UNIVERSITY OF OKLAHOMA

GRADUATE COLLEGE

# EFFECT OF OXYGEN CONTENT ON SOOT FORMATION IN A CO-FLOW DIFFUSION FLAME FUELED WITH CANOLA METHYL ESTER AND DIESEL

A THESIS

SUBMITTED TO THE GRADUATE FACULTY

in partial fulfillment of the requirements for the

Degree of

MASTER OF SCIENCE

By

STEPHANIE VIRGINIA PRADO CARBONELL

Norman, Oklahoma

2021

EFFECT OF OXYGEN CONTENT ON SOOT FORMATION IN A CO-FLOW DIFFUSION FLAME FUELED WITH CANOLA METHYL ESTER AND DIESEL

A THESIS APPROVED FOR THE

SCHOOL OF AEROSPACE AND MECHANICAL ENGINEERING

BY THE COMMITTEE CONSISTING OF

Dr. Wilson E. Merchan-Merchan, Chair

Dr. Ramkumar N. Parthasarathy

Dr. Jivtesh Garg

*This thesis and all my life are dedicated to The Sacred Heart of Jesus, Immaculate Heart of Mary, and Most Chaste Heart of St. Joseph. In these three hearts I place my trust.*

## Acknowledgements

I would first like to thank my advisor, Dr. Wilson Merchan-Merchan, for his outstanding support. The guidance and mentorship provided by Dr. Merchan-Merchan is appreciated immensely. Thank you so much Dr. Merchan-Merchan for investing in my growth as an engineer since 2016 when I began working in the Combustion Plasma and Nanoparticle Lab (CPNL) as an undergraduate. I am so thankful for the many times you stopped by the CPNL office to check-in and see how I was doing both in my personal life and research work. I appreciate the time you invested in me as your student for the past five years. I value your service as my McNair mentor, OK-LSAMP mentor, and now as my advisor. I wanted to thank you for the many meetings where we would discuss my career goals and the guidance that you provided. I really appreciate the numerous recommendation letters you wrote for me to apply to fellowship programs and graduate school. Your motivation for helping me succeed is very inspiring. I am grateful for this opportunity to work with you and for the various discussions that we had which made this thesis possible. Your insightful feedback brought my work to a higher level. Thank you Dr. Merchan-Merchan for your continuous support to help me become the engineer I am today.

I would like to acknowledge my colleagues from the CPNL. I am very grateful with Dr. Alireza Abdihamzehkolaei for his guidance and help that he provided me with the first semester I started this research. I want to thank Duncan Merchan-Breuer for his support during the development of this work. The canola methyl ester/air and diesel/air flames data provided by my colleagues is greatly appreciated.

I would also like to thank the faculty members and the staff of the University of Oklahoma for their advice and support throughout my time at OU. A special thanks for the support of my thesis committee members: Dr. Ramkumar Parthasarathy and Dr. Jivtesh Garg. Also, many thanks to Dr. Doyle Dodd for his mentorship and guiding me to pursue graduate school. Thank you, Dr. Dodd, for the many recommendation letters and the advice you provided for me to succeed in graduate school.

I gratefully acknowledge the support of the Oklahoma Louis Stokes Alliance for Minority Participation (OK-LSAMP) OU Bridge to the Doctorate Fellowship Program funded by the NSF. Thanks to their support my goal of obtaining a graduate degree became a reality. A special thanks to Dean Sherri Irvin and Dr. Rodney Bates from the OU Bridge to the Doctorate Fellowship Program for their support.

I am thankful for the OU McNair Scholars program for preparing and guiding me to pursue graduate studies. I am extremely grateful for Dr. Sophia Morren, the director of the OU McNair Scholars program for her continuous support and guiding me to pursue a graduate education.

I am grateful for the support provided by the Society of Hispanic Professional Engineers (SHPE). I am especially grateful for the community and fellowship provided by the SHPE National Graduate Committee.

I am thankful for the support and community provided by the Diversity and Inclusion Program. I would like to personally express my gratitude to Mrs. Lisa Morales, the executive director of

Diversity and Inclusion Program. Thank you, Mrs. Morales, for your continuous support ever since I became interested in pursuing an engineering degree at OU.

Finally, I am eternally grateful to God for the unconditional love and support of my family and fiancé. Thank you to my parents, Jose Gonzalo, and Monica, who have given their whole lives to support me in following my goals and dreams. Thank you 'Papi' and 'Mami' for teaching me that love, hard work, and perseverance will always help you to reach your goals. I am thankful for my brother, Jose Miguel, for always making me smile and being my motivation to set the best example as his older sister. I am grateful for my fiancé, Nathaniel Andrew, for his immense love and support. Thank you, Nathan, for always being there for me.

Thank you to Dr. Alan Nicholls from the UIC Research Resource Center. Very grateful for the assistant given in TEM studies and for helpful discussions. A special thanks to the Samuel Roberts Noble Electron Microscopy Lab at OU for help with the JEOL-2010F field emission TEM and with the JEOL2000FX (200 KeV) TEM.

The initial support of this work by the National Science Foundation (NSF) through the grant CBET-1067395 and REU CBET-1440030 is gratefully acknowledged.

The partial support for this work by the Office of the Vice President for Research at OU is gratefully acknowledged.

# Table of Contents

# List of Tables

# List of Figures

# Abstract

The release of carbon particles (or soot; nanoscale sized carbon spheres) during a combustion process is the sign of hydrocarbon fuel not burning completely. The physical property (nano scaled) and chemical compounds (depending on the fuel) are very harmful for the environment and human health causing respiratory diseases. It is important to study soot formation given the complexity of its growth mechanism. The study of soot formation is one of the most complex phenomena in combustion chemistry. The focus of this study is to enhance the understanding of soot formation in flames formed with oxygen enhanced oxidizer streams. This study is particularly unique because the fuel used is a renewable fuel (biodiesel, BD) and the oxidizer is composed of various oxygen contents. To the knowledge of the author, this is the first work that studies the soot formation of BD oxygen enhanced flames. BD is considered a renewable and clean-burning fuel, composed of vegetable oils and animal fats. Also, BD can be used in diesel engines with very little or no modifications due to its similarity to Petro fuel properties and hence has great potential to replace fossil fuels. Most soot formation studies have been performed in flames formed with gaseous fuels such as methane. In this thesis work the soot formation in vaporized coflow diffusion oxygen enriched flames of BD and No. 2 diesel is studied.

To study soot formation, we must analyze soot particles as they are forming at various flame heights. The proper method to obtain particles in this state is to study their formation in lab created flames. Previous works have studied soot particles using engines. It is very difficult to study soot formation with engines given the soot particles cannot be collected during the combustion process but only at the exhaust. Once soot reaches the end of the exhaust pipe it is different from that formed inside the piston chamber. In this study co-flow diffusion flames are used to obtain the

morphological evolution of soot and to obtain primary particle diameter ($d_p$) measurements. In this study the thermophoretic sampling technique is used to capture soot particle samples along the axial direction of the flame. That is, the thermophoretic sampler was inserted inside the flame from regions near the burner mouth to the flame tip. This sampling procedure consists of the insertion of a transmission electron microscopy (TEM) grid inside the luminous zone. Thermophoretic sampling is performed at several heights above burner (HAB) in the axial direction. Soot particles are collected at different HAB to understand the process of soot formation which consists of inception, surface growth, agglomeration, and oxidation. More specifically the BD used in the present study is canola methyl ester (CME) (Milligan Bio-TECH Inc.). The oxygen content is increased in the oxidizer stream from 21% (air), 35%, 50%, and 80%. Soot formation was studied in flames composed of CME and ultra-low sulfur diesel (ULSD) No. 2 obtained locally (Conoco gas station on 3300 W Main St, Norman, OK): CME/21% $O_2$ (air), CME/35% $O_2$, CME/50% $O_2$, CME/80% $O_2$, diesel/21% $O_2$ (air), diesel/35% $O_2$, diesel/50% $O_2$, and diesel/80% $O_2$.

TEM analysis was performed on samples of soot particles captured in the studied flames to obtain soot evolution profiles. This analysis provided low and medium resolution TEM images. To quantitively study soot formation, $d_p$ measurements were obtained at several HAB in the axial direction of the flame. To study the effect that oxygen content has on soot formation we must have a basis for comparison. In this study the CME/21% $O_2$ (air) and diesel/21% $O_2$ (air) flames were used as a basis for comparison. To study the effect BD has on soot formation under oxy/fuel conditions we use the diesel oxy/fuel flames as a basis for comparison.

The effect of oxygen content increase on soot formation in CME and No. 2 diesel lead to several observations. Overall, as the oxygen content increased in the oxidizer stream the flame height decreased and the rate of soot formation increased. Also, non-representative short aggregates were found near the burner mouth for both diesel and CME oxygen enriched air flames. Regardless of the fuel or oxygen content used, the stages of soot formation remained the same for all flames tested. The presence of soot precursors was more evident in diesel flames than in CME flames. In the CME flames, "irregular-shaped" structures or "globules" were found. The presence of "globules" decrease as the oxygen content was increased in the oxidizer stream of CME flames. Furthermore, light contrast precursor particles were found in the diesel/50% $O_2$ flame and in all the CME flames. The quantitative study of soot formation via the measurement of $d_p$, revealed that the largest $d_p$ value or peak $d_p$ values were higher for diesel flames than CME flames. Diesel/35% $O_2$ shows the highest peak $d_p$ value ~42.9 nm compared to diesel/air with ~38.5 nm, diesel/50% $O_2$ with ~36.8 nm, and diesel/80% $O_2$ with ~17.3 nm. Examining the trend in CME flames of peak $d_p$ vs. oxygen content gives interesting results. The peak $d_p$ values are as follows: CME/21% $O_2$ is ~28 nm; CME/35% $O_2$ is ~28.6 nm; and CME/50% $O_2$ is ~24 nm. Since the $d_p$ value decrease is more notable for oxygen-enhanced flames in CME we can see the oxidation process is accelerated.

# Chapter 1 – Introduction—What is Soot?

One of the main motivations for soot research is the continuous increase in energy demand which are most likely are to be derived from petrol fuels. From 2020 to 2040 there is a projected energy consumption increase of 30% [1]. One of the main sectors with high energy consumption is the transportation sector. In the transportation sector the use of diesel engines is very common, and these produce particulate matter (PM)/soot and $NO_x$ [1]. Diesel engines are internal combustion engines and of compression ignition nature. There is a tradeoff between attempting to reduce soot and $NO_x$ emissions from diesel engines. The measures in place to reduce $NO_x$ lead to restricting the soot elimination by oxidative paths. Therefore, it is crucial to eliminate soot during its early formation stages [2]. Soot is mainly carbon from the elemental perspective. However, there are some reduced amounts of species (i.e., oxygen, hydrogen, sulfur, etc.) present as well.

A solution is necessary to decrease harmful emissions from the combustion of diesel given the strict environmental regulations. PM is part of the harmful emissions which includes soot. The second largest contributor to global warming after carbon dioxide is soot [3]. Negative effects on the environment and human health are some of the drawbacks of soot emissions from industrial combustion devices [4]. Soot can easily travel through the environment causing harm given its lightweight nature [4]. A soot particle can cause more harm the smaller it is. Soot particles are miniscule carbon particles that and can easily travel into the lungs causing respiratory diseases which can lead to cancer. Some of these ultrafine particles can enter through the capillary walls into the blood stream. These particles have diameters less than a micrometer and a significant contributor to PM2.5 (PM with diameters smaller 2.5 μm) [1]. Although there can be many

important advantages with the presence of soot. High heat transfer efficiency can be obtained for combustion processes with soot present [4]. A noteworthy amount of heat by radiation can be emitted by soot given it is considered a black body. Therefore, the presence of soot is ideal for a combustion with high heat transfer efficiency in industrial processes. Additionally, the presence of soot (smoke) is an advantage for signals that there is a fire. Furthermore, there are various applications for soot (carbon black) such as tires, rubber soles, dry batteries, and inks [5]. Carbon black is a rubber-reinforcing additive for rubber products like tires and rubber soles. The conductive properties of carbon black are excellent and can be used as a component for magnetic tapes and semiconductors. Given the high coloring power of carbon black it can be used as ink for printing. Figure 1 displays images of advantages, disadvantages, and applications of soot.


***Figure 1:*** *(A) Advantages: soot signals there is a fire [6]. (B) Disadvantages: pollution in cities (environment) [7]. (C) Applications of soot [5].*

Finding solutions to PM emissions is another motivator for understanding soot formation. Biodiesel (BD) is an interesting solution to further develop efforts to reduce PM emissions and greenhouse effects. BD is derived from vegetable oils and animal fats. This environmentally friendly fuel is composed of fatty acid methyl esters (FAME) [8]. BD can be used in diesel engines without major engine modification. Although BD cannot completely replace diesel due to its high viscosity and other unstable properties, when the two are blended, the lubricity of diesel engines can be improved. It has been proven that PM emissions decrease as the BD percentage increases in the BD/diesel blends. Knothe et al. [9], observed 73-83% reductions in PM emissions when using three pure methyl esters (methyl-oleate, methyl-palmitate, and methyl-laurate) instead of conventional diesel fuel. In a study involving emission studies from heavy trucks fueled by diesel and BD blend without engine modification, Wang et al [10] shows that B35 (35% BD/65% diesel) reduces PM emissions by 25% in unaltered trucks.

Soot formation is one of the most complex phenomena in combustion, consisting of complicated interactions between combustion chemistry. Incomplete hydrocarbon reactions or combustion inefficiencies result in soot formation. Increased thermal energy could be obtained from the chemical energy present in soot particles in the form of C-H and C-C bonds if its formation could be removed, and/or, the formed soot particles could be fully oxidized at later stages [11]. To suppress and control the production of soot emissions it is critical to gain further insight into the soot formation mechanism. Although the massive amount of research, many gaps remain in understanding soot formation [1]. Even more complex is gaining an understanding of soot formation produced from BD due to the lack of investigative studies in the subject. Applications of BD in industrial combustion, where no major studies have been published considering most

research studies on the application of BD are mainly in the transportation sector with diesel engines. Unlike diesel, BDs do not contain aromatic species, therefore the soot produced is much less in comparison [12]. The need to suppress soot emission or to produce soot with BD demands a full understanding of the soot formation process. To achieve this, it is key to understand the soot formation mechanisms for BD, to study soot primary particle diameters, and the soot morphology evolution in BD.

### 1.1 Soot Formation and Evolution

Soot formation is one of the most complex phenomena that depends on various combustion parameters: fuel chemical composition, residence time, burning configuration, flame temperature and pressure [13]. Intensive research on soot formation mechanisms in the past decades indicates that in general soot formation is composed of five phases: (i) gas phase molecular species are first formed by fuel pyrolysis, which then serve as precursors; (ii) followed by the growth of polycyclic aromatic hydrocarbon (PAH) rings; (iii) particle nucleation; (iv) heterogeneous particle reaction and particle to particle interactions (coalescence and agglomeration), and (v) oxidation. Different chemical reactions are occurring in a diffusion flame. Figure 2 was adapted from the work of Shaddix and Williams and it displays the distinct regions of chemical reactions with different colors [14]. Hydrogen atoms ($H^*$) and $O_2$ are present in air and their reaction produce highly reactive chemicals. Radicals (highly reactive chemicals) such as oxygen atoms ($O^*$) and hydroxyl radicals ($OH^*$) are present to consume partially oxidized fuel fragments on the flame sheet. The outer region that surrounds the entire flame is the flame sheet. The highest temperatures are found on the flame sheet region.

In Fig. 2 the fuel pyrolysis zone (color coded blue), larger molecules are formed by a combination of fragments. The fragments come from the complex chains of hydrocarbons of the fuel which is decomposed in the fuel-pyrolysis zone where the chains are heated to high temperatures. These larger molecules are carbon-ring structures or PAHs formed by chemical reactions of acetylene ($C_2H_2$) and some radical hydrocarbon molecules ($H^*$, $CH_2^*$, $C_3H_3^*$, $C_4H_3^*$, $C_4H_5^*$). The growth of PAHs comprises a crucial phase to link formation of gaseous fuel molecules to well stablished soot structures. This has been supported by several experimental and numerical studies [15]; one of which reported that PAH molecules are highly thermodynamically stable, hence, further confirming their role on soot formation [16, 17]. The soot-inception zone (green) focuses on the transition between gas phase precursors to condensed carbon materials. In recent decades extensive research has indicated that soot nucleation is mainly driven by high molecular weight PAHs. Typical high-resolution imaging characterization suggests well defined soot structures, which are believed to be a result of PAHs stacking to create parallel layers [18]. Nonetheless, it has been reported that this phase is perhaps, the least known [15] and one that remains a topic of investigation. The soot-inception zone (green) where growth and polymerization occur to the large molecules. Gray spheres or liquid-like soot-precursors are present in this green zone. The gray spheres do not absorb or emit visible light because they do not have an internal structure.

The precursors formed in the soot-inception zone (green) enter in the soot-growth zone (yellow) and give up H2 gas and form light-absorbing particles (Fig. 2). The soot-growth zone (yellow) refers to continues growth of pre-existing soot particles through continues attachment of gaseous species, which then crystallized and favor particle size increase [19]. Despite inception being responsible for providing the nucleus for soot formation, surface growth is accountable for most

of the soot mass. For instance, numerical simulations coflow diffusion flame revealed that more than one order of magnitude soot mass comes from surface growth when compared to inception from new particles [20]. The solid particles that form in the soot-growth zone (yellow) agglomerate to form clusters of soot. Agglomeration refers to attachment of particles at a point contact while preserving the surface area. Whereas coalescence indicates the reduction of total surface area due to the elimination of the boundary between particles [21]. Despite most of the soot mass being a result of surface growth, particle to particle interactions (i.e., coalescence, agglomerations) ultimately impact the final size and morphology of the soot structures. Furthermore, at the flame tip is the soot-oxidation zone (orange) where the reactions between oxygen and hydroxyl radicals shrink the soot aggregates. The soot-oxidation zone focuses on ways to reduce/prevent soot growth and further removal. It has been recognized that the key soot oxidants are OH radicals, molecular $O_2$, and to a lesser extent $H_2O$, $CO_2$, and $NO_2$ [22]. Interestingly, at high temperatures OH radicals [23] are highly effective at oxidizing soot. Finally, the products of combustion emitted to the environment are water ($H_2O$) and carbon dioxide ($CO_2$).

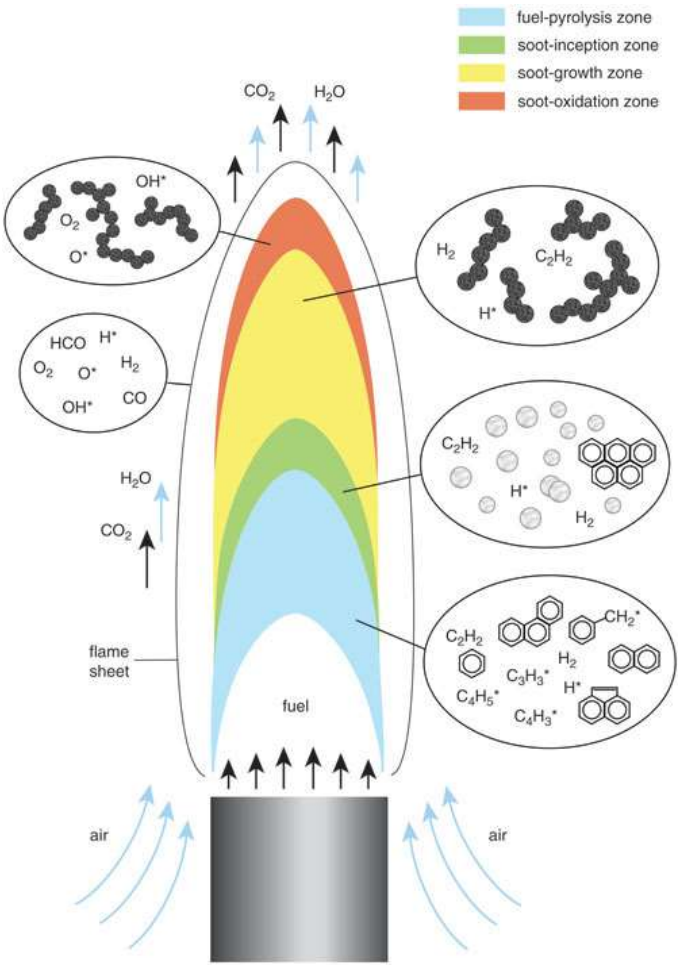


***Figure 2:*** *Soot formation chemical reactions in a coflow diffusion flame. Adapted from [14].*

### 1.2 Soot Formation in Coflow Laminar Diffusion Flames

Laboratory scale laminar flames at atmospheric or lower pressure are commonly used for soot studies. Although, real-life combustion processes are of turbulent flow and at high-pressure conditions. Consequently, due to the significant differences, multiple reactions that are dependent on turbulence-chemistry and high pressure are not considered. Nonetheless, to authorize the study soot formation in laminar/atmospheric flames there were four major components considered. First, the reliability of diagnostic techniques reduces in turbulent/high-pressure flames because of the high loads of soot [24]. Second, numerous cases have shown the instability of turbulent/high-

pressure flames is not acceptable for fundamental studies [25, 21]. Third, turbulent/high pressure flames may not have adequate spatial and temporal resolution for an acceptable assessment [21]. Fourth, it would be difficult to study soot formation in turbulent/high pressure flames; for example, using transmission electron microscopy (TEM) grids on a large turbulent flame would burn up the grid and may not be effective.

Soot formation can be difficult to study in actual processes given the many constraints and potential discrepancies in the mechanisms used to evaluate soot. That coupled with the lack of full understanding of the physico-chemical formation pathways of soot, then it is widely accepted the used of laboratory-scale devices/techniques to evaluate soot. The usage of laboratory flames removes the thermo-fluid interactions occurring inside an engine cylinder. Therefore, allowing for a better understanding of the impact of fuel chemical composition on soot properties [13]. Soot formation in turbulent or practical flames can be understood by performing fundamental investigations on laminar flames [1]. Laminar diffusion flames can aid in clarifying the sooting process in practical flames [26]. In a diffusion (non-premixed) flame the air and fuel meet and react through diffusion. For example, candles or oil lamps are diffusion flames. Soot evolution and the structure in diffusion flames, convection flow plays a critical role [21].

Soot formation evaluation has been performed extensively with the use of coflow flames [27]. Velocity, temperature, and chemicals species concentrations in a coflow has 2D (axial and radial). Coflow flames commonly are surrounded by coflowing oxidizer and the fuel injected through the burner. In coflow diffusion flames soot oxidation by oxygen hydroxyl radicals is typically obtained. Given that the flame usually covert downstream towards the high flame temperatures

where the fuel and oxidizer mix at stoichiometric levels [28]. In the fuel-rich zone bordering the fuel nozzle the polycyclic aromatic hydrocarbons (PAHs) are created. Nascent structures (i.e. inception) that form into soot particles are merely developments of PAHs components. The soot particles flow towards a higher temperature reaction area and height above burner (HAB) where soot oxidation is favored by the presence of OH radicals. Consequently, most soot particle size studies indicate that soot profiles reveal increase-and-fall behavior with increasing HAB [8, 29].

Most soot formation studies have been performed using premixed and diffusion (non-premixed) flames at normal conditions. The soot formation process of inception, surface growth, agglomeration, oxidation remains the same for either premixed or diffusion flame. Although, there are definite limitations to the overall soot formation process depending on the burner configuration used (premixed or diffusion). For example, in premixed flames the formation of precursors competes with the soot precursor's oxidation. Whereas, in diffusion flames, soot growth occurs in a very wide pyrolysis zone. There is a longer residence time in diffusion flames when comparing to premixed flames. This longer residence time is due to the very rich pyrolysis zone which allows for soot precursors to oxidize [13]. Leading to an increased surface growth and soot mass emission compared to a premixed flame [30]. The zone of particle growth is dependent on fuel chemistry and burner configuration which indicates the residence time for soot particles [13].

There is a plethora of previous works that focus on understanding the effects of BD on PM emissions of diesel engines. Cadrazco and co-workers studied the characterization of renewable diesel PM gathered from diffusion and partially premixed flame burners and from a diesel engine. The impact of fuel nature and burner type was evaluated on soot mass, primary particle diameter,

and morphology. Cadrazco et al. found that soot formed in the combustion of engines have diameters to be between those obtained in partially premixed flames and diffusion flames. This could be due to the dual nature of diesel engines. The initial combustion phase of a diesel engine is controlled by a partially premixed mixture inside the cylinder and the later phase is composed of a diffusion driven process [13]. They suggest that the costs associated with generating large quantities of fuel and the complexities of in-cylinder physical interactions and engine parameters can simply be avoided. The effect of alternative fuels on characteristics of PM can be conducted with the use of laboratory flames [13].

In this present thesis work the focus is on the understanding of the soot formation as oxygen content is increased in the oxidizer stream of flames formed with biodiesel. This is a unique area of research given that biodiesel is a new alternative fuel and liquid in nature. Most studies in the field of oxygen enhanced combustion use hydrocarbon-based fuels. Very little is known about the soot formation in biodiesel oxygen enhanced flames. Biodiesel fuels have been studied extensively in diesel engines but there is no need for them when the focus is placed on understanding soot formation due to fuel chemistry. Diesel engine studies can provide information on the structural characteristics of PM collected from the exhaust. However, the PM collected at the exhaust usually has undergone a dilution process of clean dry air. The dilution process can lead to products in the exhaust with different particle size and chemical compositions [31]. A controlled laminar flame environment eliminates physical variables that are found in diesel engines.

### 1.3 Soot Studies in Biodiesel Flames

The use of biodiesel (BD) in previous works has most commonly been in diesel engines. Although, there are several soot studies using BD as a fuel to form flames. Love et al. [32] obtained radiation, flame temperature and soot volume measurements on partially premixed flames. They used vaporized No. 2 diesel, canola methyl ester (CME), soy methyl ester (SME), and rapeseed methyl ester. Interestingly, the ignition and stabilization of the test fuel vapor flame on the burner was accomplished by using a premixed methane/air flame which was then turned off at the onset of combustion. Love and coworkers showed that soot volume fractions and flame temperatures did not significantly vary between the BDs tested. As for the comparison between BD and diesel, the peak soot volume fraction and flame temperatures were higher for BD than those of diesel. Love et al. stated that the suppressed formation of soot precursor species is due to the oxygen molecules present in BD. Also, the presence of double bonds and lower values of soot in BD flames led to increased flame temperatures when compared to diesel flames.

Soot formation in BD flames has been rigorously studied by Merchan-Merchan and coworkers. In a recent work by Merchan-Merchan et al. [33] soot evolution profiles were obtained in a coflow diffusion flame using various vaporized BDs, No.2 diesel, and blends with air as the oxidizer. BD fuels evaluated include CME, cotton methyl ester (COME), SME in their original form (denoted as B100). CME was blended with diesel to assess its effect on soot evolutions, blends evaluated were denoted as B80 (80% CME/20% No.2 diesel), B50 and B20, respectively. Results reveal that young particles (i.e., soot precursors) attained at a lower height above burner (HAB) are smaller for all BDs tested when compared to particles formed in diesel flames; similar behavior was stablished for maximum particle size regardless of HAB. For all BD flames, the formed soot

particles yielded large structures with agglomerate-like characteristics and rather irregular shapes; the irregular shape of the formed soot structures is strongly manifested at mid-flame height. Clear morphological characteristic were determined from the irregular structures: (i) presence of large eutectic components owed to the viscous liquid nature: (ii) some of the identified irregular-shaped structures presented darker areas within the structure, which are likely to resemble embedded carbonized inclusions; (iii) transmission electron microscopy (TEM) imaging suggests that the irregular-shaped structures are likely to serve as potential growth pathways to form aggregates of nearly spherical shaped at higher HAB (closer to the flame tip). These irregularly shaped structures seem to be linked to the fuel state at time of delivery for combustion processes since other works where vaporization did not take place did not presented eutectic-like components [34]. Diesel/CME blends indicated that (i) maximum particle size of the soot generated for each blend flame emulated those of the parent fuel or fuel with higher activity; (ii) increasing CME content on the mixture, resulted in the formation of a highly dense network of chain-like aggregates, whereas, pure diesel formed aggregates were of smaller size and with much reduced network; (iii) equal activity of both fuels, resulted in network of soot structure with rather difficult morphology to characterize and hence attaining a peak soot particle diameter for B50 blend was challenging.

In another related work by Merchan-Merchan et al. [8], a wick-generated laminar diffusion flame was used to study soot particles derived from CME, SME, a 50% mixture composed of SME and animal fats (AF), and diesel fuel. The technique used was also thermophoretic sampling and TEM analysis was performed to obtain soot evolutions and particle diameters. In their results it was found that carbon particulates produced from BD were remarkably smaller than those of diesel

fuel. Another interesting finding is that CME was the BD with the smallest primary particle diameter.

In other soot studies, BD surrogate has been used as fuel to form flames. Kholghy et al. [35] used a BD surrogate composed of a 50%/50% molar blend of n-decane and methyl-octanoate. They studied the effects of ester moiety on soot formation. In their work the liquid fuel was diluted with heated nitrogen and the vaporized mixture was delivered to a coflow diffusion flame configuration. Furthermore, thermophoretic sampling followed by TEM imaging to measure soot primary particle diameters along the centerline and wing of the flame. Kholghy and coworkers obtained soot morphologies along the centerline and wing for 5-decene, 1-decene, n-decane, and the BD surrogate. It was evident from their TEM images of soot particles that the presence of ester moiety seemed to delay soot formation while unsaturation significantly increased the rate of soot formation and growth. Also, the BD surrogate flame had smaller soot primary particles when compared to the n-decane flame. Another soot study that used BD surrogate in flames is Gao et al. [36]. In their work methyl decanoate was the BD surrogate used on a laminar co-flow non-premixed (diffusion) flame and partially premixed flame. They investigated the partial premixing effects on soot formation in flames by performing thermophoretic sampling. The TEM analysis along the centerline of the flame provided soot morphology information. In their results, soot evolution profiles and mean diameters of primary particles were provided. The peak mean diameter was found at mid-flame height for both diffusion and partially premixed flames. Gao and coworkers found that the size growth of primary particles and aggregates is mainly due to surface reactions such as polycyclic aromatic hydrocarbon (PAH) condensation and hydrogen abstraction-$C_2H_2$ addition mechanism and coalescence [37].

### 1.4 Oxygen Enhanced Combustion Remarks

The release of these ultra-small particles into our environment when particle oxidation is not complete can be detrimental to global warming and human health [38]. These harmful particles can be mitigated with the use of oxygen-enhanced or oxy/fuel combustion. To reduce soot emissions with the use of oxy/fuel combustion it is key to first study soot formation under oxygen enhanced conditions. There are various benefits during a combustion process when using oxygen enriched air. Flame stability increases as oxygen content increases in the oxidizer stream [34]. Higher thermal efficiency can be obtained in a combustion process formed with hydrocarbons and oxygen-enhanced air given the increase of the stoichiometric flame temperature [4, 39]. Finally, harmful emissions from incomplete combustion such as soot and NOx can be reduced in an oxy/fuel combustion [40, 41]. Higher oxygen content results in higher flame temperature which in turn increases the fuel pyrolysis and soot formation rates. Another interesting aspect of oxy/fuel combustion is that oxygen promotes and enhances soot oxidation [42]. Although, there are some drawbacks, such as the increased operational costs of using higher oxygen content than air (21% $O_2$). It can be very costly to separate oxygen from the air given the high amounts of energy required to generate high purity oxygen [43]. Also, the study of soot formation can be challenging when the flame volume is reduced to a fraction of the ~21% $O_2$ (air). Finally, the increased temperatures in oxygen enhanced combustion can lead to metallurgical problems and harm process equipment. Although, new emerging oxygen generation technologies are making the application of oxygen enhance combustion a possibility. A variety of industrial processes such as glass furnaces, boilers, and incinerators have implemented oxygen enhanced combustion [4].

*1.4.1 Soot Characterization in Oxy/Fuel Coflow Laminar Diffusion*

In the past some efforts have been undertaken to further understand the effect of oxygen content in the oxidizer stream to form the flames. Laboratory scale reactors have been used to study the effects of soot formation when the content of oxygen concentration is varied in the oxidizer stream. In the representative works that study the effect of soot formation in oxygen enhanced combustion, most have been conducted using traditional fuels and only a few works have been conducted using biodiesel. Table 1 displays a list of soot of soot studies in oxygen enhanced or oxy/fuel coflow laminar diffusion flames. The table is divided by works using traditional fuels versus BD fuel. The most common traditional fuel amongst oxy/fuel studies is methane ($CH_4$). Whereas for BD fuel, canola methyl ester, soy methyl ester, and BD surrogate were used. Most of the oxy/fuel studies enhanced the oxidizer up to 30% $O_2$. Furthermore, the most common technique used between oxygen enhanced studies is laser light extinction, most likely, given that it is a non-intrusive method. Finally, the most common objective of these studies has been to obtain soot volume fraction.

Some of the most relevant works discussed in this section are by prominent authors in the field of oxygen enhanced combustion. The study of traditionally fueled diffusion flame with oxygen enriched air can be helpful to improve actual processes and to validate soot prediction models. Henriquez and coworkers studied the effect of oxygen index (OI) on soot formation in laminar coflow propane ($C_3H_8$) diffusion flames. The OI was defined as $O_2/(O_2+N_2)$ and this represents the oxidizer levels that ranged from air (21%) to 37%. Henriquez et al. found the rates of soot growth and oxidation are enhanced as the OI increased. Given the increase in flame temperature it is expected to obtain higher rates of soot nucleation and growth [44]. A study by Kumfer et al. on

the criteria for soot inception in oxygen enhanced flames used various traditional fuels ($CH_4$, $C_2H_6$, $C_3H_8$, $C_2H_4$, $C_2H_2$). The oxygen content in the oxidizer stream was varied by the stoichiometric mixture fraction ($Z_{st}$). The experimental analysis of their work suggests that soot inception occurs when the local C/O ratio is above the critical value [45]. Soot inception limit in this work was obtained by using the soot luminosity. Another work in oxygen enhanced combustion (Lee et al.) varied the $O_2$ content from 21% (air) to 100%. The work of Lee et al. displays two main trends between oxygen content in the oxidizer stream and the flame structure. Increasing the oxygen percentage in the oxidizer stream leads to a decrease in flame height. The smaller flame sizes and low residence times leads to an overall reduction of soot content [34]. Lee et al. used a co-flow laminar diffusion flame formed with methane ($CH_4$). It was found that the increase of oxygen concentration in the oxidizer stream originally tends to promote the rate of the soot formation. However, a further increase in the oxygen content to form the co-flow flame suppressed soot formation [34]. Flame image processing has been applied on an ethylene ($C_2H_4$) coflow laminar diffusion flame and varying oxygen concentrations (21%, 30%, 40%, 50%) in the oxidizer stream to study soot volume fraction and flame temperature [46]. Yan et al. visualized the two-dimensional distributions of soot volume fraction and temperature and determined that the oxygen enriched flames had a larger soot volume fraction and higher flame temperature [46]. Finally, Zelepouga and coworkers used methane ($CH_4$) as fuel and oxygen and oxygen-enriched air for the oxidizer. Zelepouga et al. studied the effect of the addition of acetylene and polycyclic aromatic hydrocarbons (PAHs) on soot formation with non-premixed (diffusion) coflowing flames. Soot growth was found to become stronger with the enrichment of the oxidizer stream and addition of PAHs [41].

Fundamentally it is known that soot formation is highly dependent on the hydrocarbon content of the flame. Also, the ability of a flame to oxidize soot as it moves towards the tip of the flame. The following are two works that use BD as the fuel and oxygen enriched air in the oxidizer. Merchan-Merchan et al. [31] reported the effect of oxygen content in the oxidizer stream ranging from 21% to 80% in both canola methyl ester (CME) and SME flames, along with CME/No. 2 diesel blends (i.e. B20, B50, and B80). Their work focused on using laser light extinction technique to measure the soot volume fraction. The results confirmed that the oxidizers oxygen content variation has two different effects. The increase of oxygen content enhances the soot pyrolysis and thus rates of soot generation within a certain oxygen range up to threshold value (inflection point in soot kinetics. A further increase of oxygen content in the oxidizer stream above the oxygen threshold value, decreases flame height, and increases flame temperature. Therefore, favoring soot particles oxidation rates and ultimately suppressing some of the pre-synthesized soot.

In another study using BD and oxygen enhanced combustion, particles were collected thermophoretically. Lapuerta et al. [47] studied the morphology of soot agglomerates from BD surrogates in a coflow burner. The BD surrogate flame (composed of 50%/50% molar blend of n-decane and methyl octanoate). The oxidizer used was air with the addition of an extra amount of oxygen to reduce flame lift-off and improve its stability. Although, this study technically uses oxygen enhanced combustion; however, the effects of the oxygen enhancement in the oxidizer stream on soot formation was not the focus. Lapuerta's group has studied the effects of unsaturation and ester moiety in the fuel molecule on the morphology of soot particles. Their results show that the average primary particle diameter increase along the flame length until two thirds of the flame length and then decrease due to oxidation [47].

***Table 1:*** *Soot Studies in Oxy/Fuel Coflow Laminar Diffusion Flames*

| Author | Fuel | Oxidizer | Techniques | Objectives |
|---|---|---|---|---|
| ***Traditional Fuels*** | | | | |
| Henriquez et al. [44] | $C_3H_8$ | Air to 37% $O_2$ | Flame image processing, Radiant flux measurement | Soot volume fraction, Flame heights, Radiative flux |
| Kumfer et al. [45] | $CH_4$, $C_2H_6$, $C_3H_8$, $C_2H_4$, $C_2H_2$ | Air + $O_2$ | Laser induced fluorescence, Flame image processing | Flame temperature, Soot inception limit |
| Lee et al. [34] | $CH_4$ | Air, 50%, 100% $O_2$ | Thermophoretic sampling, Laser light extinction | Soot microstructure, Soot volume fraction |
| Yan et al. [46] | $C_2H_4$ | Air, 30%, 40%, 50% $O_2$ | Flame image processing | Soot volume fraction, Flame temperature |
| Zelepouga et al. [41] | $CH_4$ | Air, 35%, 50%, 100% $O_2$ | Laser light extinction | Soot fractal dimensions |
| ***Biodiesel Fuel*** | | | | |
| Merchan-Merchan et al. [31] | Canola methyl ester, Soy methyl ester | Air, 35%, 50%, 80% $O_2$ | Laser light extinction | Soot volume fraction |
| Lapuerta et al. [47] | n-Decane, 1-Decene, 5-Decene, Biodiesel Surrogate | Air + $O_2$ | Thermophoretic sampling | Average primary particle diameter |

Oxygen-enhanced combustion has been studied in terms of the soot formation process, but there are still knowledge gaps. This area of combustion research is nearly unexplored given that BD is a new alternative form of energy. BD is a renewable fuel and liquid in nature. Studying soot formation can be very complex given it requires vaporization of BD, the liquid fuel. Also, thermophoretic sampling is not widely used in oxygen enhanced studies. Most likely because thermophoretic sampling is an intrusive technique in comparison to laser light extinction. Therefore, laser light extinction is often used for oxy/fuel studies because it is a non-intrusive method. This present thesis work is unique given that not many studies use thermophoretic

sampling on oxygen enhanced BD flame to study soot formation. The study of soot morphology produced from oxygen enhanced BD flames is a nearly unexplored area of research and little is known about soot formation in these types of flames.

### 1.5 Motivation and Objectives

In the present work the effect that oxygen-enriched air has on soot formation and flame structure of a canola methyl ester (CME) co-flow flame is studied. It is crucial to understand soot formation for the emissions to be mitigated in new emerging fuels such as BD and especially the role of oxygen concentrations for soot formation. We hypothesize that size of soot diameter will vary as oxygen-enriched air is increased in the oxidizer stream to for the flame. Detailed soot evolution profiles are generated to study soot formation in high oxygen-content flames and to prove our hypothesis. Furthermore, the diesel co-flow flames are used as a basis for comparison to the BD. In the present work the effect of oxygen-enhanced combustion on soot formation is evaluated. The levels of oxygen tested in the oxidizer stream were 21% (air), 35%, 50%, and 80% $O_2$. The study is conducted using thermophoretic sampling at various heights above the burner (HAB). The analysis was performed on numerous TEM images at low and medium resolution. To summarize, the main objectives of this work are:

- To examine the effect that oxygen enhancement in the oxidizer stream has on soot formation in coflow laminar diffusion flames.
- To study the soot evolution of two types of flames (CME and No.2 diesel) are obtained and compared both as the oxygen content varied.
- To analyze the primary particle diameter ($d_p$) of oxygen-enhanced co-flow diffusion flames using CME and No. 2 diesel as the fuel.

# Chapter 2 – What is Biodiesel?

The history of biodiesel (BD) in the United States started in the 1940s when the transesterification process was used to extract glycerol during soap production [48]. The excess or residual from the transesterification process, known as glycerol, was used for wartime explosives. It was not until the 70s and 80s when the increase of oil prices occurred that extensive research began for BD processing and production [48]. BD began to be considered as a possible substitution for petro-fuel and specifically for diesel. However, as the production and consumption of BD increased several disadvantages such as fuel filter plugging, and high viscosity was encountered when using pure BD (B100) [49]. Another disadvantage of BD is the high TAN that leads to the degradation of fuel properties and hence the focus of this research study.

## 2.1 Sources of Biodiesel

Biodiesel (BD) is a renewable form of fuel created from vegetable oils and animal fats. BD is defined as a fatty acid methyl ester (FAME). Vegetable oils such as olive, cotton, canola, and corn among others are some of the primary feedstocks used to produce BD. Canadian canola is used in biofuel production around the world because it is in abundant supply. Canola is grown by 43,000 farmers who produce about 20 million tons of canola annually. In Canada, canola oil is the number one cooking oil and in the United States it is the second most popular choice [50]. BD can also be derived from animal fats such as tallow, lard, yellow grease, and poultry fat.

Given that BD is derived from food sources, there is a disagreement with the usage of food sources for fuel production. In plant origin cases like soybean oil, is mostly used for BD production that competes with the food supply chain [51]. Approximately 70-90% of the BD cost with plant origin

corresponds to raw material production [52]. The use of fertile land to produce BD rather than for a food source have created great concerns in the availability of feed [53]. Population growth does not allow for vast amounts of fertile land usage for feedstock farming of BD production. The available land is preferred for the usage of crops produced for human consumption. There is a dangerous "food versus fuel" controversy when it comes to considering sources of BD. Using feedstock for the generation of BD fuel rather than for human consumption creates adverse consequences. If feedstock for human consumption decreases the effect of supply and demand affects the availability and prices of common foods and feed.

Aquatic plants are another viable BD feedstock given the "food versus fuel" controversy. Typical aquatic plants used for the generation of BDs are shown in figure 3. This includes the cattails (top left), water lettuce (top right), water hyacinth (bottom right), and duckweeds (bottom left). Aquatic plants do not compete for the fertile land that could be used to grow feedstock for human consumption. There are approximately 107.7 million acres of wetlands in the U.S. in 2004. Another advantage of aquatic plants over fossil fuels is that they are known to recycle heat and carbon dioxide. Aquatic plants can be very beneficial as a feedstock to produce BD since it will add value to the land with a minor environmental impact [53]. The production of aquatic plants for BD production is quite unique. For instance, algae are an aquatic plant that can grow up to meters long at a fast rate and produce biomass very rapidly. Within a few hours (~6 hours) some algae species can double and many shows two doublings per day [54, 55]. Energy-rich oils can be produced by most algae groups.


***Figure 3:*** *Biodiesel feedstock from (a) aquatic plants [53].*

## 2.2 Processing and Production of Biodiesel

Biodiesel (BD) is produced through the transesterification process as shown in figure 4 below. In the transesterification process, methanol is added to a triglyceride molecule to separate the fatty acid chains that are attached to a glycerol "backbone". For every fat molecule, 3 moles of methanol are needed to separate the fatty acid chains [56]. Potassium Hydroxide or Sodium Hydroxide are typically used to act as a catalyst to speed up the reaction. In the products, 3 methyl ester chains remain as well as the glycerol "backbone" [57].

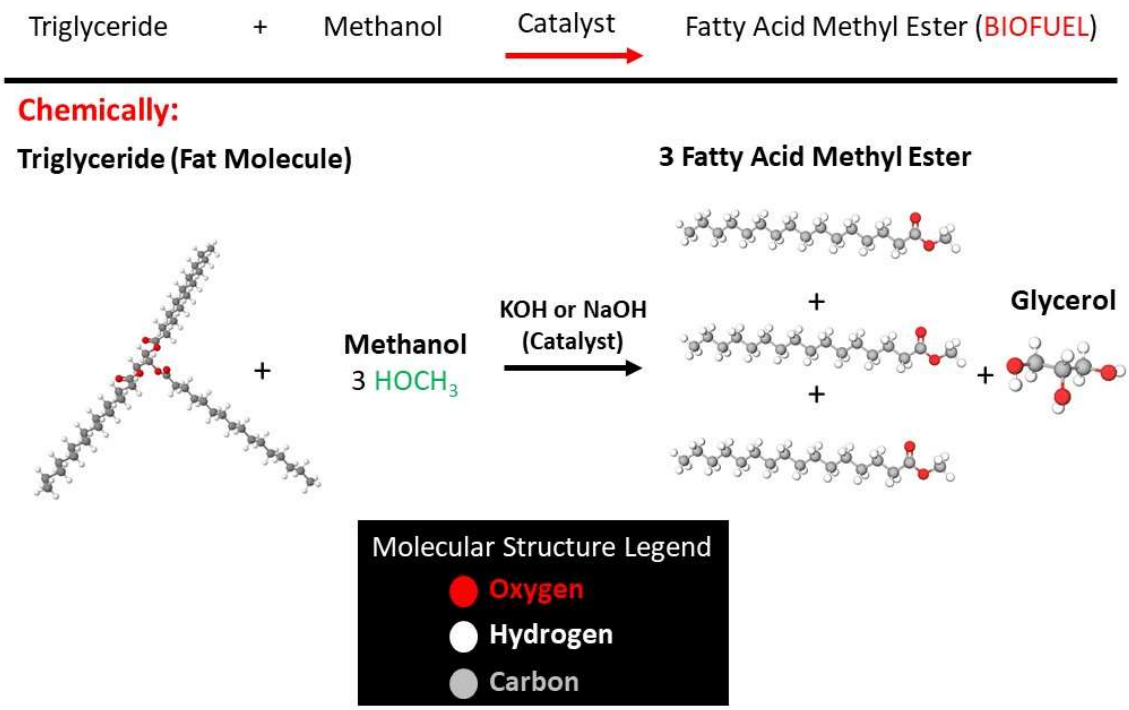


***Figure 4:*** *Transesterification Process.*

Several studies that focus on the improvement of the transesterification process, correlate instability properties with the methyl ester composition of each BD. Ramos et al. [58] aimed to study the influence of the raw material composition on BD quality, using a transesterification reaction. The work of Ramos et al. states that conversion to BD does not significantly alter fatty acid profile based on the parent lipid.

### 2.3 Biodiesel as an Alternative to Petro-fuel

Harmful emissions can be emitted when petro-fuel is used in combustion processes. Emissions of particulate matter (PM) can cause respiratory health diseases; therefore, an increased number of efforts have been placed on mitigating PM emissions. Ultra-fine particles have been estimated to result in a 1% increase in deaths for every 10 µg/m3 in PM10 (particle mass below 10 µm) [59].

Given the continuous increase of global warming and energy demand, biodiesel (BD) seems to be an alternative form of the energy solution. According to some experts, petro-fuel supplies will eventually reach its highest production level around 2050 [60]. It is critical to study alternatives to petro-fuel for global energy usage.

BD is an environmentally friendly, non-toxic, and biodegradable fuel, given that it originates from vegetable oils and animal fats. The following are the most common feedstock as sources of BD: soybean, rapeseed, sunflower, palm oil, cottonseed, and peanut [61]. BDs are defined as a fatty acid methyl ester (FAME) fuels, whose combustion tends to produce much lower carbon emissions when compared to diesel. It is well established that the burning of BD tends to produce much lower carbon emissions during a combustion process compared to diesel. The use of pure BD (B100) allows reducing the total unburned hydrocarbons (~67%), CO emissions (~48%), CO2 generation (~79%), particulate matter emissions (~47%), $SO_x$ formation (~100%), polycyclic aromatic hydrocarbons (PAHs) generation (~80%) and nitrated PAHs formation (~90%) [62, 63]. The lower emission of carbon matter resulting from the combustion of BD is considered a great advantage. Due to the oxygenated nature of the BD fuels, the grown soot particles oxidize at much rapid rate when compared to soot formed by diesel.

At this time BD cannot entirely replace diesel, yet several advantages justify its usage. One application of BD can be in diesel engines with a small decrease in performance [64]. Diesel engines operating on BD have shown a reduction in PM emissions in the exhaust gases compared with diesel fuel [65]. BD typically contains 11% oxygen by weight and lack aromatic compounds [66] which makes them suitable for soot oxidation. Diesel with poor lubricating properties can be

improved through BD and diesel blending (BD/No. 2 diesel), [**Error! Bookmark not defined.**] resulting in another advantage of BD. The cetane number (CN) property measures the combustion efficiency of a specific fuel. The CN provides an understanding of the tendency for fuel to ignite randomly [67]. It has been determined that BD can have a higher combustion efficiency and CN over that of diesel [68, 69].

However, despite the many advantages of BD over petro-fuel, recent research has shown that BD has substantial drawbacks: for instance, fuel filter plugging, and high viscosity were encountered when using pure BD (B100) [49]. High viscosity represents a BDs disadvantage and must be taken into consideration when used in combustion equipment given that the use of BD can lead to incomplete combustion [70]. Furthermore, BD has shown to possess improper cold flow properties given its high viscosity. When BD is exposed to extremely low temperatures, solid wax crystals begin to form, and this phenomenon is known as cloud point [71]. As the temperature decreases the solid crystals continuously in BD begin to enlarge and the fuel is not able to pour, this is known as pour point [72]. Canola methyl ester (CME) has a very low cloud point compared to other BD fuels, which results in a better performance [73]. Also, CME is a great lubricant in engines operating under extreme heat and steam conditions [74]. The oil generated from canola feedstocks adheres to metal surfaces better than any other oils generated from different feedstocks.

Given that the primary feedstock of BD is oils from vegetables or animal fats, a concern arises from microorganism attacks during storage or use [75]. Some of the disadvantages of BD are its corrosive properties [76]. BD is naturally corrosive given that it absorbs more water compared to diesel that tends to condense on metal surfaces and increase corrosion [75]. Given the drawbacks

encountered when using pure BD, a common solution found in recent studies is fuel blending. Which can enhance the oxidation rate of soot formed by diesel [77]. Fuel blending can take place between diesel and BD at various percentages. For example, the most common blend in peer reviewed journals is B20 which consists of 20% BD and 80% diesel. Overall, BD may lead to higher efficiencies and lower pollutant emissions than petroleum diesel [78].

### *2.3.1 Effects of Oxygenated Fuel on Soot Formation*

Biodiesel (BD) naturally has oxygen content linked to the hydrocarbon compound and is known as an oxygenated fuel. Fuel molecules play a critical role in assessing the tendency to form soot in any combustion system [79]. Verma and coworkers [80] evaluated the influence of the fuel oxygen content on morphology characteristics of soot particles by employing diesel, coconut BD, triacetin and blends thereof in 6-cylidner diesel engine. Fuel mixtures were performed in such way that the overall fuel oxygen content varied from 0% to 14%wt. The primary particle diameter was a characteristic feature evaluated. Based on results, the authors expressed: (1) the presence of oxygen on B100 and blended fuels favors the oxidation process, hence, diminishing the surface growth of soot particles and as a result smaller particle sizes were attained. Varying the engine speed also affects the soot morphology evolution resulting in increased particle size with reduction in engine speed presumably due to the longer residence times and ability of the particle to growth to coalescence or aggregation mechanisms. (2) The number of particles showed no major variation with changes in fuel oxygen content, rather the particulate mass was reduced, which indicates that the mass reduction is a result of the lower particle diameters instead of a reduction in the number of particles. Hence, suggesting that the oxygen atoms bonded to the fuel plays a critical role in soot morphological evolution. Though, discrepancies in the trends observed when analyzing

triacetin based fuel blends indicate that the soot morphological evolution can also depend in other factors.

Savic et al. [81] investigated the morphology, microstructure, and surface composition of diesel engine exhaust particles from petroleum diesel and BD blends from microalgae, cotton seed oil (CSO), and waste cooking oil (WCO). The content of BD in the diesel/BD blends allows for increasing the content of oxygen in the resulting fuel blends. Results indicated that BDs and their addition to diesel fuels yields smaller primary particle sizes, which is alignment with other studies [82, 83]. A correlation was found between primary particle diameter and fuel's oxygen content along with their respective fuel particle size distributions. It is evident from their results that soot particle size decreases with increasing BD and hence oxygen content in the fuel blends [81] at 50% engine load.

### 2.4 Biodiesel in Industrial Combustion

Biodiesel (BD) used in industrial combustion can address the growing concern of taking care of the environment. This new and emerging fuel is considered a prospective fuel in the field of the gas turbine, given that meeting emission objectives and reducing operating cost are required characteristics [84]. Habib et al. studied the emission characteristics of BD in a small-scale gas turbine. They used the following BD: soy methyl ester, canola methyl ester, recycled rapeseed methyl ester, and hog-fat biofuel. The mentioned BD were blended 50% by volume with Jet A (B50) or tested pure (B100) and used Jet A as basis for comparison. Habib and coworkers found the pure BD resulted in strikingly higher thermal efficiencies than Jet A and the blends [85].

Kurji et al [84] used a 20-kW swirl burner to analyze gas turbine combustion features while comparing the combustion of $CO_2$/$CH_4$/Diesel vs $CO_2$/$CH_4$/BD blends at atmospheric conditions. The BD used was derived from cooking oil. $CO_2$ is introduced into the BD mixture to help reduce the flame temperature, along with NOx emissions. The results showed that the chemiluminescence intensity peaks are much higher for diesel flames compared to BD, which indicates that BD has a lower sooting tendency than that of diesel. Overall, $CO_2$/$CH_4$/BD mixtures produced the cleanest profiles with the best flame stability. Furthermore, a combustion process run with BDs can significantly reduce the amount of soot formed. It is imperative to study and understand the soot particle formation when BD is used in combustion processes.

### *2.4.1 Reduction of Particulate Matter Emissions with Biodiesel*

Currently, it is difficult to find research work on biodiesel (BD) soot formation in burners, boilers, gas turbines, and other industrial combustion equiptment. Whithin this section several studies are discussed that evaluate the soot formation in relation to industrial combustion. There are a few studies that analyze the PM emissions from BDs on combustion equipment including a laboratory combustion chamber, large-scale laboratory furnace, and a low NOx combustor. Another interesting aspect of PM emissions is the effect of fuel blending on soot formation. Considering the nature of BD being an oxygenated fuel, the soot particles that are formed oxidize much faster compared to soot formed by diesel. Fuel blending can enhance the oxidation rate of soot formed by diesel. Omidvarborna et al. [86] studied soot characteristics of B20, B50 and ultra-low sulfur diesel (ULSD) through transmission electron microscopy (TEM) images. The BD used for the

blends came from three different sources, soybean methyl ester (SME), tallow oil (TO), and waste cooking oil (WCO). The combustion tests were performed in a 300 mL chamber and the device included a stainless steel reactor that was placed in an electrically heated chamber. Their work determined that the blending of BD and diesel reduces the soot particles size. BD fuels contained oxygen bonds and an unsaturated nature, both which, allow for a decrease in soot particle formation. The enhanced oxidation nature of BD tends to make the size distribution of soot particles narrower compared to diesel.

Pereira et al. [78] analyzed the PM emissions by taking scanning electron microscopy (SEM) images of BD and diesel soot formed at three different furnace operating conditions. In this study the Instituto Superior Tecnico's large-scale laboratory furnace and its auxiliary equipment were used. The BD used was composed of eleven different fatty acids. Their results show that the atomizing air/fuel ratio (AFR) directly affects the PM emissions. As the AFR increases the PM emissions of BD decrease significantly. The PM emission of diesel when AFR = 2, was significantly higher than that of BD. The main takeaway from the work of Pereira and coworkers is that the quality of atomization of BD or diesel directly affects the PM emissions.

Differing slightly from the previously mentioned studies, Altaher et al [59] analyzed PM emissions in a well-mixed lean low NOx combustion. The combustion test facility consisted of an air supply fan, venturi flow metering, electrical preheaters, air plenum chamber, double passage radial swirler, long wall fuel injector, and uncooled combustor. Natural gas combustion was compared with pure kerosene and blends of B20, B50, and B100. The type of BD used was waste rapeseed

cooking oil methyl ester (WME). The PM emissions were compared as a function of the lean well mixed primary zone equivalence ratio. Their results showed that natural gas had the highest PM emissions compared to BD and its blends. Altaher et al. [59] suggested that the lower turbulent mixing at lower Mach numbers may have contributed to a higher number and larger size of the particulates. Finally, their results showed that B100 had the smallest and lowest number of soot particles compared to B20. Again, due to the nature of BD being an oxygenated fuel these results are expected.

### *2.4.2 Biodiesel Soot Studies in Diesel Engines*

The use of biodiesel (BD) on diesel engines has interesting effects on PM emissions. Various aspects of BD are superior to those of diesel given it can reduce PM emissions due its low sufur content and oxygenated fuel nature. The following studies discuss how BD reduces PM emissions, as well as soot size and formation. Soot formations of BD have been studied in diesel engines emissions extensively. Lapuerta et al [87] conducted an analysis of work written in scientific journals about diesel engine emissions when using BD as opposed to diesel. Given the oxygenated fuel nature of BD, it is able to further reduce PM emissions during high load operation of diesel engines [88]. Furthermore, they provide a section discussing the effect of BD on particle size distributions. Results in previous works explain that BD can reduce the soot formation given its low sulfur content. Note that sulfur content has been known to be the root of nucleation and soot formation [89]. Also, they discuss that BD produces a higher number of small soot particles and reduces the number of large soot particles [90]. Finally, the acutal structure of the soot formation in BD is less structured than that of diesel which can enhance the oxidation of BD and contribute

to the reduction of PM emissions. The internal structure of BD primary particles have hollow cavities which can enhance the oxidation of soot [91]. Another research group, Boehman et al [77] studied soot aggregagets emitted at the exhaust of a diesel engine using four different fuels. The fuels tested consisted of low sulfur diesel (LSD), ultralow sulfur diesel (ULSD), LSD/B20, and ULSD/B20. The addition of BD condensates the hydrocarbons that surrounds the aggregates. Futhermore, the B20 soot formations are much more amorphous than diesel which allows for $O_2$ chemisorption and increases oxidative reactivity [92]. The increase of oxidative activity reduces PM emissions. Also, given that there is no sufficient polycyclic aromatic hydrocarbons (PAHs) in B20, this leads to the soot inception to be amorphous. Since PAHs are the reason diesel soot particles form in an orderly fashion.

Further examination was performed by a different research group, on the effect BD from five different sources used in a diesel engine. Wu et al [93] compared the PM and dry soot (DS) emitted from cottonseed methyl ester (COME), soybean methyl ester (SME), rapeseed methyl ester (RME), palm oil methyl ester (PME), and waste cooking oil methyl ester (WME) which were compared to diesel emissions. The type of BD or feedstock origin can affect PM emissions. It was found that different types of BD can reduce PM emission by 53-69% on average. Also, the higher viscosity of BD worsens atomization of fuel and increases PM emission but at high load the oxygenated fuel is able to decrease PM emissions and not focus on its poor viscous properties. Finally, higher engine speeds can enhance combustion.

Another research group obtained similar results as the previously mentioned authors when using BD in diesel engines. Xue et al [63] performed a review on the effect of BD on engine performances and emissions. This group found that the usage of BD instead of diesel reduces PM emissions from diesel engines. There are various studies that tested several BD/diesel blends which showed PM reduction as BD increases in the blend. One of the major reasons for PM reductions when using BD is its composition which is high oxygen content that allows for complete combustion and the lack of aromatic compounds and sulphur. Overall these are some main aspects of BD that must be understood to for future applications in combustion equiptment.

**2.5 Diesel vs. Biodiesel**

Aromatic-fueled combustion processes favor molecular growth outside the first aromatic ring turns out to be key for rate control towards soot formation. This results in the formation of larger polycyclic aromatic hydrocarbons (PAH) which, in turn, are more likely to form soot. Contrary to conventional diesel which is made from aliphatic/aromatic-based hydrocarbons, biodiesel (BD) is an oxygenated fuel created by the transesterification of oils which lack the presence of aromatics, nor sulfur, and rather containing long-chain alkyl esters [94]. This results in many advantages including the reduction of PAHs [95] and elemental carbon [96]. No. 2 diesel and BD used in this present work are made up of various constituents. No. 2 diesel is an ultra-low sulfur diesel (ULSD) composed of saturated hydrocarbons (paraffins, monocycloparaffins, bicycloparaffins, and tricycloparaffins) and aromatic hydrocarbons (alkylbenzenes, teralins, dinaphthenobenzenes, naphthalenes, acenaphthenes, acenaphthylenes, and phenanthrenes). Fatty acid methyl esters make up BD fuel whereas, diesel is made up of saturated hydrocarbons (75.3%) and aromatic compounds (24.7%) by volume. The BD used in this study is canola methyl ester (CME) which is composed

of methyl palmitate (5%), methyl stearate (3%), methyl oleate (62%), methyl linoleate (20%) and methyl linolenate (10%) by weight. In a work by Love et al. [32] diesel and BDs were used to study soot formation. In their work, the average representative composition of the No. 2 diesel fuel was assumed to be hexadecane $C_{16}H_{34}$; while the molecular formulas for canola, rapeseed, and soy methyl ester BDs were $C_{19}H_{36}O_2$, $C_{19}H_{35}O_2$, and $C_{21}H_{28}O_2$, respectively. The presence of oxygen is the main difference in the molecular structure of BDs when compared to diesel. Soot particles formed by oxygenated fuels like BD favor rapid oxidation reactions when compared to diesel soot, mainly due to the increase of oxidized surfaces during the growth process [94].

## 2.6 Chapter Summary

This chapter provided an overview of biodiesel (BD), a renewable and environmentally friendly fuel. The sources of BD are mainly vegetable oils and animal fats. BD is defined as a fatty acid methyl ester and produced by the transesterification process. Currently, BD is seen as an alternative to petroleum-based fuel (diesel). Although, BD cannot entirely replace diesel there are various advantages to BD that justify its usage. The use of pure BD allows for the reduction of particulate matter (PM) emissions. Also, because BD is an oxygenated fuel the oxidation of soot particles formed in BD flames oxidate at a much faster rate than diesel soot. Finally, an intensive review of previous works in the following areas are provided: (i) effects of oxygenated fuel on soot formation, (ii) BD in industrial combustion, (iii) reduction of PM emissions with BD, and (iv) BD soot studies in diesel engines.

# Chapter 3 – Experimental Approach

In the present work the main components of the experimental set-up include a thermophoretic sampler device, a coflow burner, mixing chamber, pre-vaporizer, and a fuel micropump. Soot evolution and morphology studies are conducted in the generated laminar co-flow diffusion flame. Vaporized canola methyl ester (CME) and vaporized ultra-low sulfur (ULSD) diesel No. 2 are used as fuel. The oxidizer is made up of oxygen enriched air. Descriptions and procedures of the experimental approach are discussed in this chapter.

## 3.1 Experimental Set-Up

The experimental set-up consists of a thermophoretic sampler device, coflow burner, mixing chamber, pre-vaporizer, and a fuel micropump (Figure 5). The thermophoretic sampler device is mounted on a horizontal platform and sits stationary on an optical table within experimental set-up. The sampler consists of a transmission electron microscopy (TEM) grid attached to the tip of the shaft of the 50 mm stroke compressed-air piston controlled by a pneumatic valve (Model SY5140, SMC Corp. of America). The center of the sampler was aligned with the edge of the fuel nozzle without the presence of a flame prior to sampling. The electronic control box set the residence time of the grid inside the flame. While the air solenoid valve regulated the travel time. The sampler shoots into the flame to capture soot particles with a special TEM grid (SPI, Inc.). The concept behind thermophoretic sampling is that soot particles attach onto the TEM grid by the temperature gradient between flame and the surface of the cold grid (room temperature). The thermophoretic sampling technique used is based on the one developed by Megaridis and Dobbins [97, 98] and used by others [99, 100, 101].

The sampler is mounted on an optical table and sits stationary on a stable system, therefore the coflow burner is placed on a two-dimensional step motor driven positioner. In this experimental set-up we move the burner to the desired height for the sampler to shoot inside the flame and gather soot particles. This way by moving the burner we can insert the TEM grid mounted on sampler at different heights within the flame volume. Therefore, the burner is mounted on 2-D UniSlide assemblies (MA 6000, Velmex Inc.), driven by an 8300 series stepping motor controller. The 2-D positioner allows the burner to move freely about the X and Y axis. A laptop computer was used to control the operations of the motion system with the Computer Optimized Stepper Motor Operating System (COSMOS V3.1.4) software. The 2-D positioner can move the burner with high precision (0.0000625 inches). A coflow burner was used to produce a laminar diffusion flame with biodiesel (BD) and diesel fuel. The burner used in this study is a slightly modified version of the coflow burner developed for studying methane/ethane flames by Santoro et al. [102]. A mixing chamber is used to mix laboratory dry air and industrial bottled oxygen (98% Airgas). The mixing chamber has ceramic beads inside to mix the oxidizer. Further details of the burner configuration and the mixing chamber are discussed in the next section (3.2 Burner Configuration).

In this study two liquid fuels are used: canola methyl ester (CME) (Milligan Bio-TECH Inc.) and ultra-low sulfur diesel (ULSD) No. 2 obtained locally (Conoco gas station on 3300 W Main St, Norman, OK). The BD chosen for this study CME mainly due to their large availability and benefits over petro-fuel. The liquid fuels (CME and No. 2 diesel) were pumped at a constant rate of 6 ml/h by a syringe pump (Model EW-74900-00 1-Channel from Cole-Parmer, Inc.) into a pre-vaporizer. The pre-vaporizer pipe has a total length of 65 inches and an inner diameter of 1 inch

as shown in the pre-vaporizer dimensions within figure 5. The pre-vaporizer was fully insulated and externally heated. The wall of the pre-vaporizer assembly and fuel line were heated by an array of three heating tapes. Temperature controllers were used to set the temperatures of the heating tapes. The inner temperatures of the pre-vaporizer were monitored by thermocouples and the desired temperatures to evaporate the liquid fuel were maintained. The first heating tape is set to 350 $^{o}$C to introduce the liquid BD to the pre-vaporizer. Furthermore, to prevent condensation of the vaporized fuel, there were other two heating tapes set at higher temperatures (475 and 500 $^{o}$C) and place downstream in the fuel line connecting the outlet of the pre-vaporizer with the burner. A small (~0.1 lpm) nitrogen ($N_2$) flow was introduced to the fuel line as a carrier gas. The small nitrogen flow ensured flame ignition, sustainability, and stability for the difficulties caused by the evaporation process of BD. The wall of the pipe carrying the flow nitrogen was heated by tape wrapping at 400 $^{o}$C. Also, the oxidizer line was preheated to 200 $^{o}$C [33].

As stated in the literature, the soot propensity of the fuel can significantly change if there are changes to the chemical composition of the BD. Therefore, monitoring of the vaporized fuel temperatures is critical to prevent fuel cracking and ensure the thermal stability of BD. As advised by Lin et al. [103, 104] the vaporized (BD and No. 2 diesel) fuel temperature was maintained lower than 275 $^{o}$C. Thermal decomposition of liquid hydrocarbon fuels (diesel) begins with the thermal oxidation reaction regime (<300 $^{o}$C) [104], hence the vaporized fuel temperature was maintained lower than 275 $^{o}$C for both BD and No. 2 diesel. Temperature measurements of the gas flow at the fuel nozzle in the burner verified this effect in our experiments. Also, the unburned fuel extracted from the fuel line was visually inspected. There was no visual indication of severe fuel cracking or carbonization during the vaporization process [31].

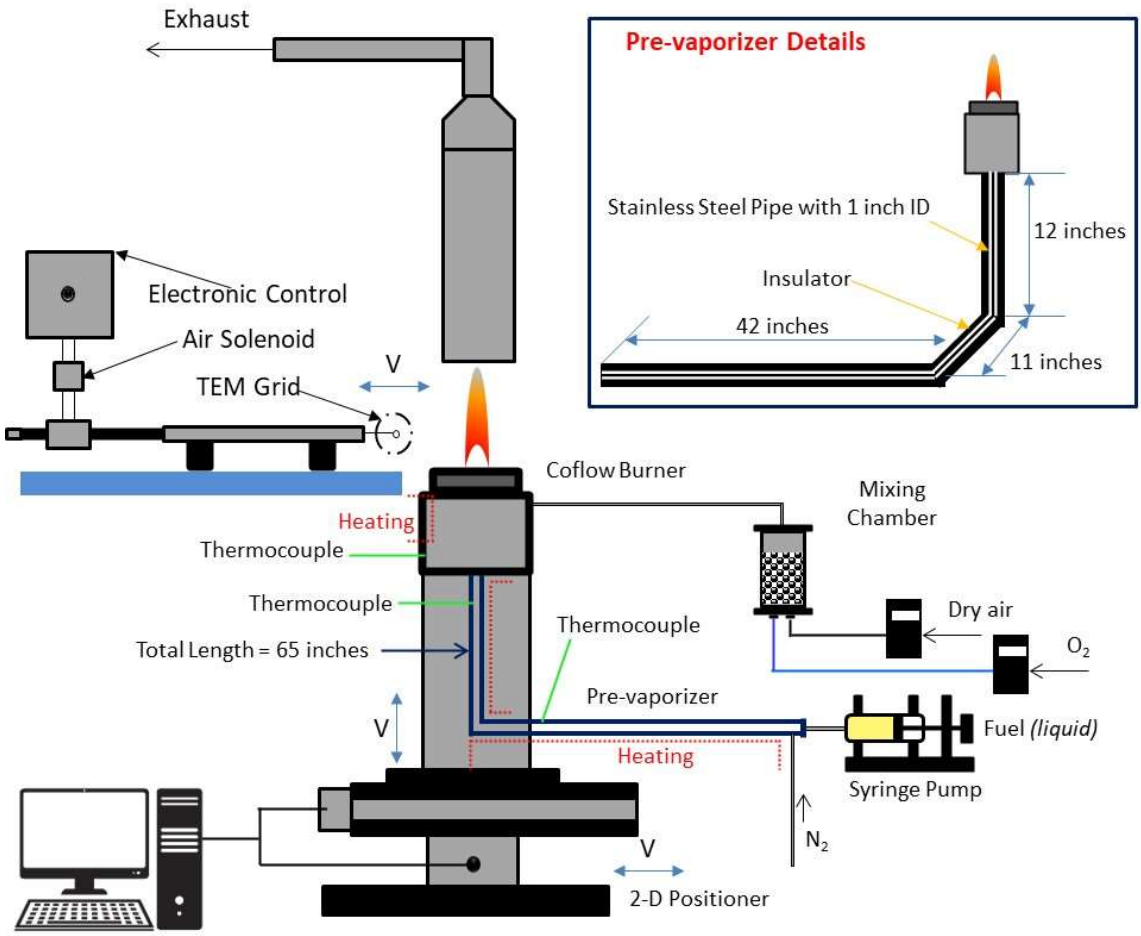


***Figure 5:*** *Schematic of the experimental setup to study soot formation and evolution in oxygen-enhanced co-flow diffusion flames formed using BD and diesel. The rigth upper corner insert provides details of the pre-vaporizer.*

### 3.2 Burner Configuration

A detailed view of the coflow diffusion burner is provided in Figure 6A. The stainless-steel burner is 178 mm tall, and the thickness of the burner walls is ~3 mm. The burner is comprised of two concentric tubes of 11 mm and 82 mm in diameter. The inner pipe is designed for supplying the vaporized fuel and the outer pipe supplies the oxidizer. After the set-up has been pre-heated, then

the liquid fuel is introduced into the pre-vaporizer by the syringe pump operating at a rate of 6 ml/h. Once the fuel vapor has been carried to the burner mouth by small amount nitrogen ($N_2$) flow, then the oxidizer is introduced. The oxygen content in the oxidizer stream was set to different percentages: 21% (air), 35%, 50%, and 80% $O_2$. The oxidizer was prepared in the mixing chamber (Fig. 5) by mixing flows of industrial bottled oxygen (98% Airgas) and laboratory dry air. The oxidizer flow rate of 38.10 lpm was kept constant and measured with the gas at ambient conditions. Oxygen and air enter the vacant chamber and then pass through a section containing glass spheres of 3 mm in diameter. The glass spheres present in Fig. 6 stabilize the flows of air and oxygen by making the flow uniform. Then the flows (air/$O_2$) pass through a ceramic honeycomb section to evenly distribute the oxidizer flows inside the burner. The honeycomb is 51 mm thick and has cells of 1.5 mm in size. Furthermore, the coflow diffusion burner configuration can form laminar and turbulent flames. In this study of soot particle morphology, the flame formed was always laminar (Fig. 6B). The studied flames where perfectly symmetrical along the axis of the flame and lacked the presence of vortices and eddies. None of the conditions used for this study resulted in turbulent flames. This is supported by the series of photographs collected from formed flames under the tested conditions (Fig. 7). Turbulent flames contain the presence of vortices or eddies as shown in the schematic of figure 6C.

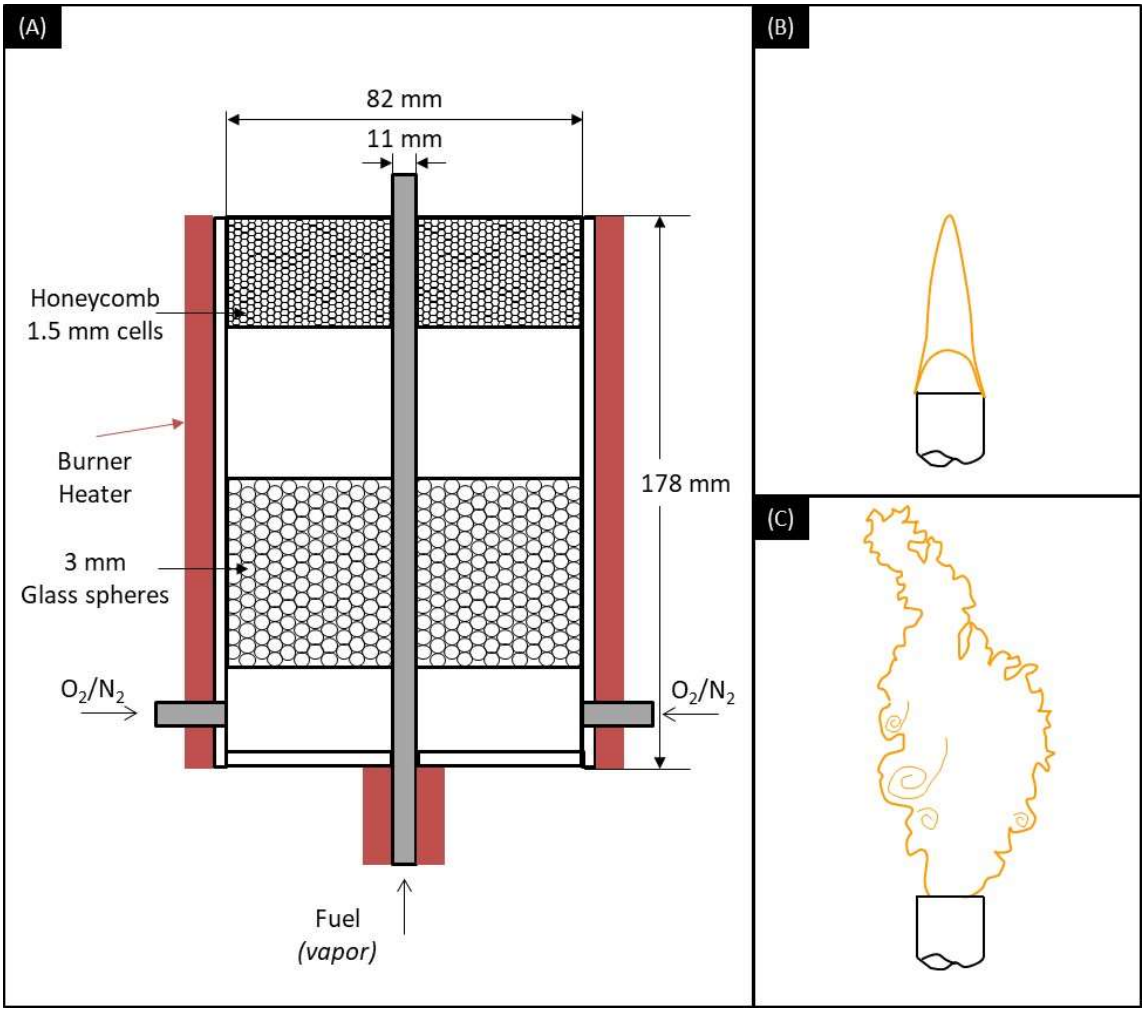


***Figure 6:*** *(A) Detailed view of the coflow burner. Schematics of typcial characteristics in (B) laminar and (C) turbulent flames.*

*3.2.1 Overview of the Studied Flames*

As the oxygen concentration increased in the oxidizer stream to form the flames their length became shorter. Regardless of fuel type or burner configuration (e.g., light vs heavy hydrocarbons or coflow vs counter flow) the flame physical structure and appearance is altered by the change of oxygen content in the oxidizer stream [40]. The increased oxygen content in the oxidizer stream

allows for a more complete combustion reaction and hence less black body radiating soot. Figure 7 contains photographs of the B100 CME and diesel flames as the oxygen concentration is varied in the oxidizer stream. The outer diameter of the inner tube is 12.7 mm. For instance, for a CME/21% $O_2$ the flame length is ~ 27 mm, CME/35% $O_2$ the flame length is ~22 mm, CME/50% $O_2$ the flame length is 14 mm, and for the CME/80% $O_2$ the flame length is 9 mm (Fig. 7(A)). The diesel flames had the following heights: diesel/21% $O_2$ the flame length is ~ 34 mm, diesel/35% $O_2$ the flame length is ~25 mm, diesel/50% $O_2$ the flame length is 13 mm, and for the diesel/80% $O_2$ the flame length is 8 mm (Fig. 7(B)). Finally, the testing conditions to create the studied flames are listed below in Table 2.

***Table 2:*** *Testing Conditions*

| **Studied Flames** | **Oxidizer Flow Rate (lpm)** | **Air Flow Rate (lpm)** | **$O_2$ Flow Rate (lpm)** | **Carrier Gas Flow Rate (lpm)** | **Pumping of Fuel (ml/h)** |
|---|---|---|---|---|---|
| Diesel/21% $O_2$ (air) | 38.10 | 38.10 | 0 | ~0.1 | 6.0 |
| Diesel/35% $O_2$ | 38.10 | 31.35 | 6.75 | ~0.1 | 6.0 |
| Diesel/50% $O_2$ | 38.10 | 24.11 | 13.99 | ~0.1 | 6.0 |
| Diesel/80% $O_2$ | 38.10 | 9.65 | 28.45 | ~0.1 | 6.0 |
| CME/21% $O_2$ (air) | 38.10 | 38.10 | 0 | ~0.1 | 6.0 |
| CME/35% $O_2$ | 38.10 | 31.35 | 6.75 | ~0.1 | 6.0 |
| CME/50% $O_2$ | 38.10 | 24.11 | 13.99 | ~0.1 | 6.0 |
| CME/80% $O_2$ | 38.10 | 9.65 | 28.45 | ~0.1 | 6.0 |

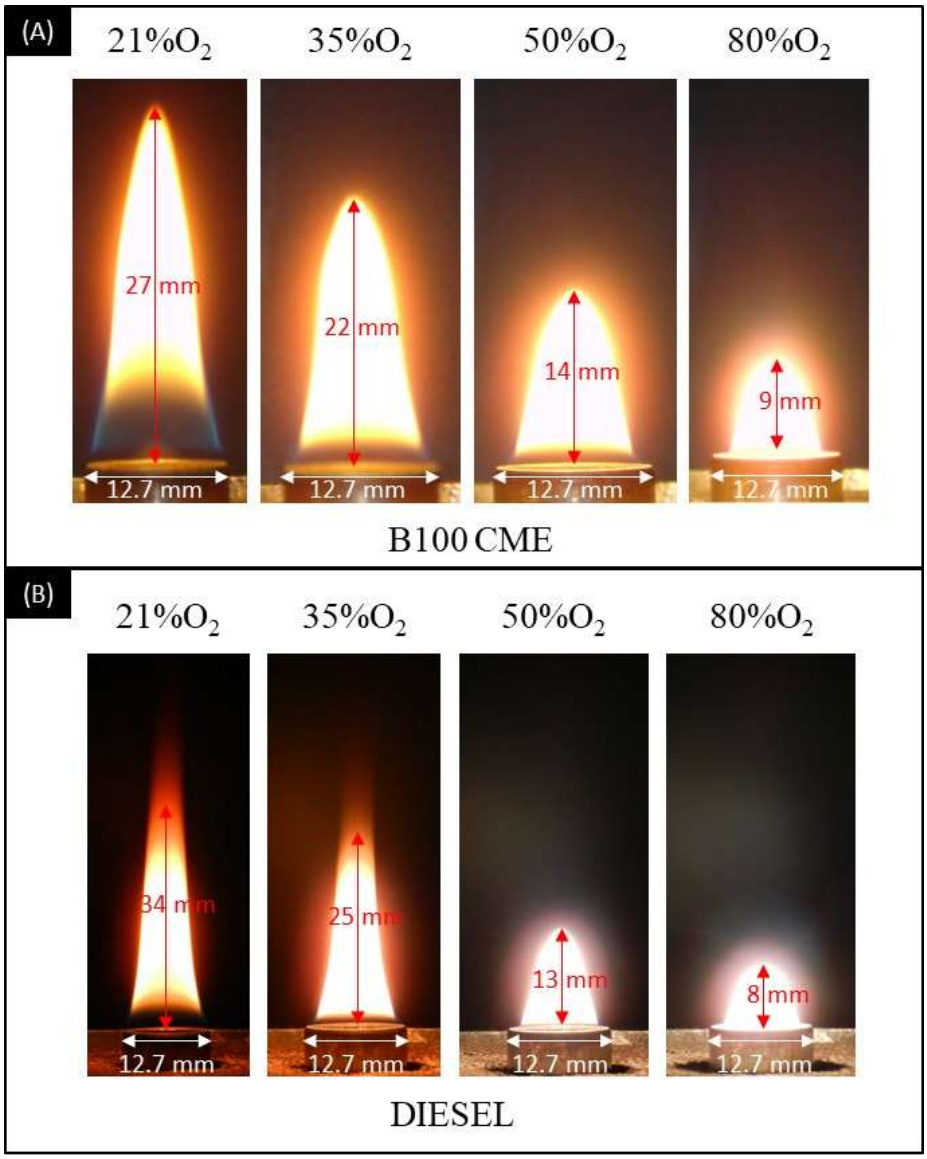


***Figure 7:*** *(A) CME and (B) diesel coflow flames with the oxygen content in the oxidizer stream ranged from 21% (air) to 80%. Each flame has their respective flame height (H) dimension and the nozzle outer diameter.*

### 3.3 Thermophoretic Sampling

Further insight into soot morphology and primary particle diameter, among other factors can be determined using thermophoretic sampling. This technique relies on drifting hot soot particles toward the cold surface of the transition electron microscopy (TEM) grid introduced into the hot flame environment. Thermophoretic deposition occurs as the TEM grid at room temperature is inserted inside the high temperature medium of the flame, particles tend to freeze on the carbon film. The grids are made of copper with a film of carbon on their surface (EMS, Inc.). A detailed view of inserting the TEM grid into the flame is available in Figure 8. Using the thermophoretic sampling technique, the TEM grid is inserted inside the flame volume along the axial direction at various heights above burner (HAB). The gathered soot particles from inside the flame's yellow luminous zone can then be used for further TEM analysis to obtain images.

An important consideration when performing thermophoretic sampling is the residence time of the sampler inside the flame. If residence time is rather short, not sufficient particles are to be collected; conversely, if the residence time is too long the TEM grid could be damaged (i.e. burned), or the particle's properties could vary due to thermal annealing. Typically, the residence time ranges in the order of milliseconds [105] and pneumatic systems are commonly used to allow for controlling the residence time, depth of collection, and allow for multiple introductions in the flame. In our study the residence time of the TEM grid inside the flame is 38 ms and approximately 10 ms for the grid's travel time.

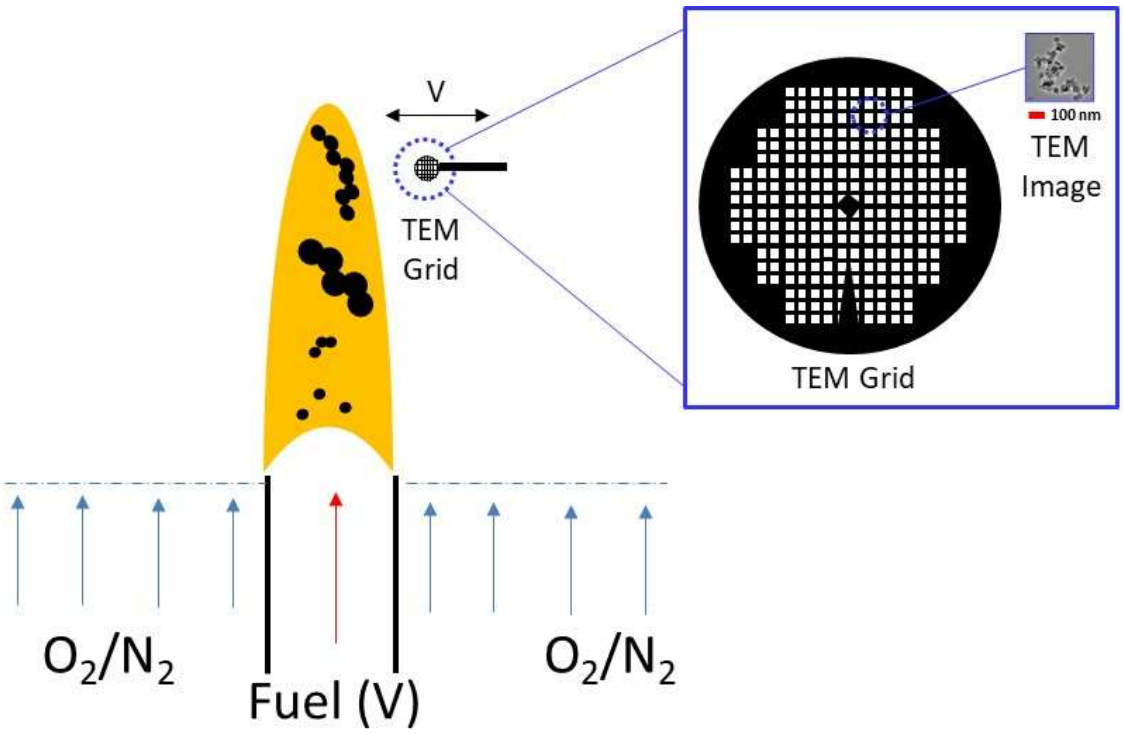


***Figure 8:*** *Detailed view of thermophoretic sampling using the TEM grid to gather soot particles in a coflow laminar diffusion flame.*

*3.3.1 Transmission Electron Microscopy Grid*

The special TEM grid used in this study is the H2 Finder Index (SPI Supplies), Figure 9. This grid is a 200-mesh copper with a 3 mm diameter and various reference patterns to enable a particular grid area under the microscope. The support grid is fabricated of copper and coated with a thin film (~20 nm) of amorphous carbon on one side of the grid. The grid has an inverted "V" shape at its bottom which provides the orientation of the grid when introducing into the flame (Fig. 9). That is, it was made sure that the inverted "V" shape is parallel to the flame axis. The grid is composed of nine main columns and six rows: each section measures 381µm and each subsection 127µm. Each section has a micron size letter or number for reference at the center and six subsections. The

letters range from A – Z, 1 – 10, and symbols are on the outer columns as displayed in Fig. 9. The letters/numbers/symbols allowed us to follow a column of the grid to provide precise soot evolution. A column of the grid can also be known as the TEM path of analysis as labeled in green (Fig. 9). As pointed out by the TEM analysis path in Figure 9, TEM images were collected following a column (i.e., D, J, Q, X, 4, 9). TEM images were collected at the center of the section that was analyzed, for instance, the TEM shown was gathered from the center of the "X" section (Fig. 9). Having the letters in each section of the TEM grid allowed us to keep track of the exact sampled height above burner (HAB). Given that oxygen enhanced flames are short this unique type of TEM grid allowed us to obtain soot samples at various heights very accurately. To obtain the evolution and morphology of soot particles forming inside oxygen enhanced flames we must capture them directly inside the flame. The soot particles are forming in short flames; therefore, this highly accurate method was developed and implemented in the study.

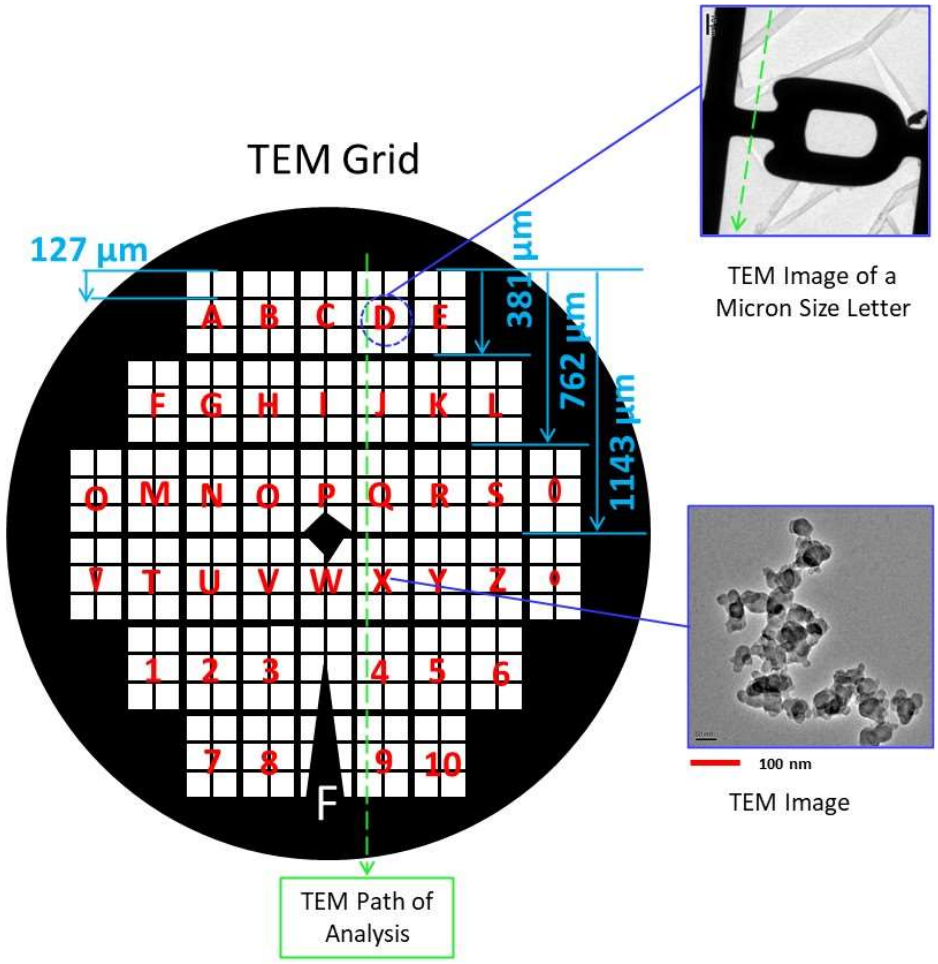


***Figure 9:*** *Top view of a H2 Finder (index) grid with dimensions. Close up view of letter D within the H2 Finder Index grid. Letters in the TEM grid allow tracking the precise position of the soot particles inside the flame volume.*

### 3.4 Transmission Electron Microscopy

The soot samples gathered by the transmission electron microscopy (TEM) grid are prepared by being stored in a desiccator for a few days prior to the TEM analysis. Not much sample preparation is necessary because the soot particles are carbon black and conductive. The electron beam from the TEM scope will be able to analyze the soot particles without any further sample preparation. Also, the TEM grid is specially made for TEM analysis with the carbon coating. Imaging of

samples collected from inside the flame was conducted using a high resolution JEOL TEM-3010 electron microscope. The microscope was operated at 200 KeV with a LaB6 filament. The TEM micrographs were collected on a Gatan digital imaging system and processed by digital micrograph software. A series of images were collected with low and medium resolution. The particle diameter profiles were obtained by measuring representative particles in the TEM images collected at medium resolution. The primary particle diameter ($d_p$) was measured using Adobe Photoshop to measure the diameter of the representative particles in pixels. The pixel values were converted to nanometers (nm) which is the unit of measurement used for $d_p$.

TEM analysis of these particles can provide detailed information on the morphology and size of the soot aggregates along with their internal structure. However, it has been reported that nascent structures are rather transparent to the TEM electron beam since they tend to be liquid-like structures, thereby, challenging the ability of TEM to characterize particles with sizes < 10 nm [106]. Nonetheless, young structures that are to evolve into mature soot structures can be characterized with TEM analysis [107]. In TEM analysis, a beam of electrons is transmitted through the soot particles which is an ultrathin specimen. The electrons pass through the specimen. The TEM scope operates similarly to a light microscope but employs electrons rather than light. Also, in the TEM scope, electromagnetic lenses are used instead of glass lenses. The high magnification capabilities of the TEM scope make this technique excellent for analyzing soot particles which have diameters less than a micrometer.

### 3.5 Chapter Summary

In this chapter the experimental approach for the study of soot formation in biodiesel oxygen enhanced coflow-diffusion flames was discussed. The fuels used in this study are No. 2 diesel and canola methyl ester (CME). The oxidizer stream was made up of various oxygen contents (21% to 80% $O_2$). Furthermore, the study of soot formation was possible with thermophoretic sampling and transmission electron microscopy (TEM) analysis. Finally, the following are provided in this chapter: (i) experimental set-up, (ii) burner configuration, (ii) an overview of the studied flames, (iii) thermophoretic sampling, (iv) TEM grid, and (v) an overview of TEM analysis.

# Chapter 4 – Evolution of soot in Diesel and CME flames

In the present work the effect of oxygen content in soot formation is investigated by using various oxygen contents. The fuels used in this study are No. 2 diesel and canola methyl ester (CME). The transportation sector plays a major role in soot emissions and diesel engines are very common in this sector. Diesel fuel is used in this study given its commonality in internal combustion engines (diesel engines). This petro-fuel can emit harmful emissions into our environment which is why renewable energy alternatives and oxygen enhanced combustion are opportunities to decrease soot emissions and other harmful pollutants. Biodiesel (BD) could potentially replace diesel fuel in the future. In these experiments, diesel is used as a basis of comparison with BD flames. That is, the same experiments using diesel are repeated with BD.

The purpose of this chapter is to present a detailed description of the evolution of soot particle formation along the centerline of a coflow laminar diffusion flame with air and oxygen enriched air. The oxygen content in the oxidizer stream consists of 21% (air), 35%, 50%, and 80% $O_2$. These oxygen conditions were chosen as to provide a good range of oxygen levels and study its effect on soot formation following what prominent authors of oxy/fuel combustion have done in the past [34, 41]. To investigate the effects of oxygen enhanced combustion the air flame (21% $O_2$) is used as a reference flame for comparison with the oxygen enhanced flames. The results from Merchan-Merchan et al. [33] are used in this present work as a basis for comparison with the oxygen enhanced flames. Merchan-Merchan and coworkers used co-flow diffusion air flames of CME and diesel to study soot evolution.

In this study, the flame is derived from the combustion of diesel and CME. The soot particles collected by the thermophoretic sampling technique underwent transmission electron microscopy (TEM) analysis. In this chapter the following are discussed: soot evolution, morphology (primary particle diameter), and soot formation process (inception, surface growth, agglomeration, and oxidation). Low resolution TEM images of collected soot samples reveal regions of particulate inception, surface growth, agglomeration, and oxidation. Plots are presented at the end of the chapter that show the primary particle diameter ($d_p$) versus height above burner (HAB) for each of the flames. Also, a plot with the peak $d_p$ versus the oxygen content in the oxidizer stream is provided. Medium resolution TEM images were used to measure the size of representative particles and obtain the $d_p$ values. The particle diameter profiles were obtained by measuring representative particles in the TEM images collected at medium resolution. The $d_p$ was obtained using Adobe Photoshop to measure the diameter of the representative particles in pixels. The pixel values were converted to nanometers (nm) which is the unit of measurement used for $d_p$. The soot $d_p$ values displayed in the plots represent the arithmetic average at the various flame heights and conditions along the flame centerline.

## 4.1 Soot evolution of diesel-air flames and using various oxygen contents in the oxidizer stream

Figure 10 displays the graphs of primary particle diameter ($d_p$) vs. height above the burner (HAB) of diesel flames at various oxygen contents. Representative medium resolution TEM images are incorporated in the plots (Fig. 10). The medium resolution TEM images are used to measure the representative soot particles to obtain $d_p$ values. The representative TEM images are color-coded with the point they represent on the curves (Fig. 10). Figure 10(a) displays the graph for diesel/21%

$O_2$ (air) adapted from the work of Merchan-Merchan et al. [33]. Figure 10(b) displays the graph for diesel/35% $O_2$, (Fig. 10(c)) for diesel/50% $O_2$, and (Fig. 10(d)) for diesel/80% $O_2$.

The general soot formation process for diesel/21% $O_2$ (air) in (Fig. 10(a)) is used as a basis for comparison to CME and oxy/fuel flames. Soot inception takes place at the lower region of the flame. As the soot particles continue to travel in the direction of the tip of the flame (buoyancy) their surface growth develops. Surface growth arises when the young soot particles stick together as displayed in in the TEM images collected from samples at HAB = 9 mm (color-coded purple, Fig. 10(a)). A strong effect of surface growth on soot morphology exists at low and intermediate heights of the flame, as established by Megaridis et al. [108]. Then agglomeration starts at HAB = 15 mm (color-coded orange, Fig. 10(a)) where more particles are sticking together creating larger clusters of soot. According to Merchan-Merchan et al. soot aggregates are shorter and of higher density and surrounded by nearly spherical singlet particulates are seen near the halfway point of the flame, HAB = 15 mm [33]. Megaridis et al. established that aggregates depict discrete rigid entities composed of extensively coalesced primary particles fused [108]. After the soot particles have agglomerated, they start forming long aggregates (color-coded blue, Fig. 10(a)) at HAB = 21 mm. Finally, the oxidation process of the soot particles begins, and the long aggregates are suppressed. Particles then move toward higher regions of the flame, and large clusters dominate showing smaller $d_p$ and a high degree of agglomeration [108]. The highest sampled flame height (HAB = 33 mm) shows that soot is undergoing an oxidation process by the significant decrease in their diameter (color-coded red, Fig. 10(a)).

Observing the lowest flame height (color-coded green) images from oxy/fuel diesel flames (Fig. 10(b), (c), (d)) a significant change of the soot appearance occurs. In diesel/35% $O_2$ (Fig. 10(b)) the TEM image of soot particles sampled at the lower part of the flame appear to be composed of a high degree of singlet or young soot/soot precursors. As the oxygen content is further increased to 50% there are fewer precursors present in (Fig. 10(c)) when compared to diesel/35% $O_2$. Also, surface growth begins near the burner mouth in the diesel/50% $O_2$ flame (Fig. 10(c)). Increasing the oxygen in the oxidizer to the highest content tested (80%), short aggregates with precursors are present in diesel/80% $O_2$ (Fig. 10(d)).

The diesel/35% $O_2$ flame (Fig. 10(b)) behaves differently than the diesel/21% $O_2$ (air) flame (Fig. 10(a)). In the diesel/35% $O_2$ long aggregates are found at the halfway point of the flame, HAB = 9 mm (color-coded orange, Fig. 10(b)). Then oxidation develops very quickly, and the long aggregates are suppressed to soot clusters with a smaller $d_p$, HAB = 21 mm (color-coded red). A very drastic decrease from mid flame height to the tip of the flame is seen in the $d_p$ value as the oxygen content is further increased in diesel/50% $O_2$ and diesel/80% $O_2$. Regarding the drastic decrease in $d_p$.

There are short aggregates with singlet particles present in the diesel/50% $O_2$ at a mid-flame HAB of 8.5 mm (color-coded orange, (Fig. 10(c)). Then at the mid-flame height for diesel/80% $O_2$, at HAB = 6 mm there are short aggregates present (color-coded orange, Fig. 10(d)). At the flame tip (color-coded red), all flames are analogous in that oxidation occurs and the aggregates have a smaller $d_p$, when compared to the $d_p$ obtained at mid-flame height.

Our analysis of collected samples using TEM imaging show that indeed the oxygen-enhanced combustion tends to suppress the formation of long aggregates. Concentrating on the tip of the flames (color-coded red) images of (Fig. 10(a), (b), (c), (d)) allows us to understand how the oxygen increase affects the oxidation of soot particles at those flame locations. The particles forming the aggregates are decreasing in size as the oxygen content increases. The $d_p$ profile shows that as the soot particles travel along the flame volume in the direction of the flame tip (Fig. 10(a)) from HAB = 9 to 33 mm the $d_p$ value increases rapidly from a lower part of the flame to the peak $d_p$ value. The diesel/air flame $d_p$ decreases gradually from the peak $d_p$ to the highest sampled position. Contrarily, in the oxygen-enhanced flames, the $d_p$ value decreases abruptly. The flame in (Fig. 10(b)) height above burner values range from 4 to 21 mm, in (Fig. 10(c)) ranges from HAB = 2.9 to 11.5 mm, and in (Fig. 10(d)) ranges from HAB = 3 to 8 mm. The oxygen enriched air flames (Fig. 10(b), (c), (d)) all show that $d_p$ decreases rapidly to the highest HAB.

This dramatic decrease in $d_p$ as oxygen content increases shows the soot formation process is accelerated. A striking trend is found when considering the peak $d_p$ value vs. the oxygen content % $O_2$. The peak $d_p$ value increases from 21% $O_2$ (air) to 35% $O_2$ and then decreases below the peak $d_p$ value of air for 50% $O_2$ and 80% $O_2$. Diesel/35% $O_2$ (Fig. 10(b)) shows the highest peak $d_p$ value ~42.9 nm compared to (Fig. 10(a), (c), (d)) with ~38.5 nm, ~36.8 nm and ~17.3 nm, respectively. Lee and coworkers used 21% $O_2$ (air), 50% $O_2$, and 100% $O_2$ to study the soot formation of laminar coannular non-premixed methane flames. In that study, methane/50% experienced the same sequence of events (inception, growth, and oxidation) as methane/air flame, but in a much shorter period. The reasons reported for a larger peak $d_p$ value in methane/50% $O_2$ than in methane/air are

as follows. The reduced residence times in oxygen-enriched flames tend to inhibit soot growth. Oxy/fuel flames enhance soot formation due to higher temperatures and promote soot oxidative mechanisms. Furthermore, the soot surface growth rates are much stronger under oxy/fuel conditions given the similar peak $d_p$ values observed for methane/air and methane/50% $O_2$ [34]. A comparable trend to Lee and coworkers (gaseous fuel) is found in the present study (vaporized fuels). The diesel/35% $O_2$ shows the highest peak $d_p$ value and diesel/air and diesel/50% $O_2$ have similar peak $d_p$ values.

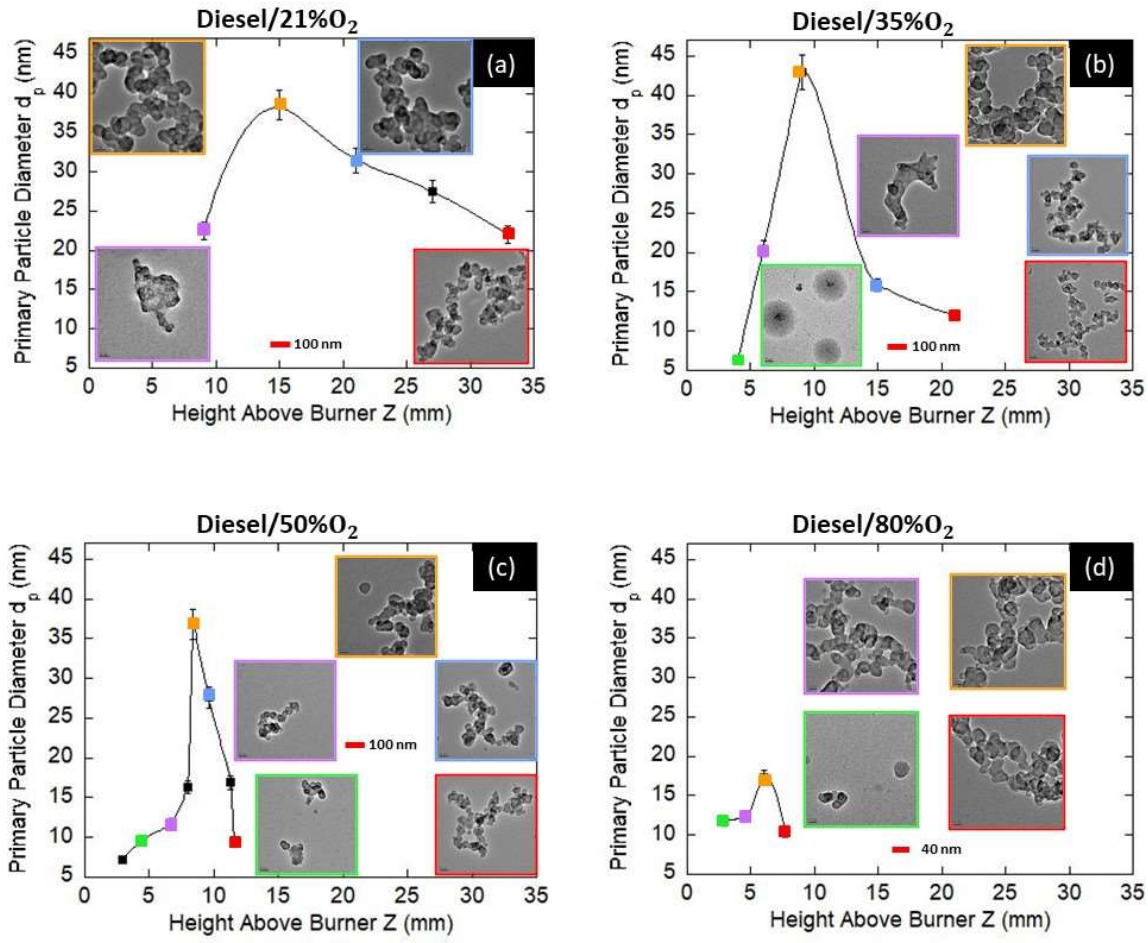


***Figure 10:*** *The plots represent the average primary particle diameter ($d_p$) with respect to the axial sampled heights for the DIESEL flames tested at different flame heights above the burner (HAB). The DIESEL flames are formed using various oxygen concentrations in the oxidizer (the balance is $N_2$): (a) 21% (air) [33], (b) 35%, (c) 50%, and (d) 80%. Each curve contains TEM images of the representative particles at the different flame heights.*

*4.1.1 Soot Evolution of Diesel/21% $O_2$ (Air)*

The low-resolution TEM images displayed in Fig. 11(a1) -(e1) show the particle formation in diesel/21% $O_2$ (air). TEM images in Fig. 11(a2) -(e2) show the variation of the particle diameter present along the axis of the studied flame. Approximately a dozen of these medium-resolution

TEM images were used at each position for obtaining the $d_p$ value of the diesel oxygen enriched air flames. Figure 11 displays the evolution of carbon particulates present in diesel/21% $O_2$ (air) flame at different HAB along the axial direction of the flame. The diesel air flame is used as a basis for comparison as the oxygen concentration is increased in the diesel flames and CME flames. The soot evolution profile of the diesel/21% $O_2$ (air) is obtained by analyzing soot samples at HAB = 6, 9, 15, 21, and 33 mm.

The collected TEM image (Fig. 11(a1)) near the burner mouth displays several precursors surrounded by larger particles. It is clear from Fig. 11(a1) that soot inception takes place at the lower region of the flame. As the soot particles continue to travel in the flame, surface growth develops. Agglomeration of aggregates is visible (Fig. 11(b1)) at a HAB = 9 mm. Surface growth arises when the young soot particles stick together as displayed in in the TEM images collected from samples at HAB = 9 mm in Fig. 11(b1). Near mid-flame height (HAB = 15 mm), soot aggregates are shorter and of higher density and surrounded by nearly spherical singlet particulates (Fig. 11(c1)).

A strong effect of surface growth on soot morphology exists at low and intermediate heights of the flame, as established by Dobbins et al. [108]. Agglomeration takes place after surface growth. The aggregates first combine prior to forming long chains. Dobbins et al. established that aggregates depict discrete rigid entities composed of extensively coalesced primary particles fused [108]. After the soot particles have agglomerated, they start forming long aggregates by aggregate-aggregate coalitions (HAB = 21 mm) in Fig. 11(d1). It is apparent that upper in the flame height

(HAB = 21 mm) the characteristics of the soot is that they are mainly composed of long chain of aggregates with a large primary particle diameter (Fig. 11(d1)). Finally, near the flame tip (HAB = 33 mm) the aggregates appear to be shorter, and they are composed of smaller primary particle diameter. Furthermore, the oxidation process of the soot particles begins, and the long aggregates are suppressed. Particles then move toward higher regions of the flame, and large clusters dominate showing smaller $d_p$ and a high degree of agglomeration [108]. The highest sampled flame height (HAB = 33 mm) shows that soot is undergoing an oxidation process in Fig. 11(e1).

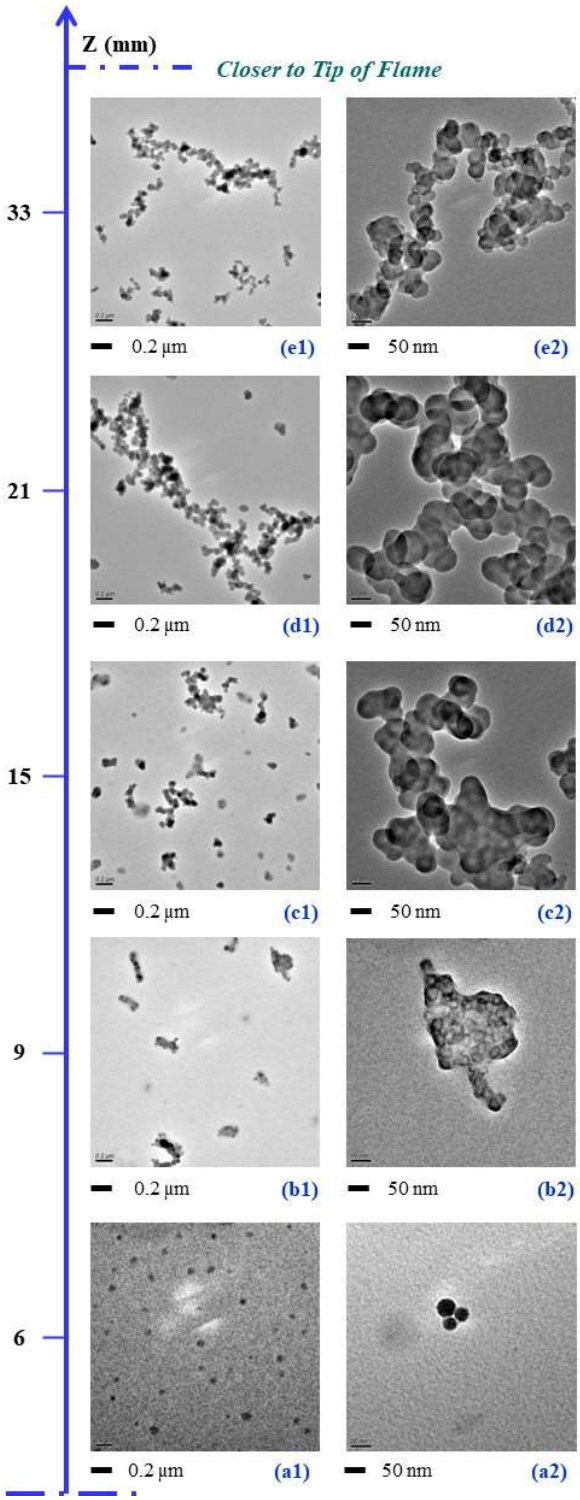


***Figure 11:*** *Representative progression of the soot evolution in a Diesel-21%$O_2$ (air) flame through low resolution TEM images collected from samples extracted along the central axis of the flame at various heights above the burner (HAB) of 6.0, 9.0, 15.0, 21.0, and 33.0 mm [33].*

*4.1.2 Soot Evolution of Diesel/35% $O_2$*

The introduction of 35% oxygen in the oxidizer stream decreased the axial length of the diesel flame compared to that when using air (21% $O_2$). The highest region of the soot analyzed for creating the 35% $O_2$ soot profile is 21 mm compared to 33 mm when using 21% $O_2$. The soot evolution profile of diesel/35% $O_2$ was obtained by analyzing soot particulates at a HAB = 4, 6, 9, 15, and 21 mm. Figure 12 displays the evolution of carbon particulates present in diesel/35% $O_2$. The low-resolution TEM images displayed in Fig. 12(a1) -(e1) show the evolution of soot formation along the diesel/35% $O_2$. Fig. 12(a2) -(e2) show the centerline particle diameter variation of the primary particles.

TEM images of samples collected at the lowest region of the flame (HAB = 4 mm) shows a high number of singlet "irregular" particles with a polydisperse size distribution Fig. 12(a1). Some of these single "irregular" particles are large in diameter more than a few hundred nanometers (as pointed out with white arrow in Fig. 12(a1)) while others have a few tens of a nanometer. Regardless of their size it appears that these structures have some inclusions at their core of the particle (material of darker contrast as shown by white arrows in Fig. 12(a2). Similar particles were observed at the bottom of the diesel/21% $O_2$ flame; however, it appears that the density of these structures increased when the oxygen concentration was increased to 35% $O_2$. At a height of HAB = 6 mm, there are short soot aggregates present surrounded with singlet particles Fig. 12(b1). Analogous to the air flame as the hot gases travel in the direction of the tip of the diesel/35% $O_2$ flame aggregates collide with other aggregates to form longer aggregates as shown in Fig. 12(c1). The effect of particle oxidation is evident by the reduction of the soot primary particle diameter in the aggregates as evident in Fig. 12(d1) and Fig. 12(e1).

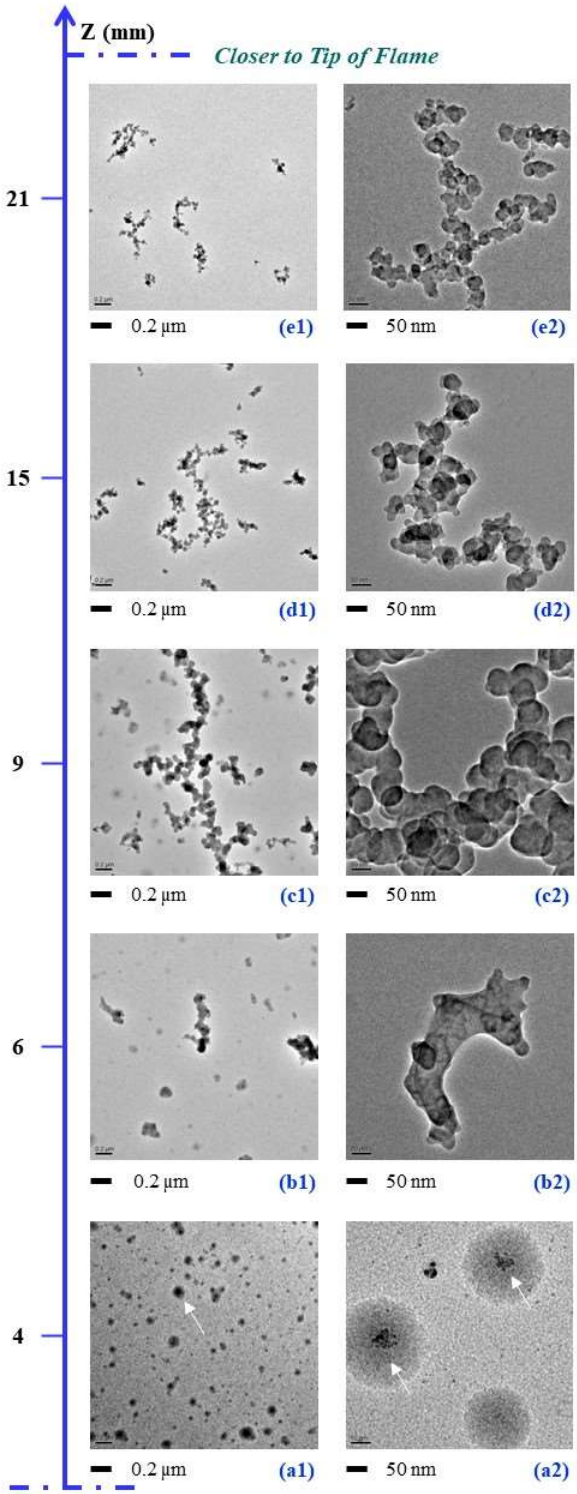


***Figure 12:*** *Representative progression of the soot evolution in a Diesel-35%$O_2$ flame through low resolution TEM images collected from samples extracted along the central axis of the flame at various heights above the burner (HAB) of 4.0, 6.0, 9.0, 15.0, and 21.0 mm.*

*4.1.3 Soot Evolution of Diesel/50% $O_2$*

Further increasing the oxygen content to 50% in the oxidizer stream the soot evolution is obtained. The soot evolution is composed by representative TEM images collected in the flame at HAB of 4.5; 6.5, 8.5, 9.5, and 11.5 mm. Figure 13 displays the diesel/50% $O_2$ flame soot evolution along the centerline. The low-resolution TEM images displayed in Fig. 13(a1) -(e1) show the particle evolution along the axis of the flame. The increase of oxygen to 50% $O_2$ in the oxidizer stream reduces the diesel flame length to about a third of the 21% $O_2$. It is fascinating to note that the entire soot evolution profile in the 50% $O_2$ diesel flame is obtained within 11.5 mm compared to 33 mm (air) and 21 mm for 35% $O_2$.

The medium resolution images Fig. 13(a2) -(e2) show the variation of primary particle diameter. Approximately a dozen medium resolution TEM images were used for obtaining the $d_p$ values. Near the burner mouth at HAB of 4.5 mm the soot samples are composed of single particles of a light contrast (pointed by the white arrows in Fig. 13(a1)) surrounded by a few agglomerates formed of a small number of primary particles (black arrow, Fig. 13(a1)). The application of medium resolution gives more clear insights of these light contrast single particles as pointed out by white arrows in Fig. 13(a2). As explained in the previously studied flames these small soot agglomerates pointed out by black arrows are trapped on the TEM grid as it pierces the outer flame traveling to the center.

At the HAB of 6.5 mm short aggregates start to form and are accompanied with singlet particles of lighter contrast. The light contrast nature and size of these particles could be difficult to identify

under the electron microscope (pointed out by white arrows) at HAB = 6.5 mm in Fig. 13(b1). At HAB = 8.5 mm the size of the primary particle appears to be larger and the formed soot aggregates appear to be longer Fig. 13(c1). Then long chains of soot aggregates are present at HAB = 9.5 mm as displayed in Fig. 13(d1). Finally, near the flame tip at HAB = 11.5 mm the aggregates are suppressed to short chains Fig. 13(e1).

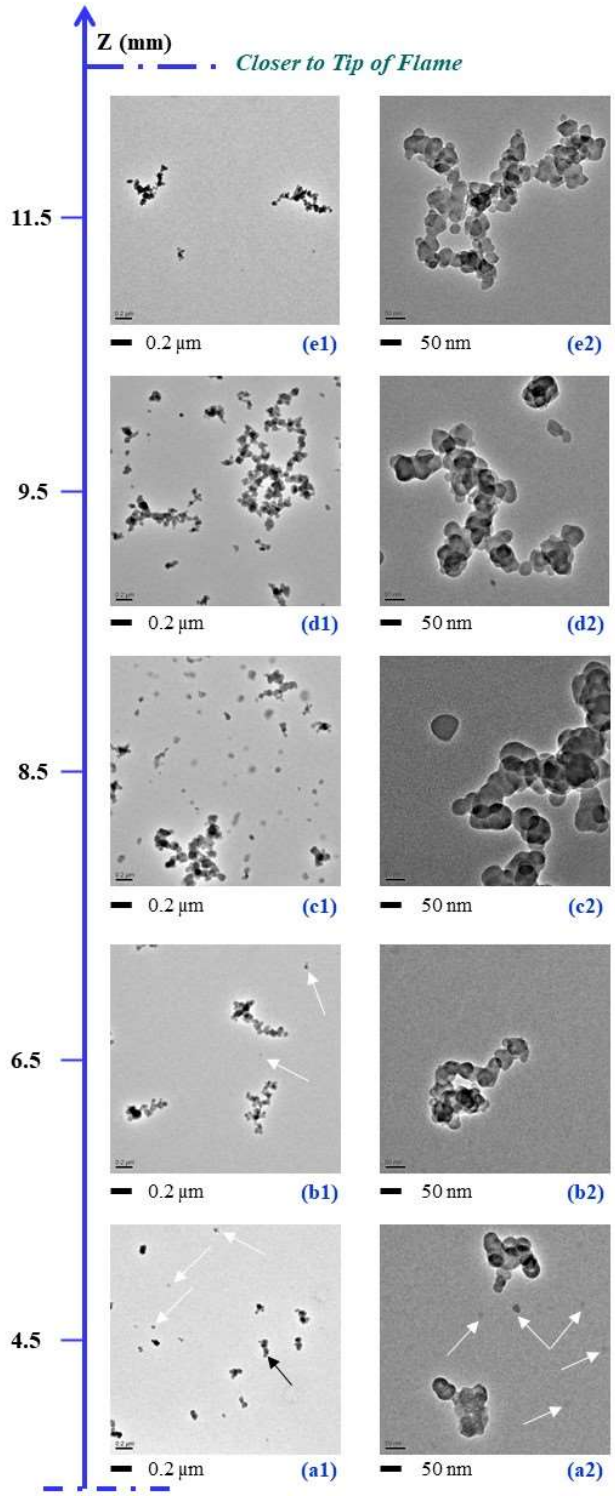


***Figure 13:*** *Representative progression of the soot evolution in a Diesel-50%$O_2$ flame through low resolution TEM images collected from samples extracted along the central axis of the flame at various heights above the burner (HAB) of 4.5, 6.5, 8.5, 9.5, and 11.5 mm.*

*4.1.4 Soot Evolution of Diesel/80% $O_2$*

Finally, we increased the oxygen enriched air to 80% $O_2$ in the diesel formed flame. The soot evolution at different HAB in the axial direction of the diesel/80% $O_2$ flame is displayed in figure 14. The sampled heights for the diesel/80% $O_2$ are 3, 5, 6 and 8 mm. The entire soot evolution profile for the highest content of oxygen tested in this study (80% $O_2$ content) was obtained from analyzing the samples within 8 mm as the flame length was further reduced (Figure 14).

At the lowest part of the flame (HAB of 3 mm Fig. 14(a1)) the presence of singlet particles is apparent. The higher number of singlet particles (precursor-like materials) are very evident in the 80% $O_2$ flame compared to diesel/21%, diesel/35%, and diesel/50% $O_2$. Black arrows in Fig. 14(a1) point out smaller particles with a darker contrast under the electron beam. The presence of the singlet "irregular" particles or single particles with a polydisperse size distribution as observed in the other diesel flames formed of lower oxygen concentrations is not evident for the diesel/80% $O_2$.

Two main trends are found when comparing between lower oxygen concentration flames and diesel/80% $O_2$: i) the overall length of the soot aggregates become much shorter as the oxygen concentration increases in the oxidizer stream; ii) the TEM images for this oxygen concentration look much cleaner. The TEM images collected from grids inserted at the medium and upper flame regions appear to have less trapped material for the 80% $O_2$. It can be observed on images collected from TEM grids inserted in the upper region of the diesel/21% $O_2$ and diesel/35% $O_2$ flames that a few aggregates cover most of the image space of Fig. 11(d1) and Fig. 12(c1). A similar situation

arises in the diesel/50% $O_2$ flame Fig. 13(d1). In the diesel/80% $O_2$ flame the aggregates have significantly oxidized (Fig. 14(d1)) and several aggregates are evident in a single TEM image.

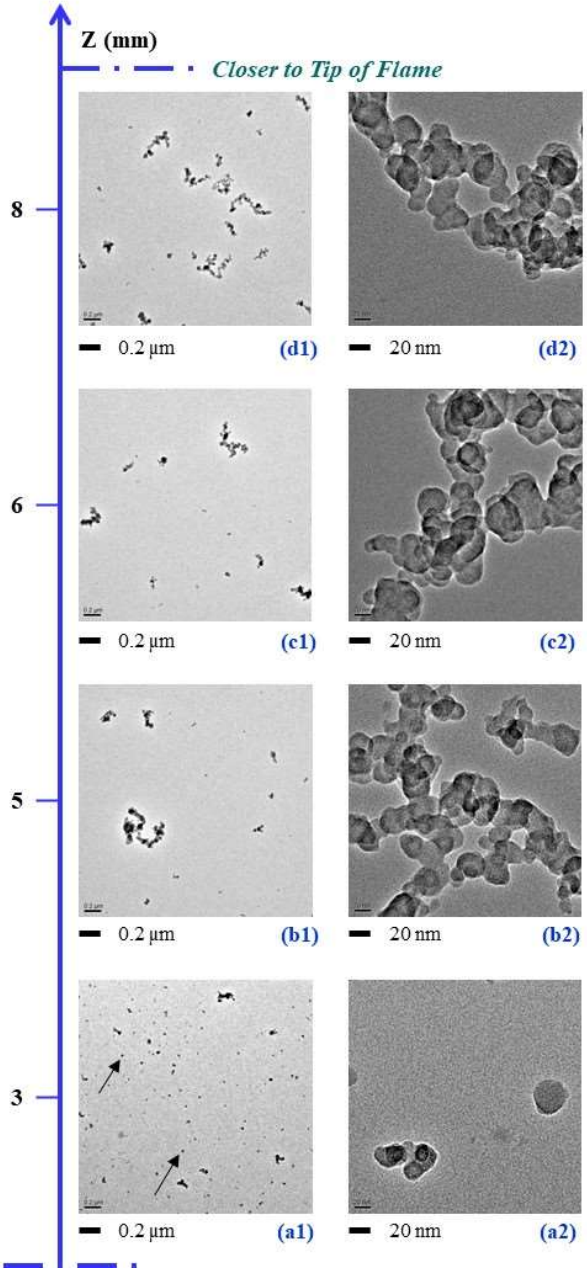


***Figure 14:*** *Representative progression of the soot evolution in a Diesel-80%$O_2$ flame through low resolution TEM images collected from samples extracted along the central axis of the flame at various heights above the burner (HAB) of 3.0, 5.0, 6.0, and 8.0 mm.*

### 4.2 Soot evolution of CME with air and various oxygen contents in the oxidizer stream

Figure 15 displays the graphs of primary particle diameter ($d_p$) vs. height above burner (HAB) of canola methyl ester (CME) flames. Additionally, (Fig. 15) displays the representative medium resolution TEM images. The representative TEM images are color-coded with the point they represent on the curves of (Fig. 15). (Fig. 15(a)) displays the graph for CME/21% $O_2$ (air) adapted from the work of Merchan-Merchan et al. [33]. (Fig. 15(b)) displays the graph of CME/35% $O_2$, (Fig. 15(c)) of CME/50% $O_2$, and (Fig. 15(d)) of CME/80% $O_2$.

Figure 15(a) shows representative medium-resolution images displayed at each sampled HAB from soot samples collected from CME/21% $O_2$ (air) flame. The data in (Fig. 15(a)) was adapted from the work of Merchan-Merchan et al. In that work CME/air showed large irregular-shaped fragments containing complex structural morphology along the centerline of the flame [33]. The TEM images show the evolution of soot. Singlet soot particles in the lower region of the flame transform into long aggregates as they travel from a region near the burner mouth to the flame tip. At the lowest HAB = 6.5 mm sampling position the image (color-coded green) displays few precursors and some irregularly shaped clusters. Merchan-Merchan et al. found that precursors are not necessarily spherical [33]. At a height of HAB = 9 mm (color-coded purple), surface growth is apparent with very small aggregates and young soot present. There are also some "globules" present in this image as pointed out by the works of Merchan-Merchan et al. [33]. Agglomeration begins to occur at the peak $d_p$ value of the curve at a height of HAB = 15 mm. Short aggregates and surface growth are visible in this image (color-coded orange). It is interesting to see some of the particulates appearing as of a lighter contrast. Finally, near the tip of the flame at HAB = 21

mm, where oxidation is taking place, the aggregates present are very long, and the particle diameters have decreased in size.

A comparison of the TEM images in (Fig. 15) can yield some insight information on the effect that the increase of oxygen content has on soot formation. The TEM images at the root of the flame for oxygen-enhanced CME flames (Fig. 15(b)-(d)) have short soot aggregates that are accompanied by singlet soot particulates. Resembling our studies in the diesel with oxygen enriched air flames short aggregates were probably collected when the probe pierced through the soot annulus during insertion and as reported by others [34]. The singlet soot particulates are not very visible now that the oxygen percentage in the oxidizer is increased. Then, analyzing the surface growth zone of the CME flames (color-coded purple). In the CME/21% $O_2$ flame (Fig. 15(a)) it appears that there are very small aggregates just beginning to form. Then as oxygen increases to 35% $O_2$ short aggregates beginning to form is observed (Fig. 15(b)). As the oxygen increases to a higher content of 50% $O_2$ a well-formed short aggregate is observed (Fig. 15(c)) than in the previous two flames discussed. At the peak $d_p$ value, agglomeration is visible (color-coded orange) for the CME flames at 21%, 35%, and 80% $O_2$. The aggregates noticeably decrease in size when comparing between the CME/air flame (Fig. 15(a)) to the CME/35% $O_2$ and CME/80% $O_2$ flames. In the CME/35% $O_2$ flame (Fig. 15 (b)), soot aggregates are accompanied by irregular structures referred to as "globules" in the literature [33]. In the CME/80% $O_2$ flame, there are precursors and very short aggregates (Fig. 15 (d)).

The oxygen increase alters the formation of the long aggregates in the CME flame. Studying the region on the curves of (Fig. 15(a), (b), (c)) where the oxidation process is dominant right after the

peak $d_p$ value (color-coded blue). The agglomerates appear to be shorter and less interconnected compared to the 21% $O_2$ and 35% $O_2$ flame. In (Fig. 15(a)) at HAB = 21 mm there is a very long aggregate with several branches. Then in (Fig. 15(b)) where the oxygen content has increased to 35% $O_2$ and the flame height is HAB = 9.5 mm, we see the aggregates have shorter branches than the ones in the CME/21% $O_2$ (air) flame. Also, it is interesting to note that in the CME/ 35% $O_2$ flame at the intermediate height the soot agglomerates are surrounded by singlet and liquid-like particles. Further increasing the oxygen content to 50% $O_2$ in (Fig. 15(c)) at HAB = 8.5 mm we see the aggregates are thinner and with smaller diameters than the ones in the CME/35% $O_2$ flame. Now looking at images gathered from the highest region of the tested flames in (Fig. 15(b)-(d)) (color-coded red). These images display the characteristics of soot oxidation in the oxygen-enhanced flames. We see that in CME/35% $O_2$ flame there is a very long aggregate that covers most of the image space. A different situation arises in the CME/50% $O_2$ flame. The aggregate present in (Fig. 15(c)) (color-coded red) is very short compared to the aggregates present in the CME/35% $O_2$ highest sampled flame height. Similarly, for the highest oxygen content tested the aggregates become even shorter and the particle diameter is extremely small in CME/80% $O_2$ in (Fig. 15(d)). The first two processes of soot formation (inception and surface growth) allow for an accelerated soot growth as the oxygen percentage increases. Then at the peak $d_p$ value the aggregates present decrease with the increase in oxygen. Then during the oxidation process, the aggregates become shorter in length as the oxygen content increases. Finally, near the flame tip, the oxygen increase allows for long aggregates to decrease in length.

The $d_p$ data for CME flames is gathered from the medium resolution images (Fig, 15(a)-(d)). In (Fig. 15(a)) the CME/21% $O_2$ sampled flame heights range from HAB = 6.5 to 21 mm. Then in

(Fig. 15(b)) the CME/35% $O_2$ range from HAB = 5.5 to 12 mm, (Fig. 15(c)) the CME/50% $O_2$ range from HAB = 5 to 9.5 mm, and (Fig. 15(d)) the CME/80% $O_2$ range from HAB = 3 to 4.5 mm. The curves which represent $d_p$ vs. HAB in (Fig, 15(a)-(d)) show the CME flames decrease in $d_p$ rapidly after the peak $d_p$ value. Examining the trend in CME flames of peak $d_p$ vs. oxygen content gives interesting results. The peak $d_p$ values are as follows: CME/21% $O_2$ is ~28 nm (Fig. 15(a)); CME/35% $O_2$ is ~28.6 nm (Fig. 15(b)); CME/50% $O_2$ is ~24 nm (Fig. 15(c)); and CME/80% $O_2$ is ~12.5 nm (Fig. 15(d)). Notice that CME/35% $O_2$ has the highest peak $d_p$ value compared to CME/21% $O_2$, CME/50% $O_2$ and CME/80% $O_2$. As explained earlier, Lee et al. found a reciprocal trend when comparing peak $d_p$ values and oxygen content in methane flames [34]. Still, in the CME flames, a drop in $d_p$ value after the peak $d_p$ accelerates as oxygen content increases. A larger drop in $d_p$ value is obtained for oxy/fuel flames than air.

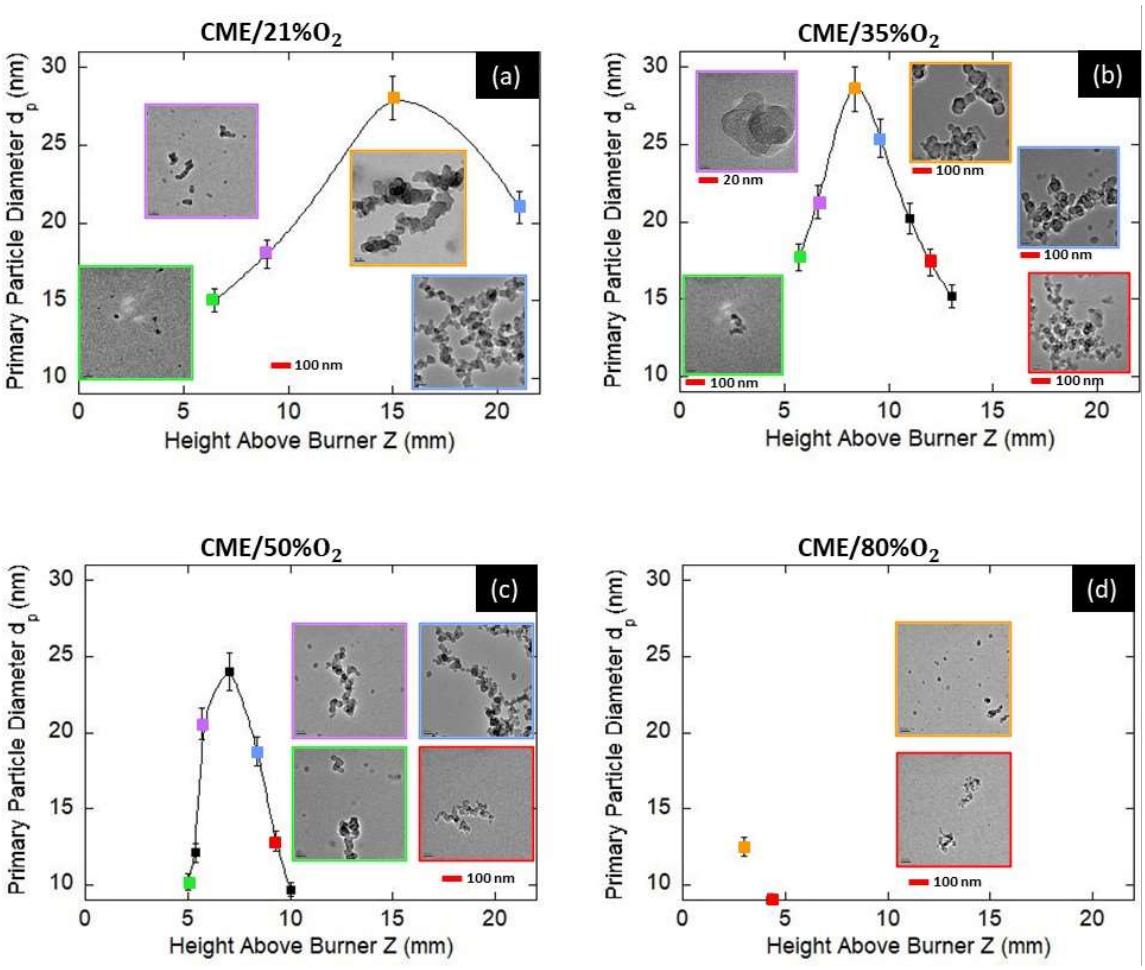


***Figure 15:*** *The plots represent the average primary particle diameter ($d_p$) with respect to the axial sampled heights for the CME flames tested at different flame heights above the burner (HAB). The CME flames are formed using various oxygen concentrations in the oxidizer (the balance is $N_2$): (a) 21% (air), (b) 35%, (c) 50%, and (d) 80%. Each curve contains TEM images of the representative particles at the different flame heights.*

*4.2.1 Soot Evolution of CME/21% $O_2$ (Air)*

Resembling the diesel flames, TEM image analysis was obtained for CME air and oxygen enriched air flames. Like the diesel flames, the CME-air flame is used as a basis of comparison with the

oxygen enhanced CME flames. The sampled heights for the CME/21% $O_2$ (air) are as follows: 6.5, 9, 15, and 21 mm. The data in (Fig. 16) was adapted from the work of Merchan-Merchan et al. In that work CME-air showed large irregular-shaped fragments containing complex structural morphology along the centerline of the flame [33]. Figure 16 displays the morphological characteristics of soot particulates present in CME/21% $O_2$ (air) flame at different heights above burner (HAB) in the axial direction.

The low-resolution TEM images, Fig. 16(a1) -(d1), reveal the evolution of soot formation along the flame axis. Singlet or "young soot" particles are present closer to the fuel nozzle to fully soot agglomerates or "mature soot" near the flame tip. At the lowest HAB = 6.5 mm sampling position the image displays precursors and some irregularly shaped clusters as pointed out by a white arrow (Fig. 16(a1)). Merchan-Merchan et al. found that precursors are not necessarily spherical [33]. A closer look at the non-spherical precursors in Fig. 16(a2) are pointed out by white arrows. There are also some "globules" present in this image (Fig. 16(b1)) as pointed out by the works of Merchan-Merchan et al. [33]. A globule of lighter contrast is pointed out by a white arrow and globules of a darker contrast is pointed out by a black arrow (Fig. 16(b1)). At this HAB of 9 mm, surface growth is apparent with very small aggregates and young soot present. In the CME/21% $O_2$ (air) flame, large "globules" of a couple hundred of nanometers in diameter are observed in the TEM images of the sample collected at HAB = 9 mm as pointed out by the black arrow in Fig. 16(b1). "Globules" with smaller diameters appear to be of a lighter contrast under the electron beam as pointed out with a white arrow in Fig. 16(b1).

It is interesting to see in Fig. 16(c1) some particulates appearing with a lighter contrast (see white arrows). Short aggregates and surface growth are visible at the peak $d_p$ value of HAB = 15 mm, Fig. 16(c1). At HAB = 15 mm soot agglomerates composed of tens of particles are accompanied by a higher number of "globules" Fig. 16(c1). The "globules" at this flame position appear to be smaller in size. It is also evident that the "globules" contain embedded carbonized inclusions that are of a darker contrast shown by white arrows in Fig. 16(c1). As suggested by Merchan-Merchan et al. and Kholghy et al. these "globules" rapidly convert to fully developed aggregates composed of mature primary particles [33, 37]. Globules are fully carbonized in the upper region of the CME-air flame to form the long soot aggregates (Fig. 16(d1)). According to Merchan-Merchan et al. [33] a single "globule" can have multiple embedded carbonized inclusions and of different sizes. Also, it is suggested that "globules" serve as growth pathways for the formation of long fully carbonized aggregates composed of nearly spherical primary particles [33]. At HAB = 21 mm very long soot aggregates composed of hundreds of soot primary particles are present at this flame position (Fig. 16(d1)). The presence of "globules" at this flame position (HAB = 21 mm) is no longer observed because they have fully carbonized.

Regardless of the fuel (diesel or CME) the general soot formation process has a similar trend including inception, surface growth, agglomeration, and oxidation. Also, the soot formation process is resembling regardless of the total flame height. The CME-air flame is 7 mm shorter than the diesel-air flame, but the soot formation process is identical. When comparing diesel-air and CME-air the main difference is that the CME flame has the presence of globules and irregular shaped structures in the upper part of the flame. There are orderly and structured short aggregates

in the diesel-air flame (Fig. 11(b1)), whereas, in the CME-air flame has the presence of globules, surface growth beginning to occur, but no short aggregates present (Fig. 16(b1)).

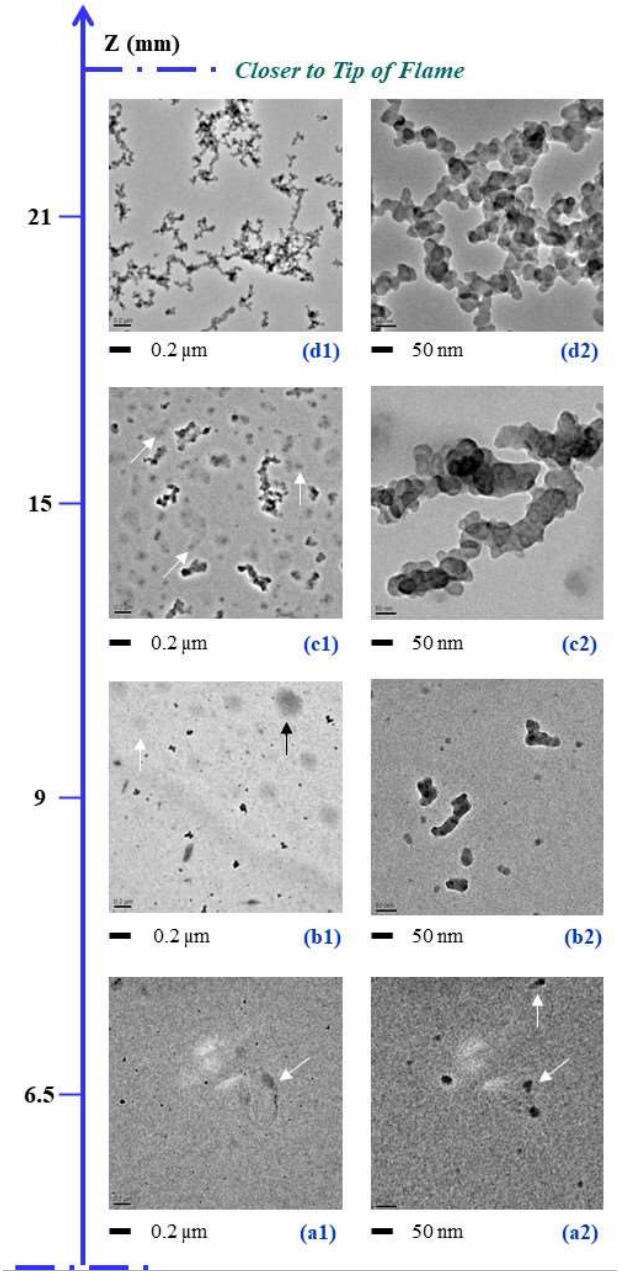


***Figure 16:*** *Representative progression of the soot evolution in an CME-21%$O_2$ (air) flame through low resolution TEM images collected from samples extracted along the central axis of the flame at various heights above the burner (HAB) of 6.5, 9.0, 15.0, and 21.0 mm [33].*

*4.2.2 Soot Evolution of CME/35% $O_2$*

Soot samples were collected along the CME/35% $O_2$ flame axis at different HAB including 5.5, 6.5, 8.5, 9.5, and 12 mm. The soot evolution of the CME flame with oxygen enriched air at 35% $O_2$ is displayed in figure 17. Evolution of soot formation along the flame axis is revealed by the low-resolution TEM images. The representative low-resolution images displayed at each sampled HAB from soot samples collected from CME/35% $O_2$ flame are shown by figure 17(a1) –(e1). Near the burner mouth, HAB = 5.5 mm, the image (Fig. 17(a1)) displays few short aggregates as pointed out with the black arrow and precursors (white arrows).

Soot precursors and singlet particles are typically present in the first step of soot formation which occurs at the lowest flame height. The short aggregates present near the burner mouth are most likely formed outside the center of the flame. According to Megaridis and Dobbins [97] there exist a strong convective and thermophoretic forces transport aggregates to the flame center and this is the reason short aggregates are accompanying the precursors present near the burner mouth as seen in Fig. 17(a1). The position of soot particles within the flame is a main factor for the size of the primary particles and the degree of agglomeration of the different aggregates [108, 109]. Therefore, the short aggregates present at the lowest flame height, Fig. 17(a1), are not representative. Also, a higher density of singlet particles is visible in Fig. 16(a1) from the CME/21% $O_2$ (air) flame when compared to Fig. 17(a1) in CME/35% $O_2$ flame. At HAB = 6.5 mm, shows surface growth occurring on the precursors (white arrows) and the aggregates (black arrow) seem shorter, Fig. 17(b1). Focusing on the lower flame heights (HAB = 4 to 6 mm) in the diesel/35% $O_2$ flame (Fig. 12(a1) -(b1)) and the lower flame heights (HAB = 5.5 to 6.5 mm) in the CME/35% $O_2$ flame (Fig. 17(a1) -(b1)). Near the burner mouth the diesel/35% $O_2$ flame (Fig.

12(a1)) dominates with numerous precursors whereas in the CME/35% $O_2$ flame (Fig. 17(a1)) there are hardly any precursors present. Furthermore, at a HAB of 6 mm in the diesel/35% $O_2$ flame (Fig. 12(b1)) there are various short aggregates present that are much larger than the few short aggregates present at HAB = 6.5 mm in the CME/35% $O_2$ flame (Fig. 17(b1)). This comparison demonstrates that the CME/35% $O_2$ flame burns much cleaner than diesel/35% $O_2$ flame at lower flame heights.

There are several liquid-like agglomerates (white arrows) with slightly larger aggregates (black arrow), Fig. 17(c1). Then the aggregates begin increasing in length and the liquid-like particles (white arrows) become darker, Fig. 17(d1). Finally, near the flame tip the aggregates are very long and irregular and the liquid-like particles have disappeared, Fig. 17(e1). There is a lesser density of particles at HAB = 9.5 mm compared to the aggregates at HAB = 12 mm. Figure 17(a2) –(e2) show representative medium-resolution images of soot samples collected from the CME/35% $O_2$ flame. A $d_p$ value was obtained at the different HAB as to study the variation of the particle diameter. The soot profile clearly shows the effect of soot inception, growth, and oxidation.

The soot evolution along the flame centerline of CME/21% $O_2$ (air) contains particle inception or single particles (bottom flame region), surface growth and agglomeration, and oxidation (upper flame region). The flame height (HAB of 21 mm) represents the highest sampled region of the CME/21% $O_2$ (air) flame and is near the flame tip (Fig. 16). The increase of oxygen content (35% $O_2$) in the oxidizer stream resulted in a shorter flame with the highest sampled position at the HAB of 12 mm (Fig. 17). Interestingly, within the 12 mm flame length the entire soot formation process

for this oxygen enriched air flame takes place. It is visible that particle inception in the oxygen enhanced flame occurs at a faster rate when comparing the soot evolutions of the CME/21%$O_2$ (air) (Fig. 16) and CME/35% $O_2$ (Fig. 17).

It is also interesting to note that the variation of the oxygen concentration influences the morphology of some "irregular-shaped" structures that accompanying soot particulates and have been referred in the literature as "globules" [33]. The presence of these "globules" structures have been observed only among the soot samples extracted thermophoretically from within flames formed with biodiesel and biodiesel surrogates [33]. These "globules" structures are large in size, have appearance of "liquid-like" characteristics and of a lighter contrast compared to the regular soot under the microscope.

In the CME/35% $O_2$ flame (Fig. 17) a high number of "irregular-shaped" structures or "globules" are accompanied by several soot aggregates with a low degree of agglomeration at HAB = 8.5 mm (Fig. 17(c1)). Throughout, it appears that the "globules" in this flame are smaller in size compared to the CME/21% $O_2$ (air) flame. The larger "globules" of very light contrast typically in the CME/21% $O_2$ (air) flame are not observed in the CME/35% $O_2$ flame. However, "globules" or "irregular-shaped" structures with darker and lighter contrast are still present among the soot as highlighted by the white arrows in Fig. 17(c1). TEM images of samples collected in this flame at the HAB = 9.5 mm show that the number of "globules" significantly decreased (Fig. 17(d1)) compared to the previous flame height. Only a few "globules" are evident at this flame height surrounding the soot aggregates pointed out by white arrows (Fig. 17(d1)). Figure 17(e1) shows

the morphology of the soot samples extracted at the flame HAB = 12 mm. The TEM image shows that the extracted samples are composed mostly of long fully agglomerated soot aggregates. “Globules” are no longer present in a zone near the tip of the flame (Fig. 17(e1)).

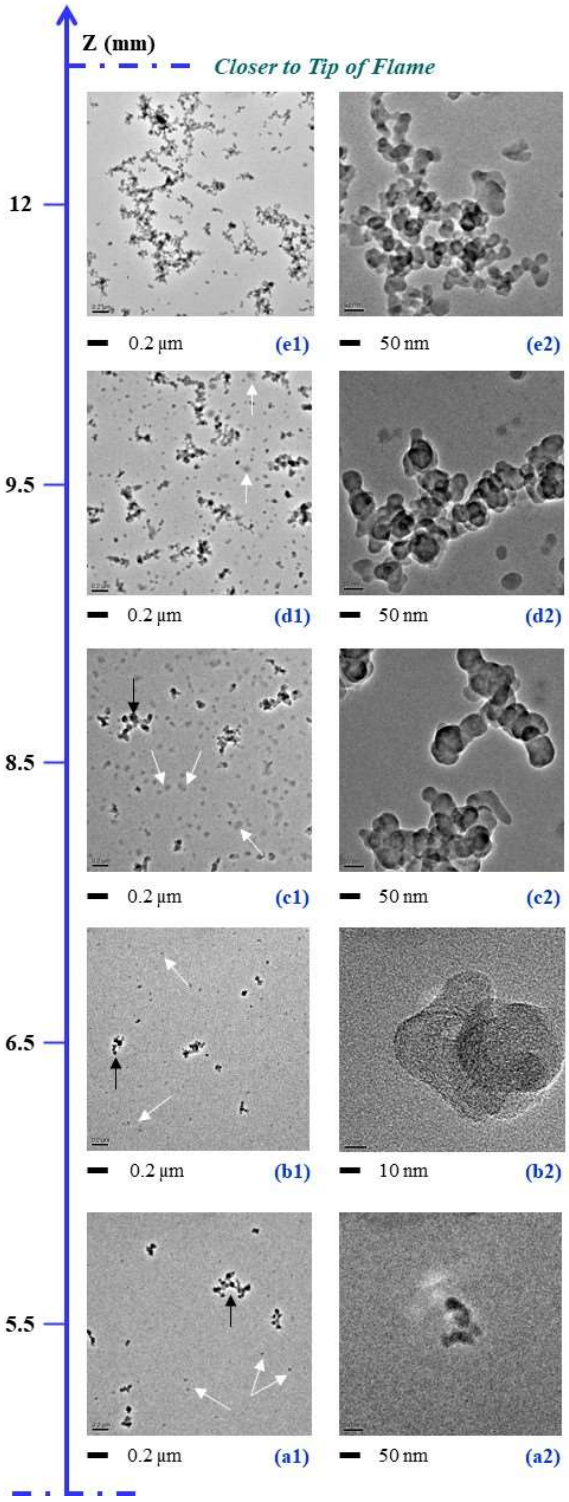


***Figure 17:*** *Representative progression of the soot evolution in a CME-35%$O_2$ flame through low resolution TEM images collected from samples extracted along the central axis of the flame at various heights above the burner (HAB) of 5.5, 6.5, 8.5, 9.5, and 12.0 mm.*

*4.2.3 Soot Evolution of CME/50% $O_2$*

Comparable to what was observed in the 35% $O_2$ oxygen CME flame, the variation of the oxygen concentration influenced the flame structure for CME/50% $O_2$. The HAB of 9.5 mm represents the highest axial sampled region of the CME/50% $O_2$ flame and is near the tip of the flame (Figure 18). Figure 18 displays the soot evolution at different HAB in the axial direction of the CME/50% $O_2$ flame. The soot evolution consists of particles analyzed at HAB = 3, 5, 6, 8.5, and 9.5 mm. Like the other oxygen concentration, the low-resolution TEM images displayed in Fig. 18(a1) -(e1) show the morphology of particle agglomeration collected from the CME/50% $O_2$ flame. The medium resolution images Fig. 18(a2) -(e2) show the variation of the size particle diameter along the CME/50% $O_2$ flame axis. The "liquid-like" characteristics structures appear to be present at the lower region of the flame (HAB = 3 mm) as shown in Fig. 18(a1) with a black arrow. In Fig. 18(a2) an "irregular-shaped" structure is pointed out by a black arrow. Close inspection of the TEM images (Fig. 18(a2-b2)) at HAB = 3 and 5 mm reveals that these "irregular-shaped" structures are surrounded by precursors or small diameter singlet particles (white arrows). Most of these precursors appear to be of a very lighter contrast under the electron microscope beam of the lower magnification TEM images (Fig. 18(a1-b1)). The illustrative single particles at HAB = 5 mm is pointed out by the white arrows Fig. 18(b1). Close inspection of the TEM image, Fig. 18(b1), shows the presence of high number of the singlet particles and this can be better observed in the medium resolution TEM in Fig. 18(b2) (white arrows). In the CME/35% $O_2$ flame there were aggregates present near the burner mouth. Similarly, in the present flame, CME/50% $O_2$, a short aggregate is present at the lower flame height (HAB = 5 mm) in Fig. 18(b1) as pointed out by the black arrow. Short aggregates are not representative of what occurs at the lower flame heights. As established previously in the CME/35% $O_2$ discussion, there are strong convective and

thermophoretic forces that transport aggregates to the flame center. This is the reason short aggregates are present near the burner mouth as seen in Fig. 18(b1).

At HAB = 6 mm the aggregates begin to grow in length and singlet particles are more evident at the lower magnification TEM images (Fig. 18(c1)). It is interesting to see such a drastic increase in the number of soot aggregates present in (Fig. 18(c1)) when compared to the previously discussed HAB of 5 mm (Fig. 18(b1)). This is interesting because there is only a one-millimeter difference between (Fig. 18(c1)) and (Fig. 18(b1)). At this flame position the soot aggregates are accompanied by some "irregular-shaped" structures as pointed out by a white arrow. These "irregular-shaped" structures are much smaller in size and are very transparent or of lighter contrast to the surrounding soot aggregates. Like the previous flames (21% and 35% $O_2$) the presence of fully agglomerated soot aggregates only is observed in the region near the tip of the flame (Fig. 18(d1)). The aggregates are formed from tens to hundreds of primary particles. The presence of "globules" structures is no longer present at this flame height (HAB = 8.5 mm).

Finally, oxidation begins to take its course and we see few aggregates with smaller particle diameter at HAB = 9.5 mm in Fig. 18(e1). TEM images of the samples extracted closest to the tip of the flame shows that the soot has been oxidized (Fig. 18(e1)). Analyzing the flames, diesel/50% $O_2$ (Fig. 13(d1)) and CME/50% $O_2$ (Fig. 18(e1)) near the flame tip, the CME/50% $O_2$ flame burns cleaner than diesel/50% $O_2$ flame. There are various long aggregates at an HAB of 9.5 mm in the diesel/50% $O_2$ flame whereas in CME/50% $O_2$ flame there are hardly any aggregates present at HAB = 9.5 mm because they have oxidized.

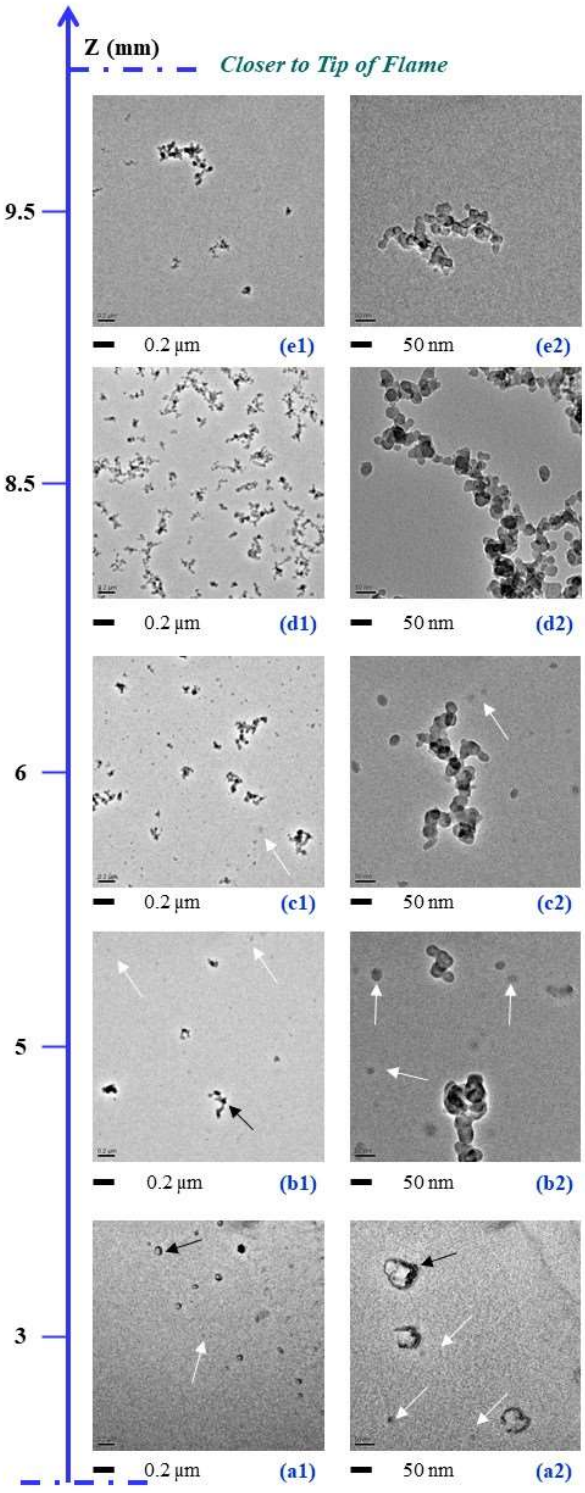


***Figure 18:*** *Representative progression of the soot evolution in a CME-50%$O_2$ flame through low resolution TEM images collected from samples extracted along the central axis of the flame at various heights above the burner (HAB) of 3.0, 5.0, 6.0, 8.5, and 9.5 mm.*

*4.2.4 Soot Evolution of CME/80% $O_2$*

The soot evolution profile of the CME/80% $O_2$ flame is composed of only two analyzed flame positions and this is due to following reasons: i) the introduction of 80% $O_2$ in the oxidizer stream significantly reduced the length of the flame and ii) the flame temperature tends to significantly increase as the oxygen content is increased and potentially burning the TEM grid. The soot evolution for the CME/80% $O_2$ consists of soot samples analyzed at HAB = 3 and 4.5 mm. Figure 19 displays the soot evolution at different HAB in the axial direction of CME/80% $O_2$ flame. Figure 19(a2) -(b2) show representative medium-resolution images displayed at each sampled HAB from soot samples collected from CME/80% $O_2$ flame.

Near the burner mouth at HAB = 3 mm there are singlet particles of light and dark contrast as pointed out by white and black arrows respectively (Figure 19(a1)). The singlet particles are accompanied of very small soot aggregates. Similar trends can be observed by comparing the obtained soot evolution profiles for both diesel and CME oxygen enhanced flames. It appears that regardless of the fuel type (diesel or CME) the introduction of 80% $O_2$ in the oxidizer stream resulted in a compressed or narrow flame region for the formation of soot precursors (Fig. 14(a1) and Fig. 19(a1)). It is interesting to see the TEM images at HAB of 3 mm for both flames of diesel/80% $O_2$ and CME/80% $O_2$ look very similar with soot precursors present and very small soot aggregates.

It appears that at the flame height of 4.5 mm most of the soot particles are oxidized at this flame region (Fig. 19(b1)). At HAB = 4.5 mm the singlet particles disappear, and a few short aggregates

are present. Also, at HAB = 4.5 mm it is obvious oxidation is occurring given there is hardly any soot particles left. The oxygen enhancement effect on the CME/80% $O_2$ flame is much more pronounced than in the diesel/80% $O_2$ flame. This is visible with the flame height reduction for the CME/80% $O_2$ flame when compared to the diesel/80% $O_2$ flame. The highest sampled height in the CME/80% $O_2$ flame (Fig. 19(b1)) is only 4.5 mm whereas in the diesel/80% $O_2$ flame (Fig. 14(d1)) it is 8 mm. The CME/80% $O_2$ flame is basically half the size of the diesel/80% $O_2$ flame when regarding the highest sampled height. Even more astonishing, is that the highest sampled height (4.5 mm) of the CME/80% $O_2$ flame is 16. 5 mm less than the highest sampled height of the CME-air flame.

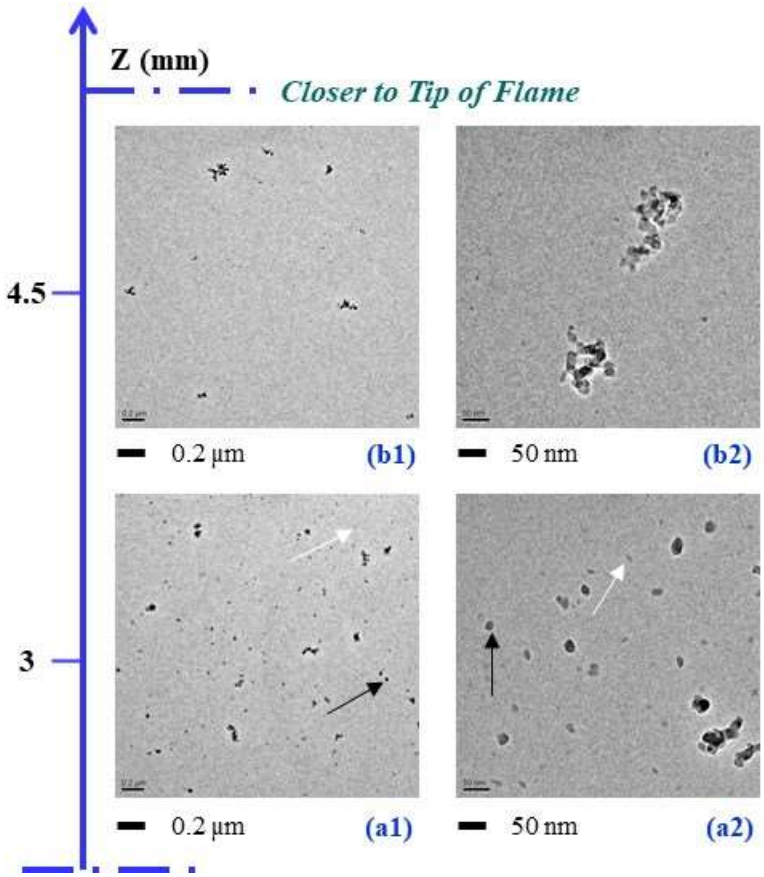


***Figure 19:*** *Representative progression of the soot evolution in a CME-80%$O_2$ flame through low resolution TEM images collected from samples extracted along the central axis of the flame at various heights above the burner (HAB) of 3.0, and 4.5 mm.*

### 4.3 Primary particle diameter of soot formed by diesel and CME with air and oxygen enriched air

Figures 20-22 display three different graphs with various plots that are identified by their respective graph keys. The diesel and CME flames are formed using four different oxygen concentrations in the oxidizer stream (the balance is $N_2$): 21% (air), 35%, 50%, and 80% $O_2$. The data gathered for all flames are represented by the average primary particle diameter ($d_p$) with

respect to the axial sampled heights at different flame HAB in Fig. 20–21. Finally, in Fig. 22 the largest $d_p$ with respect to the oxygen content in the oxidizer (% $O_2$) for both diesel and CME flames.

Figure 20 contains plots that represent the $d_p$ from soot samples collected from diesel air and oxygen-enhanced air flames at different HAB. Figure 20 displays the plot for diesel/21% $O_2$ (air) (color-coded black) adapted from the work of Merchan-Merchan et al. [33]. Figure 20 also displays the plots of diesel/35% $O_2$ (color-coded blue), diesel/50% $O_2$ (color-coded green), and diesel/80% $O_2$ (color-coded red). The $d_p$ data for diesel flames is gathered from the medium resolution images.

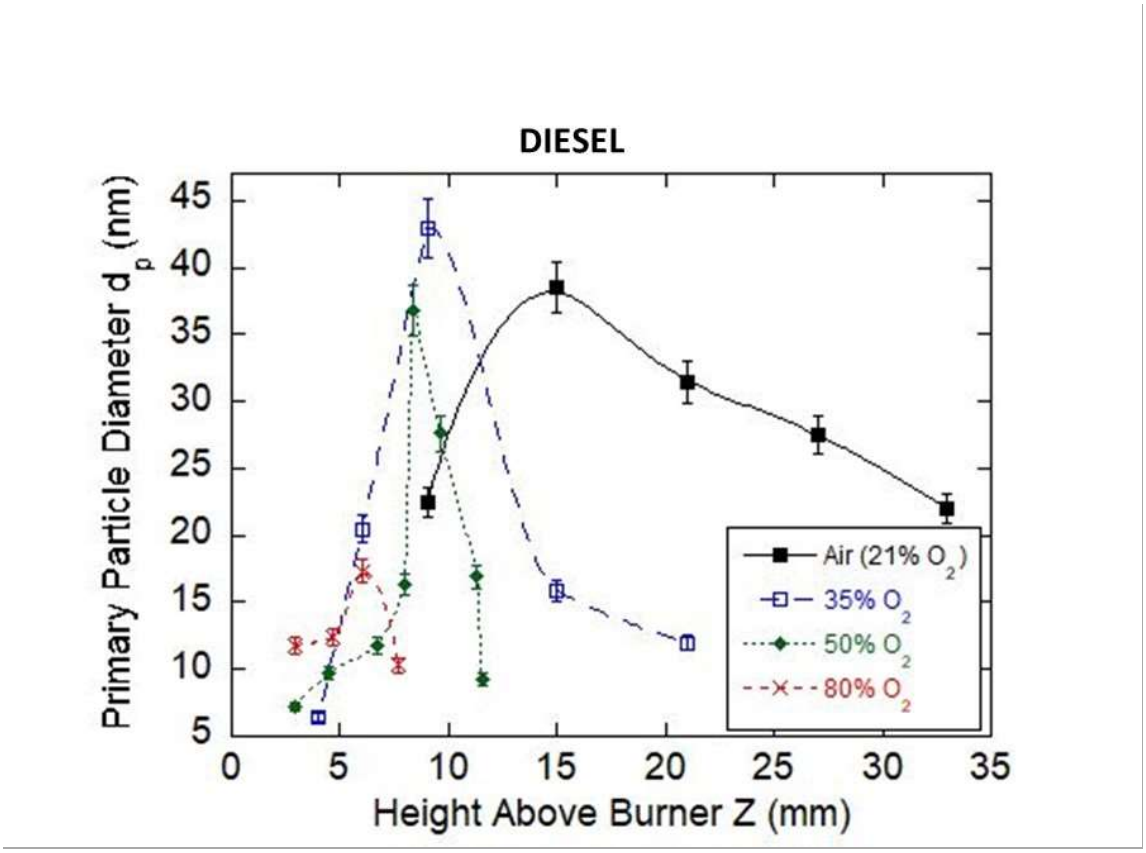


***Figure 20:*** *The plot represents the average primary particle diameter ($d_p$) with respect to the axial sampled heights for the Diesel flames tested at different flame heights above the burner (Z). Each curve is marked to represent the $O_2$ composition in the oxidizer (the balance is $N_2$). The measurement uncertainty is indicated by the vertical error bars; each bar denotes one standard deviation.*

Figure 21 displays the graphs of $d_p$ vs. HAB of all CME flames. Figure 21 displays the plot for CME/21% $O_2$ (air) (color-coded black) adapted from the work of Merchan-Merchan et al. [33]. Figure 21 also displays the plots of CME/35% $O_2$ (color-coded blue), CME/50% $O_2$ (color-coded

green), and CME/80% $O_2$ (color-coded red). Like the plots for diesel flames, the $d_p$ data for CME flames is gathered from the medium resolution images.

It is noticeable that the oxygen increase affects the oxidation of soot particles occurring near the flame tip. The particles forming the aggregates are decreasing in size as the oxygen content increases. As soot particles travel along the flame volume from HAB = 9 to 33 mm in the diesel/21% $O_2$ (air) flame the $d_p$ value increases rapidly from the lower part of the flame to the mid-flame height. At the mid-flame height of diesel/21% $O_2$ (air) the largest $d_p$ was measured or also known as the peak $d_p$ value. The diesel-air flame $d_p$ decreases gradually from the peak $d_p$ to the highest sampled position (HAB = 33 mm). Contrarily, in the oxygen-enhanced flames, the $d_p$ value decreases abruptly. The flame in diesel/35% $O_2$ HAB values range from 4 to 21 mm, diesel/50% $O_2$ ranges from HAB = 2.9 to 11.5 mm, and diesel/80% $O_2$ ranges from HAB = 2.9 to 7.7 mm. The oxygen enhanced diesel flames show that $d_p$ decreases rapidly to the highest HAB. This dramatic decrease in $d_p$ as oxygen content increases shows the soot formation and oxidation process is accelerated.

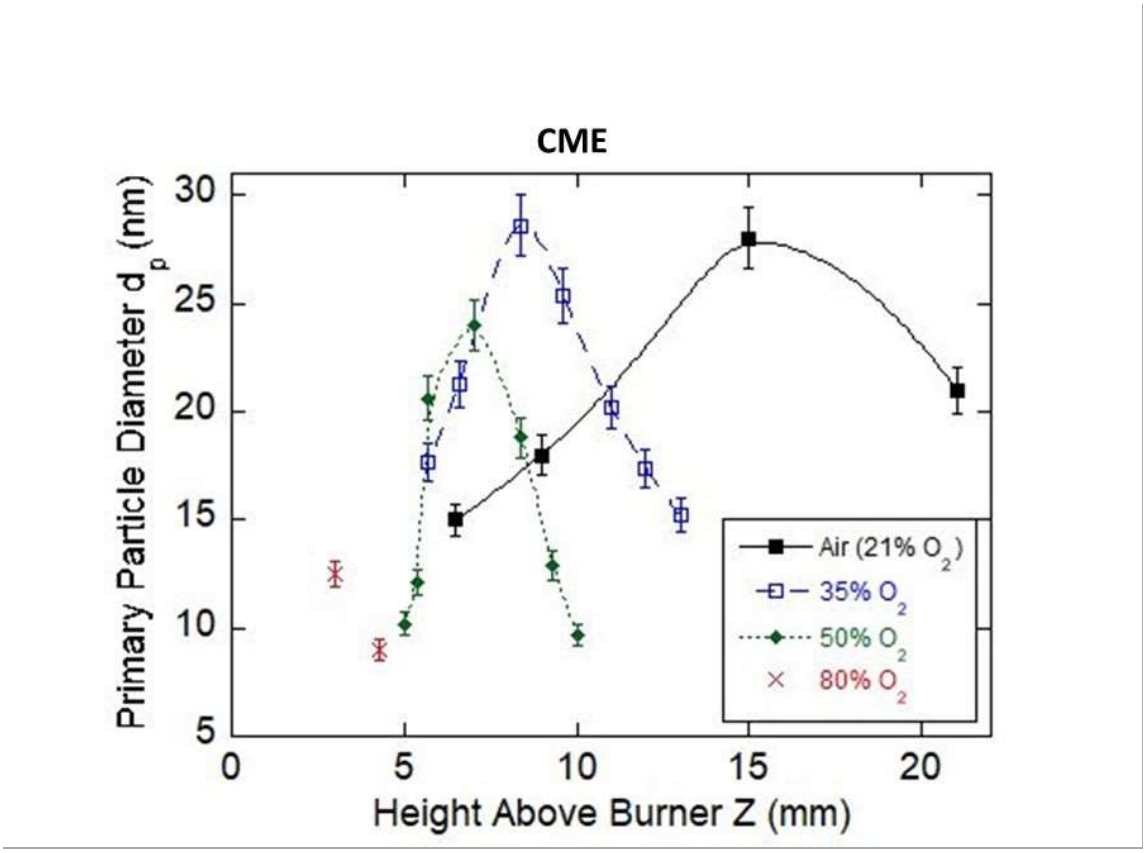


***Figure 21:*** *The plot represents the average primary particle diameter ($d_p$) with respect to the axial sampled heights for the CME flames tested at different flame heights above the burner (Z). Each curve is marked to represent the $O_2$ composition in the oxidizer (the balance is $N_2$). The measurement uncertainty is indicated by the vertical error bars; each bar denotes one standard deviation.*

The graph in Fig. 22 represents the peak value of average $d_p$ with respect to the $O_2$ composition in the oxidizer (the balance is $N_2$). Each curve in Fig. 22 is marked to represent the fuel used in the flame. A striking trend is found in diesel flames when considering the peak $d_p$ value vs. the oxygen content % $O_2$. The peak $d_p$ value increases from 21% $O_2$ (air) to 35% $O_2$ and then decreases for

50% $O_2$ and 80% $O_2$. Diesel/35% $O_2$ shows the highest peak $d_p$ value ~42.9 nm compared to diesel/air with ~38.5 nm, diesel/50% $O_2$ with ~36.8 nm, and diesel/80% $O_2$ with ~17.3 nm. Lee and coworkers used 21% $O_2$ (air), 50% $O_2$, and 100% $O_2$ to study the soot formation of laminar coannular non-premixed methane flames. In that study, methane/50% $O_2$ experienced the same sequence of events (inception, growth, and oxidation) as methane/air flame, but in a much shorter period. The reasons reported for a larger peak $d_p$ value in methane/50% $O_2$ than in methane/air are as follows. The reduced residence times in oxygen-enriched flames tend to inhibit soot growth. Oxy/fuel flames enhance soot formation due to higher temperatures and promote soot oxidative mechanisms. Furthermore, the soot surface growth rates are much stronger under oxy/fuel conditions given the similar peak $d_p$ values observed for methane/air and methane/50% $O_2$ [34]. A comparable trend to Lee and coworkers is found in the present study. The diesel/35% $O_2$ shows the highest peak $d_p$ value and diesel/air and diesel/50% $O_2$ have similar peak $d_p$ values.

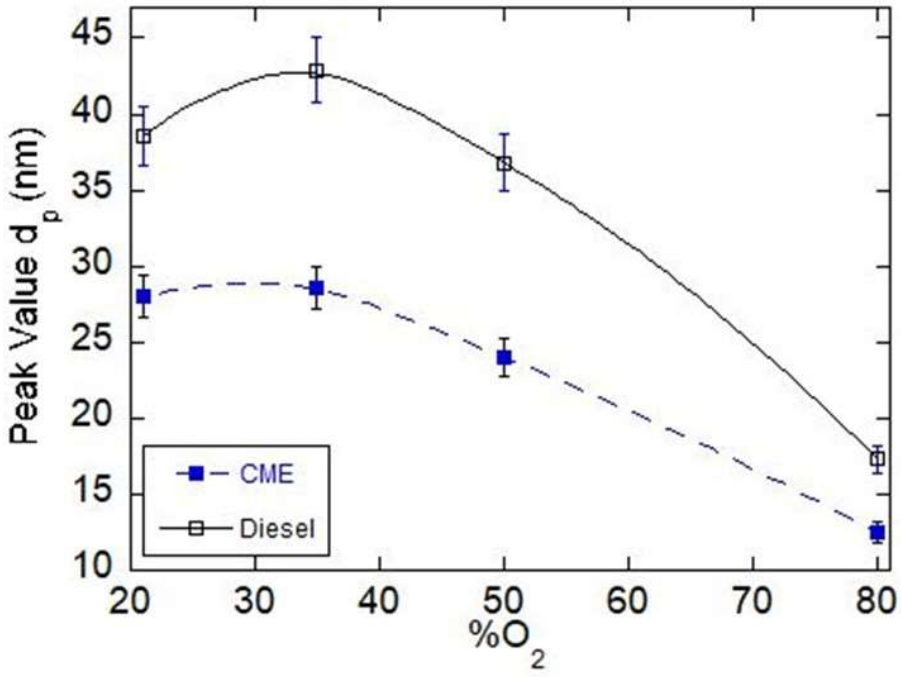


***Figure 22:*** *The plot represents the peak value of average primary particle diameter (dp) with respect to the $O_2$ composition in the oxidizer (the balance is $N_2$). Each curve is marked to represent the fuel used in the flame. The measurement uncertainty is indicated by the vertical error bars; each bar denotes one standard deviation.*

Examining the trend in CME flames of peak $d_p$ vs. oxygen content gives interesting results. The peak $d_p$ values are as follows: CME/21% $O_2$ is ~28 nm; CME/35% $O_2$ is ~28.6 nm; and CME/50% $O_2$ is ~24 nm. For CME/80% $O_2$ the flame only had two sampled heights so the largest $d_p$ value of ~12.5 nm is used as the peak $d_p$. Notice that CME/35% $O_2$ has the highest peak $d_p$ value compared to CME/21% $O_2$, CME/50% $O_2$, and CME/80% $O_2$. As explained earlier, Lee et al. found a reciprocal trend when comparing peak $d_p$ values and oxygen content in methane flames [34]. Still,

in the CME flames, a drop in $d_p$ value after the peak $d_p$ accelerates as oxygen content increases. A larger drop in $d_p$ value is obtained for oxy/fuel flames than air.

### 4.4 Chapter Summary

In our present study, the soot formation, evolution, and primary particle diameter ($d_p$) were studied in air and oxygen enriched air flames. The coflow diffusion flames were formed using two fuels: No. 2 diesel and canola methyl ester (CME). The oxygen content was varied in the oxidizer stream from 21% (air) to 80% $O_2$. The soot studies were possible with thermophoretic sampling and transmission electron microscopy (TEM) analysis. The center of the flames was sampled at various heights above burner (HAB) along the flame axial direction. Soot particle morphology was studied in detail with the obtained low resolution TEM images. Evolution of soot particle formation figures were created with both low and medium resolution TEM images.

Several observations are obtained from the study of soot formation, evolution, and morphology in diesel and CME oxygen enriched air flames: (i) The soot formation process (inception, surface growth, agglomeration, and oxidation) was analogous for all flames tested. (ii) The flames formed with CME showed the presence of "globules" or irregular-shaped structures. (iii) The presence of globules decreased as the oxygen content increased in the oxidizer stream for CME flames. (iv) Light contrast precursor particles were found in the diesel/50% $O_2$ flame and in all the CME flames. (v) The presence of soot precursors was more evident in diesel flames than in CME flames. (vi) Non-representative short aggregates were found near the burner mouth for both diesel and

CME oxygen enriched air flames. (vii) As the oxygen content increased in the oxidizer stream the flame height decreased and the rate of soot formation increased.

The medium resolution TEM images were used to obtain the $d_p$ values. The $d_p$ values were obtained from measuring the representative particles at each HAB. The largest $d_p$ value is known as the peak $d_p$, and this occurred near the middle of the flames. The decrease in $d_p$ value from peak $d_p$ to the highest HAB is very drastic in CME oxygen enriched air flames. Therefore, the oxidation rate in CME oxygen enriched air flames was much faster when compared to CME-air and diesel flames. Furthermore, the peak $d_p$ values were higher for diesel flames than CME flames. Also, in our study a trend in peak $d_p$ versus the oxygen content in the oxidizer stream (% $O_2$) was found, like the one found in the literature [34]. Regardless of the fuel (diesel or CME), the peak $d_p$ trend was analogous. The peak $d_p$ values at 21% (air) and 50% $O_2$ were similar, while the peak $d_p$ value for 35% $O_2$ was the largest $d_p$ value amongst all the oxygen contents tested.

# Chapter 5 – Conclusions and Future Work Recommendations

Soot evolution profiles, formation, morphology, and primary particle diameters ($d_p$) were obtained from studying eight coflow diffusion flames. The flames were formed using two fuels: canola methyl ester (CME) and No. 2 diesel. The oxygen ($O_2$) content in the oxidizer stream was varied (21% (air), 35%, 50%, and 80% $O_2$) while the balance is nitrogen ($N_2$). The soot formation was experimentally investigated by thermophoretic sampling and transmission electron microscopy (TEM) analysis. The insertion of the TEM grid at various heights above the burner (HAB) allowed for the study of soot evolution, formation, and morphology in air and oxygen enriched air flames. The TEM analysis provided images at low and medium resolution. The low-resolution images were used to study of soot formation, while the medium resolution images were used to obtain the $d_p$. The conclusions obtained from the results of our study and recommendations for future work are in discussed in this chapter.

## 5.1 Conclusions

There are similarities and differences in soot formation between diesel and CME oxy/fuel flames. Remarkably, the first similarity is the sequence of events in the soot formation process. Using either fuel (diesel or CME) the soot formation process includes inception, surface growth, agglomeration, and oxidation. Visually it looks like both diesel and CME flames at 50% $O_2$ have resembling soot clusters at the height closest to the burner mouth. Also, the TEM images near the burner mouth look similar for both fuels (diesel and CME) at 80% $O_2$. Fascinatingly, the short aggregates present during oxidation at the height closest to the flame tip also look similar for both flames at 50% $O_2$. Furthermore, regardless of the fuel type (diesel or CME) the introduction of

80% $O_2$ in the oxidizer stream resulted in a compressed or narrow flame region for the formation of soot precursors.

The main disparities between diesel and CME are as follows. At 35% $O_2$ content the soot inception looks very different when comparing diesel and CME flames. In the lowest flame height, the diesel/35% $O_2$ flame has many small precursors present. Whereas, in CME/35% $O_2$ flame has small aggregates present and very few precursors. Furthermore, the CME flames display shorter aggregates than in diesel flames during surface growth zone. The contrast of diesel-air and CME-air flames are apparent when comparing the surface growth. The diesel/21% $O_2$ flame is already forming short aggregates, yet CME/21% $O_2$ has predominantly small precursors. Additionally, at the peak $d_p$ value, there is a very long aggregate in diesel/35% $O_2$ versus very short aggregates in CME/35% $O_2$. Moreover, the CME flames produce more aggregates than diesel flames during the beginning of the oxidation process. Finally, the images near the flame tip look very different when comparing diesel/35% $O_2$ and CME/35% $O_2$. The aggregates in CME/35% $O_2$ are longer than in diesel/35% $O_2$ when the oxidation process happens. Furthermore, the CME/80% $O_2$ flame is basically half the size of the diesel/80% $O_2$ flame when regarding the highest sampled height. The oxy/fuel effect is very pronounced for the CME/80% $O_2$ flame in comparison to the diesel/80% $O_2$ flame.

Three key features are apparent of the oxygen-enhanced air flames from the obtained soot evolution profiles and primary particle diameters ($d_p$) data: i) the significant reduction of the flame

height, ii) the presence of a strong oxidative reaction zone as the oxygen content is increased and iii) the trend of the $d_p$ peak value.

First, the CME flames are shorter than the diesel flames. The highest sampled height of CME flames was 21 mm for 21% $O_2$ (air). The following highest sampled heights were obtained for the CME oxygen enriched air flames: 12 mm for 35% $O_2$, 9.5 mm for 50% $O_2$, and 4.5 mm for 80% $O_2$. In the diesel flames, the sampled height near the flame tip was 33 mm for 21% $O_2$ (air), 21 mm for 35% $O_2$, 11.5 mm for 50% $O_2$, and 8 mm for 80% $O_2$. Regardless of the variation in flame height, the same steps of soot formation took place in each flame, with soot inception, surface growth, agglomeration, and oxidation.

Second, as the oxygen increased in the oxidizer stream the oxidation of soot was enhanced. The long aggregates that are normally present near the flame tip for diesel and CME air flames were suppressed in the oxygen enriched flames. In the CME oxygen enriched flames the aggregates near the flame tip were severely suppressed when compared to diesel flames. In the diesel flames the reduction of soot precursors as oxygen content increased was pronounced. The presence of globules or irregular shaped structures in the CME flames decreased as the oxygen content increased. An increase in the soot formation rate is found for oxygen enhanced flames.

Third, the peak $d_p$ values of the CME flames are smaller than in diesel flames. Biodiesel is an oxygenated fuel that enhances soot oxidation. These reductions are primarily due to the oxidation rate of biodiesel which can be as much as six times that of diesel [110]. Notice that CME/35% $O_2$

has the highest peak $d_p$ value compared to CME/21% $O_2$ (air), CME/50% $O_2$, and CME/80% $O_2$ flames. Fascinatingly enough the same occurred for the diesel flames in this study. Since the $d_p$ value decrease is more notable for oxygen-enhanced flames in CME we can see the oxidation process is accelerated.

### 5.2 Future Work Recommendations

Soot formation, evolution, morphology, and primary particle diameter ($d_p$) have been determined for CME and diesel air and oxygen enriched air flames. Below are recommendations for future studies:

1. High resolution TEM analysis on the soot nanostructure from oxygen enhanced CME co-flow diffusion flames.
2. Studying the species present in CME oxygen enhanced co-flow diffusion flames by gas chromatography.
3. Soot sampling and scanning electron microscopy (SEM) analysis of soot generated above a biodiesel-air co-flow diffusion flame. The flame can be disturbed to create a soot tail and thermophoretically sample particles generated in the soot tail. To study soot cluster agglomeration in the environment.

# References


[1] Y. Wang, S. H. Chung, Progress in Energy and Combustion Science 74 (2019) 152-238.
[2] S. Rajkumar, J. Thangaraja, Fuel 240 (2019) 101-118.
[3] M. R. Kholghy, Y. Afarin, A. D. Sediako, J. Barba, M. Lapuerta, C. Chu, J. Weingarten, B. Borshanpour, V. Chernow, M. J. Thomson, Combustion and Flame 176 (2017) 567-583.
[4] C. E. Jr. Baukal, Oxygen Enhanced Combustion, 2nd Ed., CRC Press, Boca Raton, FL, p. 385, 2013.
[5] Asahi Carbon CO., LTD, https://www.asahicarbon.co.jp/global_site/product/cb/usage.html
[6] Hart Keramik AG, https://hart-keramik.de/en/2017/07/31/chimney-fire-resistant/
[7] MarketWatch, https://www.marketwatch.com/story/four-in-10-americans-are-breathing-unsafe-air-and-these-8-cities-are-the-worst-2019-04-24
[8] W. Merchan-Merchan, S. Granados Sanmiguel, S. McCollam, Fuel 102 (2012) 525-535.
[9] G. Knothe, C. A. Sharp, T. W. Ryan, Energy Fuels 20 (2006) 403-408.
[10] W. G. Wang, D. W. Lyons, N. N. Clark, M. Gautam, Environ. Sci. Technol. 34 (2000) 933-939.
[11] H. A. Michelsen, M. B. Colket, P. E. Bengtsson, A. D'Anna, P. Desgroux, B. S. Haynes, J. H. Miller, G. J. Nathan, H. Pitsch, and H. Wang, ACS Nano 14 (2020) 12470-12490.
[12] C. Scrimgeour, Chemistry of fatty acids, InL Bailey's industrial oil and fat products, 6th Ed., John Wiley & Sons Inc, New York, 2005.
[13] M. Cadrazco, A. Santamaria, I. C. Jaramillo, K. Kaur, K.E. Kelly, J. R. Agudelo, Combustion and Flame 214 (2020) 65-79.
[14] C. R. Shaddix, T. C. Williams, American Scientist, 95 (2007) 232-239.
[15] M. Frenklach, Phys Chem Chem Phys 4 (2002) 2028–37.
[16] S. E. Stein, A. Fahr, J Phys Chem 89 (1985) 3714–25.
[17] V. Chernov, M. J. Thomson, S. B. Dworkin, N. A. Slavinskaya, U. Riedel, Combust Flame 161 (2014) 592–601.
[18] M. Sirignano, A. D'Anna, Proc Combust Inst 34 (2013) 1877–84.
[19] B. S. Haynes, H. G. Wagner, Z Phys Chem 133 (1982) 201-2013.
[20] H. S. Guo, Z. Z. Gu, K. A. Thomson, G. J. Smallwood, F. F. Baksh, Proc Combust Inst 34 (2013) 1795–802.
[21] L. Zhou, N. J. Dam, M. D. Boot, L. P. H. de Goey, Combust Flame 161 (2014) 2669–77.
[22] A. Cavaliere, R. Barbella, A. Ciajolo, A. D'Anna, R. Ragucci, Proc Combust Inst 25 (1994) 167–74.
[23] K. G. Neoh, J. B. Howard, A. F. Sarofim, Proc Combust Inst 20 (1985) 951–7.
[24] M. P. B. Musculus, L. A. Pickett, Combust Flame 141 (2005) 371–91.
[25] H. I. Joo, Ph.D. Thesis University of Toronto 2010.
[26] T. L. Berry, W. L. Roberts, Combust Flame 145 (2006) 571–8.
[27] M. D. Smooke, C. S. McEnally, L. D. Pfefferle, R. J. Hall, M. B. Colket, Combust Flame 117 (1999) 117–39.
[28] K. T. Dotson, P. B. Sunderland, Z. G. Yuan, D. L. Urban, Fire Safety J 46 (2011) 550–5.
[29] K. T. Kang, J. Y. Hwang, S. H. Chung, W. Lee. Combust Flame 109 (1997) 266–81.
[30] A.E. Karatas, Ö.L. Gülder, Prog. Energy Combust. Sci. 38 (2012) 818–845.
[31] W. Merchan-Merchan, S. McCollam, J. F. Correa Pugliese, Fuel 156 (2015) 129-141.
[32] N. D. Love, B. T. Goepfert, R. N. Parthasarathy, S. R. Gollahalli, AIAA Aerosp Sci Meet Exhib Reno, Nevada; January 7–10 2008.

[33] W. Merchan-Merchan, A. Abdihamzehkolaei, D. Merchan-Breuer, Fuel 226 (2018) 263–277.
[34] K. O. Lee, C. M. Megaridis, S. Zelepouga, A. V. Saveliev, L. A. Kennedy, Combust. Flame 121 (2000) 323–333.

[35] M. R. Kholghy, J. Weingarten, A. D. Sediako, J. Barba, M. Lapuerta, M. J. Thomson, Proc Combust Inst, 36 (2017) 1321-1328, 2017.
[36] Z. Gao, L. Zhu, Z. Zou, C. Liu, Z. Huang, SAE Technical Paper 2017-01-2397, 2017.
[37] M. Kholghy, M. Saffaripour, C. Yip, M. J. Thomson, Combust. Flame 160 (2013) 2119-2130.
[38] T. C. Bond, S. J. Doherty, D. W. Fahey, P. M. Forster, T. Berntsen, B. J. DeAngelo, M. G. Flanner, S. Ghan, B. Karcher, D. Koch, S. Kinne, Y. Kondo, P. K. Quinn, M. C. Sarofim, M. G. Schultz, M. Schulz, C. Venkataraman, H. Zhang, S. Zhang, N. Bellouin, S. K. Guttikunda, P. K. Hopke, M. Z. Jacobson, J. W. Kaiser, Z. Klimont, U. Lohmann, J. P. Schwarz, D. Shindell, T. Storelvmo, S. G. Warren, C. S. Zender, J Geophys Res Atmos 118 (2013) 5380–552.

[39] A. Beltrame, P. Porshnev, W. Merchan-Merchan, A. Saveliev, A. Fridman, L. A. Kennedy, O. Petrova, S. Zhdanok, F. Amouri, O. Charon, Combust. Flame 124 (2001) 295-310.
[40] K. Saito, F. A. Williams, S. Gordon, Combust. Sci. and Tech. 47 (1986) 117-138.

[41] S. Zelepouga, A. V. Saveliev, L. A. Kennedy, A. A. Fridman, Combust. Flame 121 (2000) 76–89.

[42] D. X. Du, R. L. Axelbaum, C. K. Law, Proc Combust Inst, 23 (1991) 1501-1507.
[43] C. E. Jr. Baukal, Oxygen-Enhanced Combustion, CRC Press, Boca Raton, FL, p. 369, 1998.

[44] R. Henriquez, R. Demarco, J. L. Consalvi, F. Liu, A. Fuentes, Combust Science and Technology 186 (2014) 504–517.

[45] B. M. Kumfer, S. A. Skeen, R. Chen, R. L. Axelbaum, Combust. Flame 147 (2006) 233–242.
[46] W. Yan, D. Chen, Z. Yang, E. Yan, P. Zhao, Energies 10 (2017) 750.
[47] M. Lapuerta, J. Barbaa, A. D. Sediako, M. R. Kholghy, M. J. Thomson, Journal of Aerosol Science 111 (2017) 65–74.
[48] V. Garpen J., Fuel Processing Technology 86 (2005) 1097-1107.
[49] C.L. Peterson, G.L. Wagner, D.L. Auld, Trans. ASAE 26 (1983) 322-327.
[50] Canola Council of Canada. https://www.canolacouncil.org/about-canola/industry/
[51] L. Qin, L. Liu, A. P. Zeng, D. Wei, Bioresource. Technol. 245 (2017) 1507-1519.
[52] S. Saran, A. Mathur, J. Dalal, R. K. Saxena, Fuel 188 (2017) 324-331.
[53] B. Zhang, S. Xiu, A. Shahbazi, M. J. Acosta (E.d.), Nova Science Publishers, Inc., vol. 11, p. 203-216, 2012.
[54] J. Sheehan, T. Dunahay, J. Benemann, P. Roessler, National Renewable Energy Laboratory, CO, USA, vol. 328, 1998.
[55] M. H. Huesemann, T. S. Hausmann, R. Bartha, M. Aksoy, J. C. Weissman, J. R. Benemann, Appl Biochem Biotechnol 157 (2009) 507–26.
[56] Y. Christi, Biotechnol Adv 25 (2007) 294-306.
[57] I. M. Atadashi, M. K. Aroua, A. A. Abdul, Renew Energy 36 (2011) 437-43.
[58] M. J. Ramos, C. M. Fernandez, A. Casas, L. Rodriguez, A. Perez, Bioresource Technology 100 (2009) 261-268.

[59] M. A. Altaher, G. E. Andrews, H. Li, Proceedings of ASME Turbo Expo 2013: Turbine Technical Conference and Exposition, vol. 1B: Combustion, Fuels and Emissions, San Antonio, Texas, USA, June 3-7, 2013.
[60] National Geographic. https://www.nationalgeographic.org/encyclopedia/petroleum/.
[61] U. Schorken, P. Kempers, European Journal of Lipid Science and Technol, 111 (2009) 627-645.
[62] A. P. Vyas, J. L. Verma, N. Subrahmanyam, Fuel 89 (2010) 1-9.
[63] J. Xue. T. E. Grift, A. C. Hansesn, Renew Sust Energy Rev 15 (2011) 1098-116.
[64] J. M. Encinar, A. Pardal, N. Sanchez, Fuel 166 (2016) 51-58.
[65] H. Li, A. Lea-Langton, G. E. Andrews, M. Thompson, C. Musungo, SAE Technical Paper 2008-01-0076, 2008.
[66] S. A. Basha, K. R. Gopal, S. Jebaraj, Renew Sustain Energy Rev 13 (2009) 1628–34.
[67] V. M. Rossinskii, B.A. Énglin, Chem Technol Fuels Oils 16 (1980) 26-29.
[68] E. F. Aransiola, T. V. Ojumu, O. O. Oyekola, T. F. Madzimbamuto, D. I. O. A. Ikhu-Omoregbe, Biomass Bioenergy 61 (2014) 276-97.
[69] S. P. Singh, D. Singh, Renew Sustain Energy Rev 14 (2010) 200-16.
[70] J. F. Reyes, M. A. Sepulveda, Fuel 85 (2006) 1714-1719.
[71] P. Verma, M. P. Sharma, G. Dwivedi, International Journal of Renewable Energy Research 7 (2017) 3196-3202.
[72] Z. Jurac, V. Zlatar, Fuel Process Technol 106 (2013) 108-113.
[73] B. R. Moser, Energy Fuels 22 (2008) 4301–6.
[74] U. Thiyam-Holländer, M. N. A. Eskin, B. Matthäus, CRC Press, 2012.
[75] M. A. Fazal, A. S. M. A. Haseeb, H. H. Masjuki, Fuel Processing Technology 91 (2010) 1308-1315.
[76] T. Tsuchiya, H. Shiotani, S. Goto, G. Sugiyama, A. Maeda, SAE Technical Paper 2006-01-3303, 2006.
[77] A. Boehman, J. Song, M. Alam, Energy & Fuels 19 (2005) 1857-1864.
[78] C. Pereira, G. Wang, M. Costa, Energy 74 (2014) 950-955.
[79] D. B. Olson, J. C. Pickens, Combust Flame 57 (1984) 199–208.
[80] P. Verma, E. Pickering, M. Jafari, Combust and Flame 205 (2019) 206–219.
[81] N. Savic, M. M. Rahman, B. Miljevic, Carbon 104 (2016) 179-189.
[82] M. Salamanca, F. Mondragon, J. R. Agudelo, P. Benjumea, A. Santamaría, Combust. Flame 159 (2012) 1100-1108.
[83] H. Seong, K. Lee, S. Choi, C. Adams, D. E. Foster, SAE Technical Paper 2012-01-0441, 2012.
[84] H. Kurji, A. Valera-Medina, A. Okon, C. T. Chong, Energy Procedia 142 (2017) 154-159.
[85] Z. Habib, R. Parthasarathy, S. Gollahalli, Applied Energy, 87 (2010) 1701-1709.
[86] H. Omidvarborna, A. Kumar, D. S. Kim, Science of the Total Environment 544 (2016) 450-459.
[87] M. Lapuerta, O. Armas, J. Rodriguez-Fernandez, Progress in Energy and Combustion Science 34 (2008) 198-223.
[88] R. J. Last, M. Kruger, M. Durnholz, SAE Technical Paper 950054, 1995.
[89] D. B. Kittelson, J Aerosol Sci 29 (1998) 575-88.
[90] J. Krahl, A. Munack, O. Schroder, H. Stein, J. Bunger, SAE Technical Paper 2003-01-3199, 2003.
[91] J. Song, M. Alam, A. L. Boehman, U. Kim, Combust Flame 146 (2006) 589-604.

[92] R. L. Vander Wal, A. J. Tomasek, Combust. Flame 134 (2003) 1-9.
[93] F. Wu, J. Wang, W. Chen, S. Shuai, Atmospheric Environment 43 (2009) 1481-1485.
[94] O. B. Popovicheva, C. Irimiea, Y. Carpentier, et al., Aerosol and Air Quality Research 17 (2017) 1717–1734.
[95] S. L. Lin, J. H. Tsai, S. J. Chen, K. L. Huang, C. C. Lin, H. T. Huang, Y. C. Hsieh, C. H. Chiu, Aerosol and Air Quality Research 17 (2017) 1579–1589.
[96] K. Na, S. Biswas, W. Robertson, K. Sahay, R. Okamoto, A. Mitchell, S. Lemieux, Atmos. Environ. 107 (2015) 307–314.
[97] C. M. Megaridis, R. A. Dobbins, Symposium (International) on Combustion 22 (1989) 353–62.

[98] C. M. Megaridis, R. A. Dobbins, American Chemical Society (1987) 254–259.
[99] K. O. Lee, R. Cole, R. Sekar, M. Y. Choi, J. Zhu, J. Kang, and C. Bae, SAE Technical Paper 2001-01-3572, 2001.

[100] K. O. Lee, R. Cole, R. Sekar, M. Y. Choi, J. S. Kang, C. S. Bae, H. D. Shin, Proceedings of the Combustion Institute 29 (2002) 647-653.
[101] W. Merchan-Merchan, S. G. Sanmiguel, S. McCollam, Fuel 102 (2012) 525–35.

[102] R. J. Santoro, T. T. Yeh, J. J. Horvath, H. G. Semerjian, Combust Science and Technology 53 (1987) 89–115.

[103] R. Lin, Y. Zhu, L. L. Tavlarides, Fuel 106 (2013) 593–604.
[104] R. Lin, L. L. Tavlarides, J. of Supercritical Fluids 75 (2013) 101-111.
[105] B. Zhao, K. Uchikawa, H. Wang, Proc Combust Inst 31 (2007) 851–60.
[106] K. Okabe, M. Sakai, Y. Mizutani, T. Aizawa, SAE Int. J. Fuels Lubr. 6 (2013) 807–816.
[107] J. Hwang, F. S. Hirner, C. Bae, et al., Applied Thermal Engineering 159 (2019) 113899.
[108] R. A. Dobbins, C. M. Megaridis, Langmuir, (1987) 254-259.

[109] C. M. Megaridis, Ph. D. Thesis, Brown University 1987.
[110] R. L. Vander Wal, A. Strzelec, T. J. Toops, C. S. Daw, C. L. Genzale, Fuel 113 (2013) 522–526.

# Appendix A – Resume

**STEPHANIE PRADO CARBONELL**

prad2961@gmail.com

## EDUCATION

**University of Oklahoma** | Norman, OK

**Master of Science in Mechanical Engineering** | May 2021 | Overall GPA: 3.83/4.00
**Bachelor of Science in Mechanical Engineering** | May 2019 | Overall GPA: 3.52/4.00

**University of Oklahoma – Arezzo** | Arezzo, Italy

**Engineering Education Abroad** | May 2018 (2-week program) | Overall GPA: 4.00/4.00

## ENGINEERING EXPERIENCE

**Graduate Research Assistant** | **Combustion, Plasma, and Nanoparticle Laboratory** | OU | Aug 2019–May 2021

- Published in the Central States Section of The Combustion Institute 2020 Spring Technical Paper Volume
- Executed a literature review of soot formation in oxygen enhanced combustion
- Studied soot formation in diffusion oxygen-enhanced biodiesel flames

**Mechanical Energy Intern** | **Burns & McDonnell** | Kansas City, MO | Jun–Aug 2020

- Quality reviewed system drawings to match existing plant equipment configuration for various vendors and clients
- Interfaced with multiple disciplines within Burns & McDonnell nationally and internationally
- Collaborated on work package labeling of a combined cycle plant using Navisworks and iConstruct
- Evaluated previous steam turbine and heat recovery steam generator design data
- Trained on Fathom, Constructability, Welding, Pipe Stress and Pumps
- Updated standard Energy Global Practice documents to streamline future specifications

**Power Plant Intern** | **Oklahoma Gas & Electric** | Luther, OK | May–Aug 2019

- Managed installation project of 68 platforms to increase the safety of operators, mechanics, and technicians
- Drafted 3 scopes of work that identified OSHA standards, design requirements, codes, and specifications
- Assessed expenditures on scaffolding and potential savings for budgetary justifications
- Presented preliminary designs of safety platforms based on customer needs
- Provided a timeline of project implementation over two budget years

- Worked with vendors to identify budgetary estimates
- Participated in root cause failure analysis to evaluate the turbulent flow of the high-pressure steam line

**Undergraduate Research Assistant** | **Combustion, Plasma, and Nanoparticle Laboratory (CPNL)** | OU | Feb 2017–May 2019

- Handled safely hazardous chemicals in a laboratory, conducted experiments, collected, and analyzed data
- Tested the corrosiveness of alternative fuels by titrations with the director of the CPNL
- Studied various physical and chemical properties of biodiesel

**Power Plant Intern** | **Oklahoma Gas & Electric** | Luther, OK | Jun–Aug 2018

- Provided technical support to an ongoing condenser issue which rectified a ~ $1000/day loss of opportunity
- Managed a root cause failure analysis on the condenser
- Monitored performance of the condenser and vacuum pumps to optimize the utilization of equipment
- Determined possible solutions to overheated scanner blowers that provided cooling air to flame scanners
- Learned the main process of a combined cycle power plant

**Manufacturing Intern** | **Baker Hughes, a GE Company** | Houston, TX | Jun–Aug 2017

- Modeled valves and plates in Unigraphics NX8 that were manufactured, tested, and sold to customers
- Analyzed the Hydro testing process to document as a work instruction
- Organized the tooling department using Lean Six Sigma 5S method to increase productivity of the plant

**Product Design Intern** | **Ronnie K. Irani Center for the Creation of Economic Wealth** | Norman, OK | Aug–Dec 2016

- Created an evaporative cooling product for outdoor market vendors in developing countries to reduce food waste
- Analyzed market opportunity and path to market to produce the most beneficial product
- Presented weekly on design and development of the product to various audiences and a formal final presentation

## PUBLICATIONS AND CONFERENCE PROCEEDINGS

- S. Prado Carbonell, A. Abdihamzehkolaei, D. Merchan-Breuer, S. Srivastava, W. Merchan-Merchan. "Effect of Oxygen Concentration on Soot Formation in a Co-Flow Diffusion Reactor Fueled with Canola Methyl Ester and Diesel." (In preparation for FUEL).

- S. Prado Carbonell and W. Merchan-Merchan. Soot Formation in Biodiesel-Oxygen Enriched Air Laminar Diffusion Flames. 40th ASME/AIAA Online Regional Symposium. Oklahoma State University. April 3, 2021.

- S. Prado Carbonell. Effect of Oxygen Content on Soot Formation in a Co-Flow Diffusion Flame Fueled with Canola Methyl Ester and Diesel. Fall 2020 Graduate Student Virtual Poster Fair Energy Session. University of Oklahoma. November 13, 2020.

- S. Prado Carbonell, W. Merchan-Merchan. "Effect of Oxygen Content on Soot Formation in a Co-Flow Diffusion Reactor Fueled with Canola Methyl Ester and Diesel." 2020 Spring Technical Meeting Central States Section of The Combustion Institute. Huntsville, Alabama. (Published).

- S. Prado Carbonell. "A Study of the Total Acid Number in an Oxygenated Fuel (Biodiesel)." University of Oklahoma McNair Scholar's Thesis 2019.

- S. Prado Carbonell, W. Merchan-Merchan. A Study of the Total Acid Number in an Oxygenated Fuel (Biodiesel). Society of Hispanic Professional Engineers National Convention Engineering Science Symposium. Cleveland, Ohio. November 9, 2018.

- S. Prado Carbonell, W. Merchan-Merchan. Total Acid Number of Vegetable Oil-Based Biodiesel. University of New Mexico McNair Scholars Research Conference. Albuquerque, New Mexico. October 5, 2018.

- S. Prado Carbonell, W. Merchan-Merchan. Measuring the Acid Number of New Emerging Fuels. 2nd Annual Curiosity to Creativity Spring Symposium. University of Oklahoma. April 25, 2018.

## LEADERSHIP EXPERIENCE

**National Graduate Committee Volunteer** | **Society of Hispanic Professional Engineers (SHPE)** | Jul 2020–May 2021

- Managed the STEM Community Influence & Outreach group
- Initiated and solidified relations with Academic, Government, and Industry research institutions
- Increased the number of SHPE members with advanced degrees contributing to research and development

**Vice-Regional Student Representative (VRSR)** | **Society of Hispanic Professional Engineers** | Sept 2018–Jun 2019

- Served alongside 5 VRSR to provide support for ~2,000 students across 7 states
- Built a community between SHPE chapter presidents to improve each chapter
- Bridged the gap between chapter and regional leadership

**Chapter President** | **Society of Hispanic Professional Engineers** | OU | May 2017–May 2018

- Managed a team of 15 officers to coordinate at least 4 events each month for a chapter of ~40 active members
- Collaborated with company representatives to host technical and professional events
- Actively involved in mentorship and motivation of Hispanics in STEM
- Past positions: **Regional Marketing Director** | May–Aug 2019, **Academic Chair** | May 2018–May 2019, **VP of Chapter Development** | May 2016–May 2017, **Publicist** | Nov 2015–May 2016.

## SKILLS & AWARDS

- Bilingual in English and Spanish
- Latino Student Life Outstanding Graduate Student | May 2021
- NSF Bridge to the Doctorate Fellow | Jul 2018–May 2021
- Shell Scholar | Aug 2018
- Pi Tau Sigma International Mechanical Engineering Honor Society | May 2018
- OK Louis Stokes Alliances for Minority Participation Scholar | Jan 2018–May 2019
- Mentored Research Fellowship | Jan 2018
- BP Scholar | June 2017
- McNair Scholar | May 2017–May 2019
- Diversity & Inclusion Program Scholar | Jan 2016–May 2021
- Latino Student Life Academic Excellence Award | May 2016